

TWO-PHASE MODELING OF DEBRIS FLOWS

A dissertation submitted to
ETH ZURICH
for the degree of
Doctor of Science

presented by
JULIA KOWALSKI
Dipl. Math. (Universität Augsburg)
born 22. April 1979
citizen of
Germany

Accepted on the recommendation of
Prof. R. Jeltsch (ETH Zürich)
Dr. P. Bartelt (SLF Davos)
Dr. J. McElwaine (University of Cambridge)

Acknowledgement

This thesis is the result of my work at the Swiss Federal Institute for Snow and Avalanche Research (SLF) in Davos and its mother institution, the Swiss Federal Institute for Forest, Snow and Landscape Research (WSL) in Birmensdorf where I started as PhD student in Spring 2005. During my time I benefited in many different ways from many people to all of which I want to express my gratitude.

My research work was made possible through my adviser at SLF, Perry Bartelt. In countless lively discussions he shared with me his deep insight in avalanche and debris flow research. I wish to thank him for teaching me the awareness of application necessities and for at the same time granting me the freedom to pursue my own aspects of the project.

I also wish to thank my academic adviser, Prof. Rolf Jeltsch, from the Seminar for Applied Mathematics at the Swiss Federal Institute of Technology (ETH) in Zurich. He quickly accepted to supervise my project and his openness allowed a smooth interaction between SLF and ETH. I am especially grateful for his flexible and unbureaucratic way to organize the last weeks of my thesis time before the defense.

I am very thankful to Jim McElwaine from Cambridge University, UK, for his enthusiastic interest in my work and I am happy that he accepted to be external examiner of my thesis. I benefited from his knowledge both in modeling and application issues. The discussions with him have been intense and fruitful and advanced the quality of my work in many ways.

The every day of research life took place with colleagues from the avalanche and debris flow research groups at SLF and WSL. I am especially grateful to my office mate, Marc Christen from SLF, for the nice office atmosphere and the introduction to and discussion of geoscientific software, and to Corinna Wendeler from WSL, for the collaboration on data evaluation and the personal exchange on PhD students subtleties. Thanks also to Betti Sovilla (SLF), Martin Kern (SLF), Mark Schär (SLF), Katharina Platzer (formerly SLF), Brian McArdell (WSL), Christoph Graf (WSL), Axel Volkwein (WSL), Bruno Fritschi (WSL), Melissa Swartz (formerly WSL) and all the others.

My regular visits and discussions at the Seminar for Applied Mathematics at ETH Zurich also contributed immensely to both my academic and personal development. I always enjoyed my time with Peter Kauf, Miroslav Cada, Daniel Wright, Jörg Schmidt and the rest of SAM.

I also would like to thank my friends Ingrid Reiweger and Bettina Leimgruber for all the

nice things we did together besides my PhD, from skiing and climbing in the mountains to the cosy evenings in the Davos nightlife. And I am unspeakably grateful to my family and my boyfriend, Manuel Torrilhon, for their invaluable support that helped me through the ups and downs of the years of PhD.

Davos, May 2008

J.K.

Contents

Zusammenfassung	1
Summary	3
1 Introduction to Debris Flows	5
1.1 Classification and Definition	5
1.2 Terminology	7
1.2.1 Initiation, Transit, and Run-out zone	7
1.2.2 A single debris flow surge	8
1.3 Effective stress and fluid pore pressure	8
1.3.1 Stationary state of a particle-fluid mixture	9
1.3.2 Suspension limit of a particle-fluid mixture	9
1.3.3 Dynamic transition	10
1.3.4 Stress concepts in a debris flow	11
1.3.5 Extension to a multi-dimensional stress state	12
1.4 Current Debris Flow research	13
1.4.1 Homogeneous mixture approach	13
1.4.2 Iverson's model	14
1.4.3 Multi-component mixture approach	14
1.4.4 Motivation	14
2 Experimental data sets	17
2.1 Debris flow measurements	17
2.1.1 Real scale events at Illgraben	17
2.1.2 Chute experiments	19
2.2 Dimensional analysis	21
2.2.1 Significant physical parameters	21
2.2.2 Dimensionless groups for debris flows	22
2.3 Fluid pore pressure results	24
2.3.1 Illgraben results	24
2.3.2 USGS - Flume results	26
2.4 Measurements versus existing theories	27
2.4.1 One-phase, rheological models	27
2.4.2 The Iverson/Denlinger model	28
2.4.3 Existing depth-integrated multi-component approaches	28

2.4.4	Necessity of a model extension	29
3	Derivation of a one-phase shallow flow model	31
3.1	Framework and balance laws	31
3.1.1	Coordinate system	31
3.1.2	Basic set of equations	32
3.2	Boundary conditions	32
3.2.1	Kinematic conditions	33
3.2.2	Dynamic conditions	34
3.3	Dimensionless coordinates	35
3.3.1	Definition of the scales	35
3.3.2	Scaled model formulation	35
3.3.3	Scaled boundary conditions	36
3.4	Integration over the flow depth	36
3.4.1	Flow height and shallow flow assumption	36
3.4.2	Preliminary considerations	37
3.4.3	Depth-averaged mass conservation	37
3.4.4	Depth-averaged momentum balance	38
3.5	Remark on the shape factor	38
3.5.1	Shear layer thickness	39
3.5.2	Shear layer curvature	39
3.6	Constitutive Relation for the stress	40
3.6.1	Vertical momentum balance	40
3.6.2	Isotropic fluid	40
3.6.3	Mohr-Coulomb material	40
3.7	The Savage-Hutter model	41
3.7.1	Final formulation	41
3.7.2	Eigenvalues	42
3.8	Voellmy-Salm variation and practical use	42
4	A depth-integrated multi-component system	45
4.1	Multi-component balance laws	46
4.1.1	General framework	46
4.1.2	Single component balance laws	46
4.1.3	Full saturation	47
4.1.4	Incompressibility and volume-averaged velocity	48
4.1.5	Viscous drag momentum exchange	48
4.2	Kinematic boundary conditions	48
4.2.1	Generalization to an arbitrary interface	49
4.2.2	Autonomy assumption	49
4.3	Dynamic boundary conditions	50
4.4	Dimensionless coordinates	51
4.4.1	Definition of the scales	51
4.4.2	Scaled single component balance laws	52
4.4.3	Scaled boundary conditions	52

4.5	Depth-integration	53
4.5.1	Flow mass, height and averaging concept	53
4.5.2	Integrated single species mass conservation	53
4.5.3	Integrated single species momentum balance	53
4.5.4	Shape factor	54
4.5.5	Averaged stress and vertical center of mass	54
4.6	Uniform suspension	55
4.6.1	Inclusion of the boundary conditions	55
4.6.2	Closure for the vertical center of mass	56
4.6.3	Averaged momentum exchange	57
4.6.4	Summarized model formulation	57
4.6.5	Comparison to the Iverson and the Pitman/Le approach	58
4.7	Vertical layering	58
4.7.1	Incorporated boundary conditions	58
4.7.2	Averaged normal stresses	60
4.7.3	Summarized model formulation	60
4.7.4	Comparison to the two-layer shallow water theory	61
4.8	Combined approach	62
4.8.1	General setting	62
4.8.2	Boundary conditions	63
4.8.3	Averaged normal stresses	64
4.8.4	Final model formulation	65
4.8.5	Sedimentation and Re-suspension	66
4.9	Connection to the basal fluid pressure	67
5	Mathematical properties	69
5.1	Wave speeds and region of hyperbolicity	69
5.1.1	Characteristic polynomial	69
5.1.2	Remark on the two-layer system	71
5.1.3	Region of hyperbolicity	71
5.1.4	Eigenspeeds	73
5.1.5	An approximation for the fast waves	74
5.2	Simplified Riemann problem	75
5.2.1	Hyperbolic structure	75
5.2.2	Rankine Hugenoit jump conditions	76
5.2.3	Slow discontinuities	77
5.2.4	Fast discontinuities	78
5.3	Horizontal mixing of components	79
5.3.1	Depth-averaged slip	79
5.3.2	Phase diffusion	80
6	A model based on the theory of mixtures	81
6.1	Mixture theory	81
6.1.1	Single component equations	81
6.1.2	Bulk formulation	82

6.1.3	First species mass conservation	82
6.2	Slip velocity	83
6.3	Evolution of the concentration	84
6.3.1	Sedimentation	84
6.3.2	Phase diffusion	85
6.4	Depth-Integration	85
6.4.1	Mass- and Momentum equation	86
6.4.2	Concentration equation	86
6.4.3	Vertical center of mass	87
6.5	Summarized formulation	89
6.6	Hyperbolic properties	90
6.7	Pure sedimentation and basal fluid pressure	90
6.8	Relevance of the depth-averaged mixture model	91
7	Numerical solution of the suspension model	93
7.1	General framework	94
7.1.1	Hyperbolic systems	94
7.1.2	Finite volume formulation	95
7.2	Homogeneous system	98
7.2.1	HLL Wave speeds	98
7.2.2	Empirical Convergence	99
7.2.3	Two-dimensional column collapse	100
7.3	One-dimensional Riemann examples	102
7.4	Momentum relaxation and phase diffusion	104
7.4.1	Invariant and variant part of the relaxation	105
7.4.2	Relaxation in the Runge-Kutta Heun scheme	106
7.4.3	Momentum relaxation in the uniform suspension model	108
7.5	Frictional source terms	109
7.5.1	Component dependent friction	109
7.5.2	Lateral mixing	113
8	Outlook: Realistic test cases	117
8.1	Chute flow	117
8.1.1	General setting	117
8.1.2	Choice of the friction parameter	119
8.1.3	Separation of components	120
8.2	Simulation in realistic terrain	121
8.2.1	RAMMS - Rapid Mass Movements	122
8.2.2	A debris flow at Illgraben	124
8.2.3	Outlook	125
	Bibliography	127
	Curriculum Vitae	135

List of Figures

1.1	Different zones of a debris flow	6
1.2	Formation of lateral levees	7
1.3	Longitudinal cut through a single debris flow surge	8
1.4	Mixture of particles in a fluid at its stationary state	10
1.5	Evolution of the effective fluid pressure with sedimentation	11
1.6	Shear stress in different vertical states of the mixture	12
2.1	Illgraben overview	18
2.2	Illgraben instrumentation	19
2.3	USGS - Large-scale Debris Flow Flume	20
2.4	USGS - Basal fluid pressure measuring devices	21
2.5	Illgraben event results, 28th May 2005	25
2.6	USGS flume results	26
3.1	Coordinate system, basal profile and free surface of the flow	32
3.2	Motion of a material point on an interface	33
3.3	Normal, shear and effective stress at the bottom surface	34
3.4	Typical velocity profile	39
4.1	Two stratified fluids - the upper contains suspended particles	46
4.2	Motion of a material point on an interface in a mixture	49
4.3	Uniform suspension	56
4.4	Two-layer shallow flow	59
4.5	Combined approach	64
5.1	Hyperbolic region of the uniform suspension system	71
5.2	Characteristic polynomial along a path through the phase space	72
5.3	Hyperbolic region for different momentum shape factors	73
5.4	Celerity weights in the phase space	74
5.5	Exact and approximated celerity weighting factors as functions of m^* and u^*	75
6.1	Sedimentation in the multi-phase mixture formulation	91
7.1	Column collapse problem, 1st and 2nd order numerical solution	101
7.2	Initial Data of the 1D Riemann problem	102
7.3	Phase space with initial configuration and solution path	103
7.4	Computed single component masses at $t_{final} = 0.4$	104

7.5	Solution to the Riemann problem for the simplified model	105
7.6	Consistency factor $R(z)$ and analytical solution	106
7.7	Consistency factor $R(z)$ and exponential function for different relaxation factors $r(z)$	108
7.8	Riemann problem evaluated for different τ	109
7.9	Component dependent friction - negligible momentum exchange	110
7.10	Component dependent friction - strong momentum exchange	111
7.11	Lateral mixing on an incline τ being small	114
7.12	Lateral mixing on an incline τ being big	115
8.1	Topography and geometry of the USGS Flume	118
8.2	Contour plot of the Calibration run	120
8.3	Separation of components on the chute	121
8.4	Flow chart of a simulation in real terrain	122
8.5	Georeferenced map and a DEM of the Illgraben area	123
8.6	Illgraben simulation: 28th May, 2005; 3d view	124
8.7	Illgraben simulation: 28th May, 2005; 2d view	125
8.8	Illgraben simulation (3d view) with a large initial volume of 500'000 m ³	126

List of Tables

2.1	Listing of the major Illgraben events in 2005	19
2.2	Significant physical parameters in a debris flow	22
2.3	Dimensionless numbers for the debris flow process	23
2.4	Approximated dimensionless quantities	24
2.5	Summary of assumptions for existing debris flow models	27
7.1	Empirical order of convergence for different test runs	100
8.1	Measured versus calculated values at the USGS Flume	119

Zusammenfassung

Murgänge zählen zu den typischen Naturgefahren in den Gebirgsregionen dieser Welt. Sie bestehen aus einem Gemisch von Wasser, Sedimenten, Steinen und Geröll und können, je nach Fließvolumen, zu sehr großen Verwüstungen führen. Um das Risiko zu mindern und mögliche Schutzmassnahmen zu treffen (Errichtung von Schutzdämmen, flexible Ringnetze), wird seit Jahren intensiv die Dynamik von Murgängen erforscht. Mathematische Modelle setzen das entwickelte Prozessverständnis um und stellen die Grundlage für numerische Simulationen dar. Letztere finden immer häufiger Anwendung in der Gefahrenzonenkartierung.

Diese Dissertation beschäftigt sich mit der mathematischen Modellierung von Murgängen als zwei-komponenten Mischung (flüssig, fest) und deren numerischer Simulation. Ein Vergleich klassischer Modelle mit experimentellen Daten zeigt deutlich, dass bestimmte Aspekte des Fließprozesses nur unzureichend beschrieben werden. Ein Grund hierfür ist die Vernachlässigung der vertikalen Relativbewegung zwischen den einzelnen Komponenten. Letztere ist jedoch für die Modellierung von Sedimentation und Resuspension innerhalb des Fließkörpers wesentlich. Im Rahmen dieser Arbeit werden nun, ausgehend von Mischungstheoretischen Grundlagen, Modellgleichungen hergeleitet, welche eine vertikale Variabilität explizit zulassen. Ferner werden Aspekte der numerischen Lösung und Implementierung diskutiert.

In den ersten beiden Kapiteln wird die Notwendigkeit einer Generalisierung klassischer Murgangmodelle motiviert. Es wird zunächst das für den weiteren Verlauf der Arbeit notwendige Begriffsgebäude eingeführt und wesentliche physikalische Effekte in Partikel-Fluid Mischungen diskutiert. Darauf aufbauend werden zwei experimentelle Murgangdatensätze analysiert und miteinander verglichen. Als Hauptresultat ergibt sich, dass eine variable, vertikale Struktur bei der mathematischen Modellierung von Murgängen berücksichtigt werden muss.

Murgänge weisen eine flache Fließgeometrie auf, zugehörige mathematische Modelle werden daher in einer höhen-gemittelten Art und Weise formuliert. Im dritten Kapitel wird der mathematische Rahmen für eine solche Integration am Beispiel des Savage-Hutter Modells bereitgestellt. Die nachfolgenden Betrachtungen für Mischungen orientieren sich an dieser grundlegenden Herleitung. Es werden grundsätzlich zwei verschiedene Zugänge verwendet: Der erste basiert auf einer expliziten zwei-phasen Beschreibung der Einzelkomponenten und wird in den Kapiteln vier und fünf diskutiert. Der zweite baut auf den Bilanzgleichungen der Gesamtmischung auf und ist Thema des sechsten Kapitels.

Die zwei-phasen Formulierung ist durch eine dichte-gewichtete, vertikale Integration der Bilanzgleichungen in den Einzelkomponenten gegeben. Im Gegensatz zu homogenen, isotropen Materialien ist die Dichte bei Mischungen im Allgemeinen variabel. Im resultierenden System tauchen daher, neben den Massen und Geschwindigkeiten, auch die vertikalen Massenschwerpunkte als Systemgrößen auf. Für homogene Suspensionen und vertikal entmischte Fließkörper werden explizite Modellabschlüsse hergeleitet. In einem kombinierten Modellansatz stellen Sedimentations- und Resuspensionsprozesse die Dynamik zwischen den beiden betrachteten Grenzfällen dar.

Im fünften Kapitel wird ausführlich die hyperbolische Struktur homogener Suspensionen analysiert. Das Modell ist, ähnlich den Zwei-Schichten-Flachwassergleichungen, bedingt hyperbolisch. Jedoch sorgt der vorhandene Impulsaustausch zwischen den Komponenten dafür, dass die physikalisch relevanten Systemzustände im hyperbolischen Bereich liegen.

Auch für die Gleichungen der Mischungstheorie wird die Höhenmittelung für variable, vertikale Dichte durchgeführt. In diesem Fall wird ein Abschluss für den vertikalen Massenschwerpunkt rigoros aus dem ersten Moment der Gesamtmassenbilanz hergeleitet. Das resultierende System ist für positive Massen strikt hyperbolisch und stellt sich als direkte Verallgemeinerung der Flachwassergleichungen dar.

Das siebte Kapitel konzentriert sich auf die numerische Lösung des Suspensionsmodells. Das System partieller Differentialgleichungen besteht im wesentlichen aus drei Anteilen: (1) dem homogenen Fluss, (2) der Relaxation und (3) der effektiven Beschleunigung. Sukzessive wird die Diskretisierung der Einzelanteile diskutiert und schließlich zu einem Gesamtlöser zusammengesetzt. In numerischen Beispielen an der schiefen Ebene werden Entmischung der Komponenten in Fließrichtung und Phasendiffusion orthogonal zur Fließrichtung demonstriert.

Im letzten Kapitel werden Simulationsergebnisse zweier ausgewählter komplexer Geometrien vorgestellt. Zunächst wird eine experimentelle Murgangrutsche, danach eine realistische Topographie realisiert. Die Beispiele entsprechen den Rahmenbedingungen der im einführenden Abschnitt verwendeten Datensätze. Das letzte Kapitel muss als erster, erfolgreicher Schritt in Richtung der Realisierung komplexer Testfälle gesehen werden und liefert als solcher den Grundstock für zukünftige Forschungsbestreben.

Summary

Debris flows are dangerous natural hazards occurring in mountainous areas throughout the world. The flow mass consists of a heavy, dense mixture of water, sediment, and boulders of different sizes, which can cause tremendous devastation. In recent years the mechanics of debris flows has been the subject of intensive research, the primary goal being to understand the factors leading to debris flow initiation and finding an appropriate physical description of debris flow motion. Land planning measures (e.g. hazard maps) and protection measures (e.g. debris flow dams, flexible wire barriers) require a detailed understanding of debris flow mechanics.

The subject of this thesis is the formulation and numerical solution of a system of equations describing the flow of a two-component (fluid, solid) debris flow mixture in complex terrain. A comparison between existing models and experimental data indicates, that simplifying assumptions presently employed in debris flow practise cannot accurately describe the motion of two-component mixtures. The primary reason for this is the disregard of the vertical slip velocities between the single components. However, a formulation with vertical, relative velocities is essential to describe settling and re-suspension processes within the flowing body. In this work, model equations are derived, that explicitly account for a varying, vertical distribution of mass by considering possible slip between the components. This also implies the developing of an appropriate numerical solution technique.

In chapters one and two, the necessity for generalizing existing debris flow models is motivated. The required terminology is introduced and fundamental physical effects in particle-fluid mixtures are discussed. Two experimental data sets are analyzed and compared. The main conclusion of the introductory chapters is, that a realistic mathematical debris flow model has to account for a time-dependent, vertical structure.

Debris flows exhibit a shallow flow geometry. Hence, models are formulated in a depth-integrated fashion. The third chapter provides the mathematical framework for the depth-integration similar to the well-known derivation of the Savage-Hutter or St. Venant equations. All following considerations concerning mixture-models for debris flows are based on this fundamental derivation. Two approaches are considered: The first is based on an explicit description in the single components, which is discussed in chapters four and five. The other is built upon the bulk equations in the theory of mixtures and is the topic of the sixth chapter.

The explicit two-phase formulation is given by a density-weighted, vertical integration of the single-component's balance laws. In contrast to a homogeneous, isotropic material,

the bulk density with mixtures is variable in general. Hence, next to the components' masses and velocities, the vertical center of masses appear as additional variables in the resulting equations. For a uniform suspension and a complete, vertical segregation, explicit closures are derived. In a combined modeling approach, settling and re-suspension processes provide the necessary dynamic transition between those two limits.

In the fifth chapter, the hyperbolic structure of the uniform suspension limit is analyzed in detail. Similar to the two-layer shallow water equations, it is conditionally hyperbolic. However, the available momentum exchange between the species assures that the physically relevant states of the system are within the hyperbolic domain.

In chapter six, the balance laws for the bulk mixture are integrated with respect to varying densities. Here, a closure for the vertical center of mass is derived rigorously by depth-integrating the first moment of the bulk mass conservation. The resulting system is strictly hyperbolic for positive masses and therefore is a direct generalization to the single phase shallow water equations.

Chapter seven concentrates on the numerical solution of the suspension model. The system of partial differential equations essentially consists of three different parts: (1) the homogeneous flux, (2) the relaxation, and (3) the effective acceleration. The discretization of the single contributions is discussed and summarized into a complete numerical solution scheme. Numerical examples on the inclined plane demonstrate the segregation of components in flow direction and the phase diffusion orthogonal to the flow.

In the last chapter, results of two simulations in complex topography are presented. The first is a simulation of a flow in an experimental debris flow chute. A realistic case in complex terrain is presented to further test the model. The latter examples correspond to data sets that have been analyzed in the introductory chapters. This last chapter has to be seen as an initial step towards the simulation of realistic test-cases in complex topography. Hence, it provides the basis for future research activity.

Chapter 1

Introduction to Debris Flows

The Alpine arc in the heart of Europe is one of the most famous mountain ranges in the world. The population density is high. With an average of over 200 inhabitants per square kilometer in the habitable area, the Alps belong to the most densely populated regions in the world. The Alps are subject to natural hazards, such as avalanches, debris flows and rockfall. Between 1972 - 2002 debris flows alone in Switzerland caused the death of 20 people, as well as damage to the amount of 360 Mio CHF ¹. Therefore a tremendous effort is made to avoid fatalities and to minimize damage potential against debris flows.

Within this Chapter a general introduction to debris flow phenomena is provided. This includes a rough description and definition of the process, as well as a section on the terminology, that defines the necessary notation. As it will be fundamental for the ongoing of this thesis, the effective stress principle is summarized with respect to the debris flow process. Finally, a selective summary on past and present research activities in the field is provided.

1.1 Classification and Definition

A debris flow is a special form of a landslide, the latter being the name for a whole range of different geophysical mass movements. According to Cruden [24] a landslide is defined as *the movement of a mass of rock, debris or earth down a slope*. A further classification includes the differences in movement type and velocity, composition of the incorporated material, morphology, geometry, size and activity (compare [91, 25, 51]). For the purpose of this work, the important characteristics are the composition of the material and the type of movement, which can be summarized as follows:

- **Material:** Mixture of poorly sorted sediment or even organic material, of a range of different sizes ($65\mu\text{m}$ up to several meters) and a fluid phase, given by a viscous slurry. The latter is also called the fluid matrix of the flow, it is given by water mixed

¹WSL Storm Damage Database

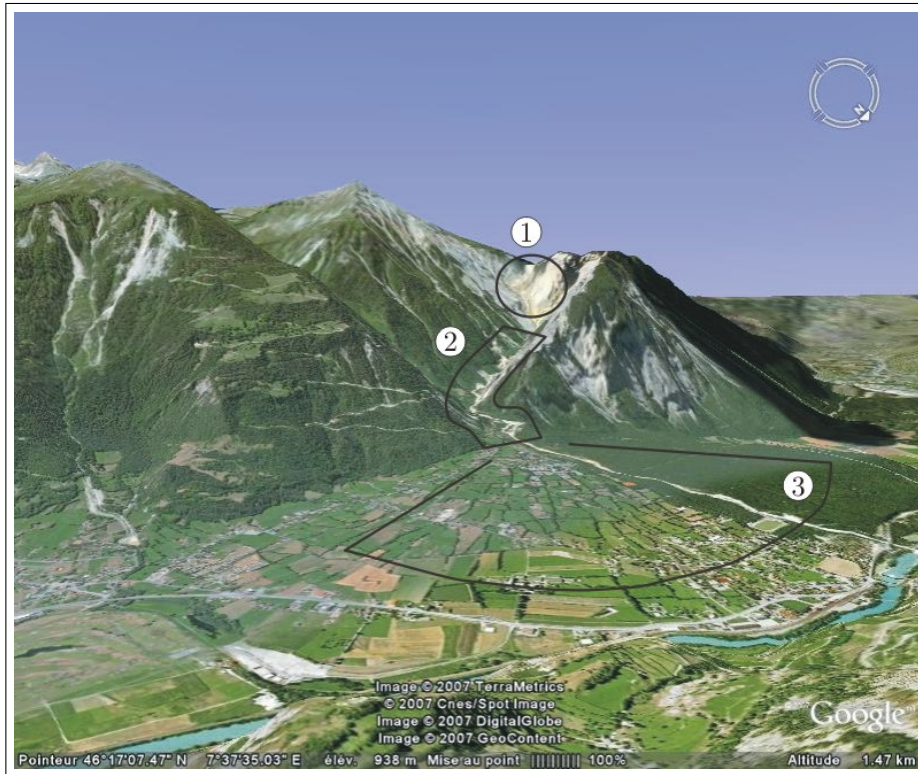


Figure 1.1: Different zones of a debris flow: 1) Initiation zone 2) Transit zone 3) Deposition zone

with very fine particles ($< 65\mu\text{m}$). The solid content changes with the position in the flow, and usually varies between 30-80%.

- **Movement:** Debris flow volumes in the Alps range between 10^3 - 10^6 m^3 , but there are also recorded flow events that carry a bulk volume up to 10^7 m^3 . Usually, their flow paths are determined by pre-existing corries, in which the debris flows in surges. Channel gradients vary from about 40° in the starting zone to 3° in the deposition zone (compare Figure 1.1). Depending on the given topography velocities can be as high as 15 ms^{-1} .

A rigorous specification of landslides with respect to debris flows can be found in Hungr et al. [38] or in the description of a debris flow provided by Rickenmann in [40].

Considering the complexity of a debris flow, it might seem difficult to formulate a manageable definition, that covers all details. In fact, many of the definitions provided in the literature, specialize on certain aspects of the flow, either on the composition of the material, the morphology, or, as it is done within this thesis, on the dynamical and mechanical processes. For the purpose of this work the definition formulated by Iverson [44] is most suitable:



Figure 1.2: Formation of lateral levees (Sertig Dörfli - 5.10.2006)

Debris flows are churning, water-saturated masses of fine sediment, rocks, and assorted detritus that originate on mountain slopes and course down stream channels when they reach valley floors. Strong interactions of solid and fluid forces greatly influence the behavior of debris flows and distinguish them from related phenomena such as rock avalanches and water floods.

1.2 Terminology

1.2.1 Initiation, Transit, and Run-out zone

For a debris flow event, three different zones have to be defined in order to discuss the correct rheological behavior of a debris flow from initiation to run-out (compare Figure 1.1). In the first zone loose material is released, meaning that some mechanism is required to initiate the flow. In the European Alps two main processes are considered to be relevant source mechanisms for debris flow initiation: Either (1) saturated soil fails instantaneously and the debris flow starts as a landslide or (2) solid material, mostly loose as a consequence of erosion, is entrained into surface water flow. The region, where those two processes occur is called the **initiation zone**.

In the **transit zone**, the debris flow has developed into one or more single debris flow surges. A schematics of a longitudinal cut through a single surge is given in Figure 1.3.

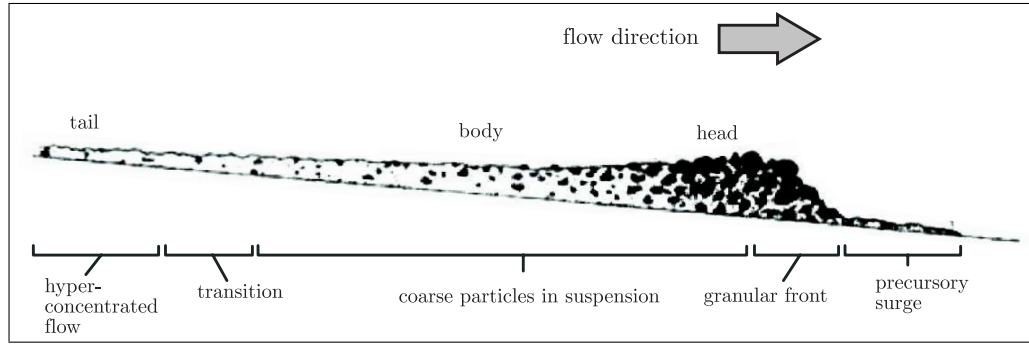


Figure 1.3: Longitudinal cut through a single debris flow surge with a granular front

If there are coarse particles in the flow, the surge exhibits a granular front, whereas roll-waves are typical for small particle suspensions. However, the transition between different flow regimes is smooth and in the complete absence of any coarse particles mud-flows arise. Within this thesis the focus will clearly be on flows with a granular front. In the transit zone material is constantly deposited from and entrained into the flowing body and the flow is influenced by the underlying basal topography. Particles of different sizes are redistributed, such that eventually levees can form at the sides of the flow. An example of lateral levees can be seen in Figure 1.2.

Finally, the bulk movement decelerates and stops, because internal and basal friction forces overcome the inertial forces and gravitational acceleration. This is considered as the **deposition zone**.

1.2.2 A single debris flow surge

A single debris flow surge with a granular front can be divided into distinct regions, sketched in Figure 1.3. Prior to the flow front there will be a non-trivial material discharge referred to as the **precursory surge**. It is characterized by small flow heights and a solid concentration that increases towards the arrival of the actual **granular front**. The latter is also called the **head** of the flow. Here, particles are not suspended and in the very first section of the front the mixture may not be fully saturated. In the third zone, or **body** of the flow, the coarse particles are in suspension. Eventually the solid concentration within the surge decreases and it turns into a **hyper-concentrated stream** or **mud flow**. This last part is also called the **tail**.

1.3 Effective stress and fluid pore pressure

The effective stress concept has initially been developed for soils by Terzaghi in 1936 [86, 11]. It is an engineering approximation based on experiments to determine the stresses in a water-soil mixture and, for the purpose of this thesis more importantly, it can be

straight-forwardly generalized to high-concentrated fluid-particle mixtures [71]. Most introductory books on soil mechanics or geotechnical engineering include the basic ideas, a good description is provided in the book by Holtz [37], which serves as a basis for the following summary.

1.3.1 Stationary state of a particle-fluid mixture

Let us consider a vertical column of a mixture of a Newtonian fluid and solid particles, as it is sketched in Figure 1.4. The mixture is saturated, meaning that the filling level h is given by the fluid, and all particles are completely covered. The material densities of the components are denoted by $\rho_{f,0}$ (fluid) and $\rho_{s,0}$ (particles). For $\rho_{f,0} \neq \rho_{s,0}$ the particles are not neutrally buoyant. Thus, in the absence of other than the gravitational force, the stationary state of the material is well-defined. Within the scope of this work, it is assumed that $\rho_{f,0} < \rho_{s,0}$, such that in a stationary state, all particles have settled down to the ground. The total mass of the solids m_s and the surrounding fluid m_f respectively per infinitesimal area dx is given by

$$m_s := \int_0^h \rho_{s,0} 1_s dz \quad m_f := \int_0^h \rho_{f,0} 1_f dz \quad (1.1)$$

Here, 1_s and 1_f denote indicator functions for the solid and the fluid component. Then the hydrostatic fluid pressure \mathbf{P}_h and total vertical stress \mathbf{N}_{tot} evaluated at the base are given by

$$\mathbf{P}_h = g\rho_{f,0} h \quad \mathbf{N}_{\text{tot}} = \int_0^h g\rho dz = g(m_s + m_f) \quad (1.2)$$

where $\rho := \rho_{s,0}1_s + \rho_{f,0}1_f$ is the point-wise density at any location within the mixture and it is not constant throughout the depth in general. It is important to note, that the relation for the fluid pressure holds true only if the void space between the grains allow for a continuous fluid network.

Total vertical stress and fluid pressure can also be evaluated at every height z throughout the mixture and are thus given as functions of z . Terzaghi stated in 1936 [86], that the inter-granular or effective stress \mathbf{N}_{eff} , that causes displacements within the grains, is given by

$$\mathbf{N}_{\text{eff}} := \mathbf{N}_{\text{tot}} - \mathbf{P}_h. \quad (1.3)$$

A straight-forward calculation shows, that $\mathbf{N}_{\text{eff}} = \int_0^h g(\rho_{s,0} - \rho_{f,0}) 1_s dz$, such that in the stationary state the effective stress is nothing but the vertical stress of the solids with respect to the buoyancy-reduced weight.

1.3.2 Suspension limit of a particle-fluid mixture

We now consider the other limit, as it may be present in the body of a debris flow (compare Figure 1.5). All particles are in suspension, such that none of them touches the ground.

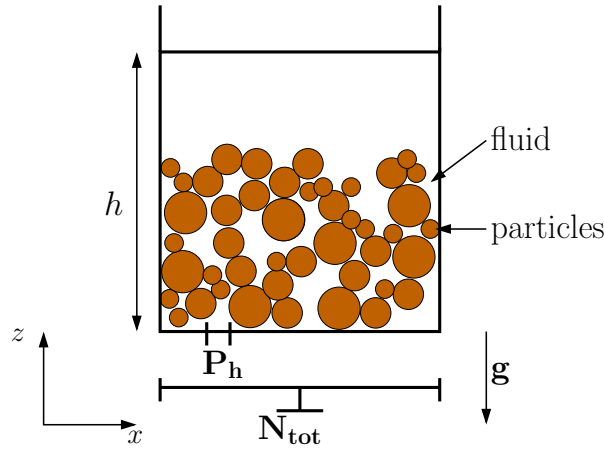


Figure 1.4: Mixture of particles in a fluid at its stationary state

Furthermore the settling velocity is considered to be small, such that dynamic pressure contribution in the fluid may be negligible. Mass conservation implies, that the total vertical stress is still the same. But since all particles are in suspension the effectively measured fluid pressure \mathbf{P}_{eff} , also called the fluid pore pressure, evaluated at the ground coincides with \mathbf{N}_{tot} .

$$\mathbf{P}_{\text{eff}} = \mathbf{N}_{\text{tot}} = \int_0^h \rho g dz = (m_s + m_f)g \quad (1.4)$$

The excess fluid pore pressure is now defined as the difference between the effectively measured fluid pore pressure at the ground and the hydrostatic fluid pressure, that would be present in the stationary state

$$\mathbf{P}_{\text{ex}} := \mathbf{P}_{\text{eff}} - \mathbf{P}_{\text{h}} \quad (1.5)$$

Thus knowing m_s , m_f and the pure density of the fluid $\rho_{f,0}$, \mathbf{P}_{ex} acts as a measure for the amount of particles that have no direct or indirect contact to the ground. They are said to be in suspension.

1.3.3 Dynamic transition

For a non-stationary state of the mixture, Terzaghi's effective stress principle generalizes to

$$\mathbf{N}_{\text{eff}} := \mathbf{N}_{\text{tot}} - \mathbf{P}_{\text{eff}} \quad (1.6)$$

We can easily see, that in the limit of a uniform suspension the inter-granular stress \mathbf{N}_{eff} is zero. During the sedimentation more and more particles reach their stationary state and define a level k referred to as the sedimentation line. During the process of sedimentation, it increases in time. In the same time the effective fluid pressure \mathbf{P}_{eff} decays from the total vertical stress \mathbf{N}_{tot} to the hydrostatic fluid pressure in the stationary state \mathbf{P}_{h} . Or equivalently, the excess fluid pore pressure \mathbf{P}_{ex} decays from $\mathbf{N}_{\text{tot}} - \mathbf{P}_{\text{h}}$ to $\mathbf{0}$. Within the chosen framework, the decay of \mathbf{P}_{ex} is due to the settling of grains and one would derive

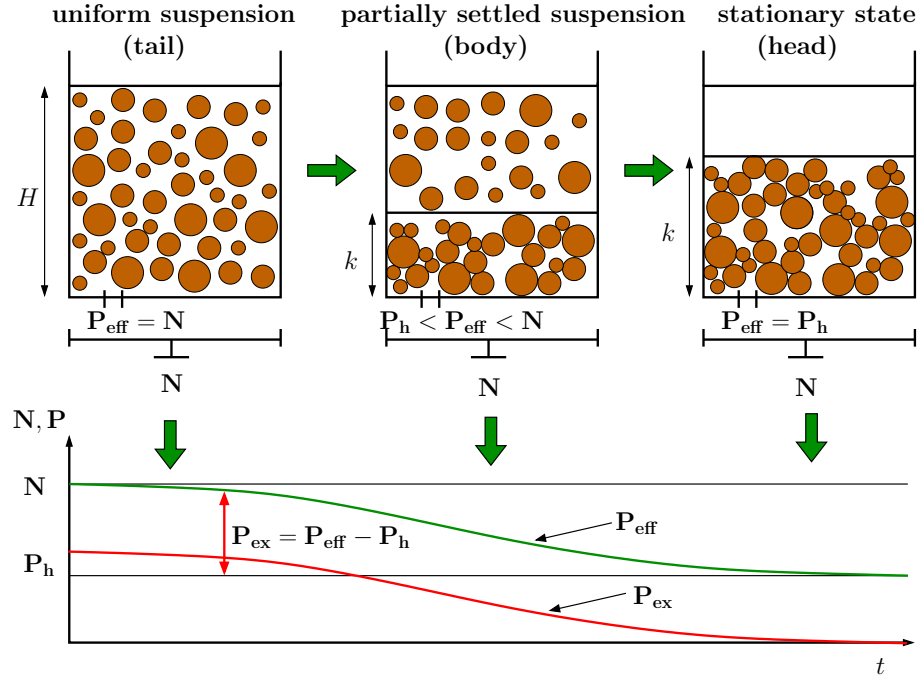


Figure 1.5: Evolution of the effective fluid pressure at the base with sedimentation of particles

an explicit time dependent formula by imposing a hindered settling velocity (compare [56, 9, 10]) on the particles. An alternative standpoint can be found, if the observer takes the view of the fluid rather than the solid. The fluid diffuses through the voids whereas the soil is consolidated. The essential formula of 1D consolidation theory, a diffusion equation for the pore water during the process of consolidation is again due to Terzaghi and given by

$$\partial_t \mathbf{P}_{\text{eff}} = K \partial_z^2 \mathbf{P}_{\text{eff}} \quad (1.7)$$

In the original work the diffusion coefficient K is called the coefficient of consolidation because it contains the material properties that govern the consolidation process, which are: Darcy coefficient of permeability, compressibility, void ratio of a maximum packing for the considered particles, pure fluid density and gravitational acceleration.

1.3.4 Stress concepts in a debris flow

In order to relate the introduced stress concepts to debris flows a very simple box model is considered. A vertical column filled with a fluid-particle mixture is assumed to slide downwards on an inclined plane with a velocity \mathbf{U} . The simple flow situation is indicated in Figure 1.6. The forces acting on the moving mass are then given by (1) gravitational acceleration and (2) resisting shear that is determined by some friction law. The force due to gravitational acceleration acts in direction of the flow, whereas the shear force counteracts the flow direction.

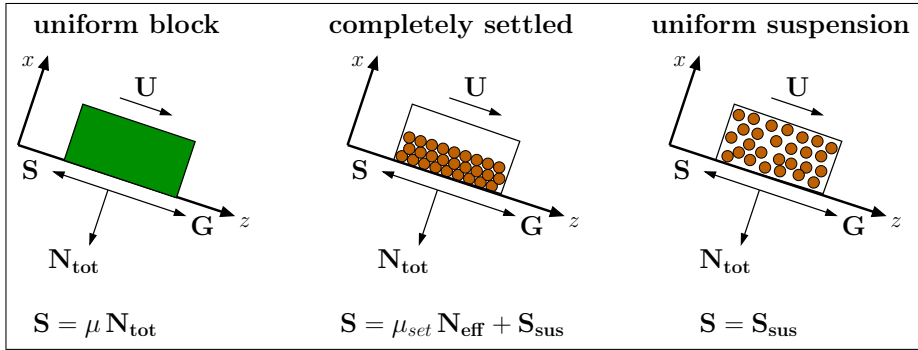


Figure 1.6: Shear stress in different vertical states of the mixture

A well-known friction law for solid materials, that is also applied in the field of granular matter sliding down an incline, is given by the Coulomb dry friction relation. It states that shear and total normal force on the plane are proportional with the coefficient of proportionality denoted by μ .

$$\mathbf{S} = \mu \mathbf{N}_{\text{tot}} \quad (1.8)$$

One approach is, to split the shear resistance of a fluid-particle mixture into two parts. The first contribution, denoted by \mathbf{S}_{set} , is due to the settled particles the other one, \mathbf{S}_{sus} , is due to the fluid, that may contain suspended particles.

$$\mathbf{S} = \mathbf{S}_{\text{set}} + \mathbf{S}_{\text{sus}} = \mu_{\text{set}} \mathbf{N}_{\text{eff}} + \mathbf{S}_{\text{sus}} \quad (1.9)$$

It is common practise, to close the settled particles contribution by a Coulomb friction law with respect to the effective normal force (compare for example [44]). In a uniform suspension the effective inter-granular stress \mathbf{N}_{eff} is essentially zero and the complete basal shear is determined by the friction law for the fluid. The fluid contribution reduces to the minimal hydrostatic part, when all particles have direct or indirect contact to the ground.

Both mixture types and actually all intermediate states are present in debris flows with a granular front. Within the body and the tail, coarse and fine particles are in suspension, whereas in the head of the flow, the particles are settled (compare Figure 1.3). The previous considerations now result into an essential implication for any debris flow model: It is crucial to know the vertical state of the mixture, as the amount of suspended and settled particles influences the basal and internal friction in a particle-fluid mixture. However, to know the absolute amount of either component in the column alone is not enough. Then, a reconstruction of the necessary information on the vertical state is not possible.

1.3.5 Extension to a multi-dimensional stress state

A concluding remark is devoted to the extension of the effective stress concept to a multi-dimensional stress state. Iverson and Denlinger [44, 47, 64] generalized the principle in

a consistent way to the established conventions in soil mechanics, to the mixture stress tensor σ , that will later be needed in the general derivation of the model equations.

$$\sigma_{\text{tot}} = \sigma_{\text{eff}} + \mathbf{p}_{\text{eff}} \mathbf{I} + \phi_f \sigma_{\text{f,dev}} \quad (1.10)$$

Here σ_{eff} denotes the effective stress, \mathbf{p}_{eff} the absolute value of the previously introduced effectively measured fluid pore pressure. The latter acts isotropically and is therefore multiplied by the identity matrix \mathbf{I} . $\sigma_{\text{f,dev}}$ denotes the deviatoric stress in the fluid component and as it is present only in the fluid. It is multiplied by ϕ_f the fluid volume fraction or pore space of the mixture. In the absence of horizontal velocities, relation (1.10) reduces to Terzaghi's effective stress concept (1.6).

1.4 Current Debris Flow research

Since 1910, when Stiny [82] published first results on the subject, considerable debris flow research has been carried out, especially in the last two decades. An introduction to the vast field is provided by the proceedings of three International Conferences on Debris-Flow Hazards Mitigation: Mechanics, Predictions, and Assessment [18, 92, 72, 73] as well as by the book [64]. With respect to mathematical modeling, important developments are summarized in the following.

All mathematical debris flow models are conceptually idealized as either

- a homogeneous mixture, that can be treated as a single-component media
- a two-component mixture (fluid-solid or diffusive).

Hence, when it comes to deriving a system of partial differential equations for the dynamics of debris flows, two corresponding classes of models exist.

1.4.1 Homogeneous mixture approach

Models that are based on a homogeneous mixture approach treat the whole flowing body as one-single phase with a non-Newtonian rheology. Constitutive relations for the rheology of mud flows have been analyzed by Costa [21] and Coussot [22]. For granular front flows, similar work has been done by Takahashi [84, 85] and an overview on existing constitutive relations is given by Jan and Shen [52]. The homogeneous mixture concepts have been very successfully applied to mud-flows [26, 22], whereas they turned out to give unsatisfactory results for flows with a granular front, especially with respect to velocity profiles and solid concentrations [46].

1.4.2 Iverson's model

Iverson stated in a comprehensive review on the physics of debris flows [44], that a model that can cover for a granular front should be capable to describe the whole process from initiation to deposition. This makes the separate consideration of the different species necessary and leads to the second class of existing debris flow models. He proposed depth-averaged fluid-solid mixture equations, a discussion of which can also be found in [47, 48]. The system is derived along the lines of the Savage-Hutter model (SHM) for shallow granular flow [77, 70]. In fact, it can be seen as a direct generalization, as it reduces to the very same in the absence of any fluid. Both the SHM and Iverson's model are strictly hyperbolic systems of conservation laws, that are linearly degenerated only in the case of zero flow heights. Hence, they are closely related to the well-known shallow water equations (e.g. [58]). Therefore, results on its numerical solution could be adopted without difficulty.

Iverson's model did not fully satisfy the demand of being able to reproduce the flow behavior from initiation to deposition. This is mainly due to the fact, that the assumptions on the mixture are too restrictive, as it assumes a constant mixture density. Consequently vertical or horizontal slip of the species is not possible. However precisely these relative movements produce many of the flow characteristics (segregation, granular front, sedimentation). Still, Iverson's results are significant, since his model overcame the assumption induced problems by imposing a pore pressure evolution equation on the system. This was justified by experimental measurements on the USGS large scale chute [49].

1.4.3 Multi-component mixture approach

A different way to generalize the mixture theory concepts, is to relax the restrictive assumptions of a constant mixture density directly. Instead of considering the mixture, the balance laws for the single components have been depth-averaged directly, such that one can track each components' velocities and horizontal relative movement is possible. A first effort in this direction is due to Bozhinskiy [14] and a model with an extensive derivation is suggested by Pitman and Le [68]. The latter was reformulated by Pelanti et. al. [67] to recover the bulk mixture momentum balance. However, to overcome subtleties in the derivation all of these implicitly assumed a vertical mixture distribution basically given by a uniform suspension. The resulting systems lack the mathematical property of hyperbolicity [67]. This is also known from the two-layer shallow water theory [4] and once again similarities between the models are such that results for the numerical approximations [1, 12] can be adopted and applied to geophysical mass movements [17].

1.4.4 Motivation

Experimental data on the fluid pressure distribution throughout a debris flows clearly indicate, that the vertical structure within the flow must not be neglected, as it has

strong influence on the flow dynamics [49, 62]. Since this is a crucial point and serves as a motivation for the later modeling work, we will demonstrate this also in the following Chapter 2 on debris flow experiments. The difference between fully and partly suspended sections has been described from a phenomenological point of view in the previous section. The previously mentioned formulation of a pore pressure evolution equation by Iverson [48, 47] can be interpreted as an attempt to code information on the vertical structure within the system, but until now no effort has been done to account for vertically varying particle distributions in shallow fluid-solid mixture flows.

Chapter 2

Experimental data sets

This chapter introduces two experimental data sets for debris flows. The first is taken from an automated debris flow observation site in real terrain, the second from experiments conducted at an artificial large-scale chute. By performing a dimensional analysis, we will see, that the data sets are dynamically similar, and hence, their results can be compared. Both measurements include fluid pressure results at the base of the flow. These are analyzed with respect to the effective stress concept, introduced in Section 1.3, and compared to existing mathematical models. We will see, that neither of the existing mathematical models describe the process in a satisfactory way, which finally motivates an extension of the existing theory.

2.1 Debris flow measurements

Systematic observation of debris flows is difficult, due to their unpredictable timing, location and magnitude. Comprehensive data sets are therefore rare. One way to overcome this problem, is to install automated devices, triggered by the event itself, directly into the torrent. This idea has been carried out by the Swiss Federal Institute for Forest, Snow and Landscape Research (WSL) at Illgraben - Switzerland. The latter is well known for its high debris flow activity. Instead of waiting for natural events to occur, one can also scale down the flow to laboratory size, according to specified similarity criteria. Flume experiments like are done by the U.S. Geological Survey. Both approaches are introduced within this section.

2.1.1 Real scale events at Illgraben

The Illgraben catchment, located in southwestern Switzerland, extends from the summit of the Illhorn mountain (2716 m above sea level) to the confluence of the Illbach river and the Rhone river (610 m above sea level) [39]. See Figure 2.1 for a picture and a schematic overview. The initiation zone has a size of approximately 4.6 km^2 . Once initiated, the debris flows down in a U-shaped channel, the transit zone. It is between 5-10 m wide

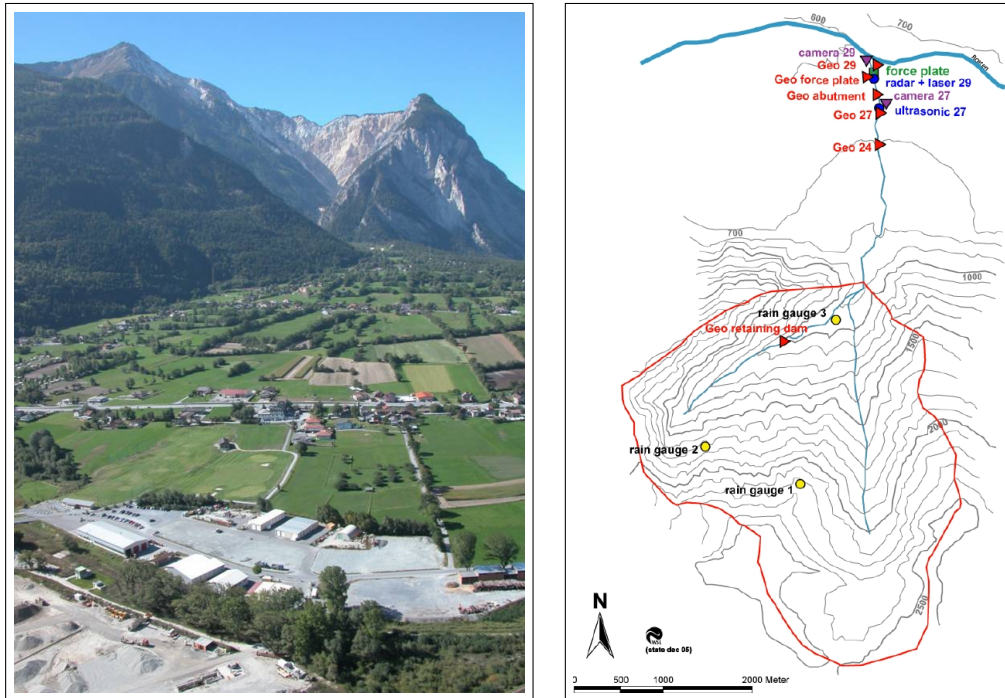


Figure 2.1: L: Illgraben - Initiation, Transition and Deposition zone; R.: Illgraben - schematic overview

and 5 km long, and finally enter into the Rhone. The last 2 km section is inclined by an average inclination angle of 8-10°.

Geophones are installed along the track, the other measuring devices are installed at a location just before the channel ends (compare Figure 2.1 (right)). The instrumentation includes a 8 m² force plate, which measures shear and normal forces at the base, a pressure device to determine the basal fluid pore pressure, and a laser for the flow height above the force plate (compare Figure 2.2). Another height measuring system (this time a radar) is located further upstream. The average front velocity is determined, by correlating geophone signals at the force plate with those 460 m upstream. For further details on debris flow observation results at Illgraben, we refer to [62].

Debris flows at Illgraben generally occur from May to October and follow convective rainstorms [62]. With around 5 events every year, the flow activity is reasonably high. Once a flow is initiated, it passes the geophones along the track. These in return will trigger the measuring devices around the force plate. For an exemplary data set of the year 2005, see Table 2.1.

Like in the 2005 observation season, the first event in the year is usually the biggest one. This is mainly due to the presence of a big amount of eroded, loose material after the winter season. The melting snow mobilizes additional material. The debris flow events (2) through (5) have typical sizes for the Illgraben, the last two are reasonably small. The



Figure 2.2: Illgraben instrumentation - Force plate and height measuring device

2005	28.05. (1)	03.06. (2)	13.06. (3)	04.07. (4)	18.07. (5)	02.08. (6)	18.08. (7)
h_{\max} (upstr.) [m]	1.5	0.8	0.57	0.76	1.5	1.1	0.7
h_{\max} (plate) [m]	2.25	1.1	1.0	1.12	1.7	1.2	0.8
U_{front} [ms^{-1}]	9.0	2.5	5.3	2.8	2.3	1.4	0.7
max. discharge [m^3s^{-1}]	150	21	30	20	27.5	18	7.5
bulk volume [10^3 m^3]	140	30	25	25	19	7	5.6

Table 2.1: Listing of the major Illgraben events and their characteristics in the observation season 2005.

maximum heights at the upstream measurement location ($h(\text{upstr.})$) are systematically smaller, than the ones measured at the force plate ($h(\text{plate})$). This is due to the fact, that the channel width decreases towards the force plate.

2.1.2 Chute experiments

Since 1991, the U.S. Geological Survey (USGS) conducted a series of large-scale debris flow flume experiments. The following paragraph summarizes a description of their facilities and experiments, given in a technical report in 1992 [45].

The USGS, in cooperation with the U.S. Forest Service, constructed a flume to conduct controlled experiments on debris flows. It is located in the Cascades Range foothills, Willamette National Forest, Oregon, and provides excellent research opportunities. The flume is a reinforced concrete channel 95 m long, 2 m wide, and 1.2 m deep that slopes 31°



Figure 2.3: U.S. Geological Survey large-scale debris flow flume - the material has just passed the flume mouth and entered the deposition area [59]

(60%), an angle typical of terrain where natural debris flows originate. Removable glass windows built into the side of the flume allow flows to be observed and photographed as they sweep past.

To create a debris flow, up to 20 m^3 of sediment are placed behind a steel gate at the head of the flume, saturated with water from subsurface channels and surface sprinklers, and then released. Alternatively, a sloping mass of sediment can be placed behind a retaining wall at the flume head and watered until slope failure occurs. The ensuing debris flow descends the flume and forms a deposit on a nearly flat run-out surface at the flume base.

The set of experiments we are referring to in this thesis, is discussed in [49] and includes several 10 m^3 events. The sensors are located at the center-line of the flume 67 m below the head-gate and 7.5 m (in one experiment 14.5 m) beyond the flume mouth. The devices measure fluid pressure and normal stress simultaneously, a schematic of the instruments' configuration is given in Figure 2.4.

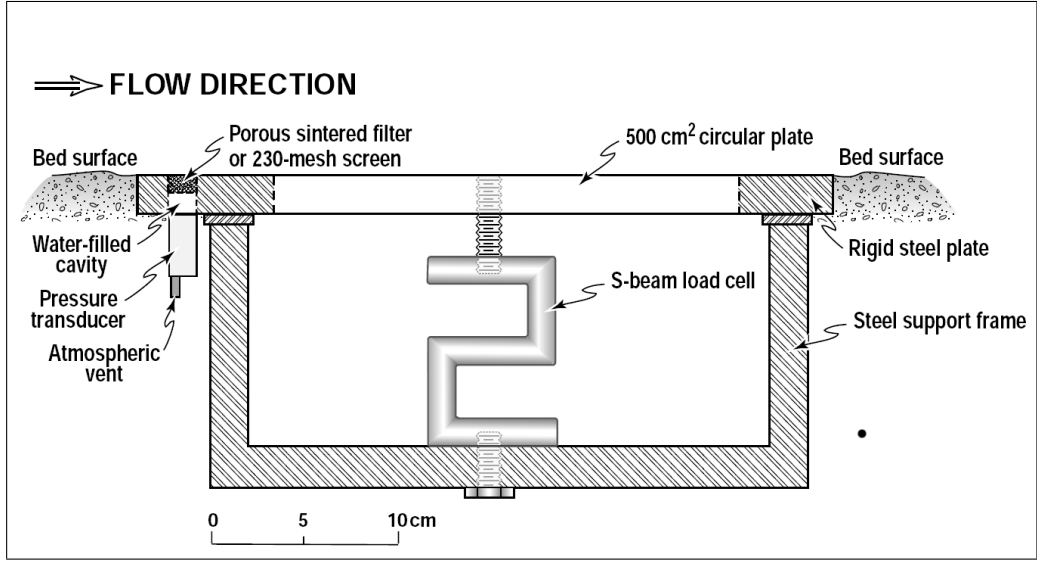


Figure 2.4: USGS- debris flow flume - fluid pore pressure and normal stress measuring devices (from [49])

2.2 Dimensional analysis

In order to compare the Illgraben events and the large-scale flume experiments, a dimensional analysis is carried out. The results of the analysis can also be employed to distinguish different flow regimes and to identify small terms in the final model. Comprehensive work on similarity criteria for debris flows has been done by Davies [26] and Iverson [44]. Ancey and Evesque looked at the frictional–collisional flow regime in detail [2], and for a rigorous theoretical foundation to flow regimes for geophysical flows, see also the work of Coussot [23].

2.2.1 Significant physical parameters

Significant physical quantities in a debris flow are given in Table 2.2. The set includes material properties of the fluid component (density, viscosity), of the solid component (density, internal and basal friction angle, characteristic grain diameter), and of the composite material (density, characteristic relaxation time scale for the momentum exchange, characteristic shear rate). Significant quantities for the kinematics of the bulk debris flow are represented by characteristic height, length, velocity and flow time scale. Finally, characteristic channel slope angle and gravitational acceleration are external constants, which influence the dynamics of debris flows. In the case of full saturation, solid and fluid volume fractions ϕ_s and ϕ_f are given by

$$\phi_s := \frac{\rho - \rho_{f,0}}{\rho_{s,0} - \rho_{f,0}} \quad \phi_f := \frac{\rho_{s,0} - \rho}{\rho_{s,0} - \rho_{f,0}}$$

With these definitions, we get a relation of the form $\rho = \phi_f \rho_{f,0} + \phi_s \rho_{s,0}$, which is the intuitive one.

Physical parameter	Notation	Unit
bulk density	ρ	[kg m ⁻³]
pure fluid density	$\rho_{f,0}$	[kg m ⁻³]
pure solid density	$\rho_{s,0}$	[kg m ⁻³]
char. height	H	[m]
char. length	L	[m]
char. flow time scale	T	[s]
char. velocity	U	[m s ⁻¹]
char. channel slope angle	ζ	[–]
char. relaxation time scale	τ	[s]
internal friction angle	Φ	[–]
basal friction angle	δ	[–]
char. grain diameter	d	[m]
fluid viscosity	ν	[Pa s] = [kg m ⁻¹ s ⁻¹]
grav. acceleration	g	[m s ⁻²]
char. shear rate	$\dot{\gamma}$	[s ⁻¹]

Table 2.2: Significant physical parameters in a debris flow with their notation and unit

2.2.2 Dimensionless groups for debris flows

Twelve quantities of the latter set are dimensional, the appearing three fundamental physical quantities being length m, time s and mass kg. Now, according to the Buckingham Π Theorem [15], nine dimensionless numbers describe the phenomenon equally well (compare [41]). The corresponding set of dimensionless numbers is not uniquely defined. For the purpose of this analysis the choice listed in Table 2.3 seems to be convenient. It is very similar to the dimensionless groups introduced in [44]. Table 2.4 summarized approximations to the first five dimensionless numbers of Table 2.3 for both data sets. That is why their physical relevance is discussed briefly.

The **Shallowness parameter**, given by the ratio between characteristic height scale and characteristic length scale of the flow, is small for most geophysical flows. This will be a crucial assumption for the later applied depth-integration.

The **Mass number** denotes the ratio between the effective solid mass and the effective fluid mass. It contains information on the partitioning of the momentum transport in a fluid-solid mixture. For $M < 1$, fluid momentum transport dominates, whereas for

Dimensionless number	Notation	Definition
Shallowness parameter	ε	$\frac{H}{L}$
Mass number	M	$\frac{\phi_s \rho_{s,0}}{\phi_f \rho_{f,0}}$
Froude number	Fr	$\frac{g \cos \zeta H}{U^2}$
Friction number	F	$\frac{\phi_s (\rho_{s,0} - \rho_{f,0}) g H \tan \Phi}{\phi_f \dot{\gamma} \nu}$
modified Savage number	S	$\frac{\rho_{s,0} \dot{\gamma}^2 d^2}{(\rho_{s,0} - \rho_{f,0}) g H \tan \Phi}$
Acceleration number	A	$\frac{gT}{U} (\sin \zeta - \cos \zeta \tan \delta)$
Sedimentation number	Se	$\frac{\tau g}{U}$
modified grain Reynolds number 1/2	R1/R2	$\frac{\rho_{f,0} \dot{\gamma} d^2}{\nu}$

Table 2.3: Dimensionless numbers for the debris flow process

$M \geq 1$, momentum transport is mainly due to the solids.

The **Froude number** is well-known from river hydraulics. A value less than one implies sub-critical flow ($0 < Fr < 1$), whereas a value greater than one implies super-critical flow ($Fr > 1$).

The **Friction number** is to be interpreted as the ratio between characteristic solid and fluid friction forces. *Within the flowing body, normal forces on planes parallel to the free upper surface approximately balance the weight of the super-incumbent solids, and the Coulomb friction rule, with friction coefficient $\tan \Phi$, describes bulk inter-granular shear stresses on such planes* [50]. The viscous fluid friction is given by the product of shear rate and viscosity $\dot{\gamma} \nu$. Each of the stresses is multiplied by the corresponding volume fraction.

The **modified Savage number** contains information about the inertial shear stress according to grain collisions in comparison to quasi-static shear stress associated with Coulomb friction. However, the value of the Savage number strongly depends on the chosen grain size, such that it can as well be interpreted as a criterion, to distinguish between grains, that are in a collisional dominated regime and those, which are gravitational dominated.

Both data sets deal with shallows flows, in which the Mass number is of the order of one.

Dimensionless number	Illgraben	Flume
Shallowness parameter	$\ll 1$	$\ll 1^\bullet$
Mass number	2 – 3	4*
Froude number	0.3 – 3.7	3.5 [•]
Friction number	$0.6 \cdot 10^6 - 2.4 \cdot 10^7$	$2 \cdot 10^{3*}$
modified Savage number	0.04^Δ	0.2*

Table 2.4: The approximated dimensionless numbers for the real scale Illgraben events are based on the data set of 2005; the ones of the USGS flume experiments are either directly taken from literature (superscript *), or computed from published data (superscript [•]) - for both see [44]. (Δ : for a grain size of 0.5 m)

Hence, solid and fluid components contribute to the momentum transport and have to be considered in a modeling approach. The flume flows are mainly super-critical. Within the set of real scale events we find both, sub- as well as super-critical flow events. The Friction number of both data sets differs by several orders of magnitude. However, both values indicate that the internal friction is mainly due to the solids, whereas fluid viscosity is negligible. From the approximated Savage number we see, that for both data sets, grain collisional forces are small.

2.3 Fluid pore pressure results

2.3.1 Illgraben results

Figure 2.5 shows the results of the first major debris flow in 2005, which took place on the 28th May. With a bulk volume of 140.000 m^3 , it belongs to the largest recorded events at Illgraben. The plot shows the first 15 min of the flow. However it should be noted, that it lasted for another hour. The plot shows the actual measured values, which are visible height H , total normal stress \mathbf{N}_{tot} , effective fluid pressure \mathbf{P}_{eff} and shear stress \mathbf{S} . They are plotted versus time. The third plot shows the effective friction coefficient, which is evaluated from the total normal stress and the shear stress, and defined according to

$$\mu_{eff} := \frac{\mathbf{S}}{\mathbf{N}_{\text{tot}}}.$$

The height data clearly shows the arrival of the front, and the same abrupt increase is seen in the normal stress plot. In contrast to this, the effective fluid pressure data shows

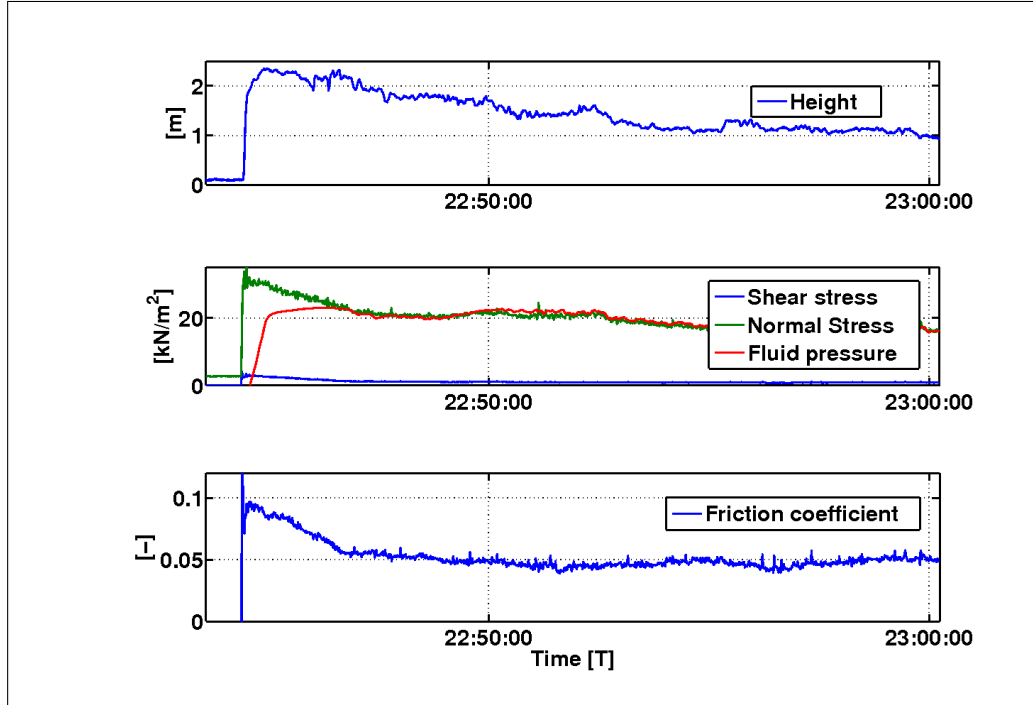


Figure 2.5: Illgraben event results, 28th May 2005 - height H , normal stress N_{tot} , shear stress S and basal fluid pressure P_{eff} measurements in plot one and two; computed effective friction coefficient μ_{eff} in plot three.

a delay, and it should be noted, that this delay is not due to the measuring devices. In the fluid pressure curve, we identify three different regions:

- Close to the front, the increase in the fluid pressure is reasonably high, although not as strong as the increase in the total normal stress. This is the bouldery front of the flow, in which the small values of the fluid pressure may be due to an unsaturated flow configuration. However, from video observations of various events we know, that it is only the very first part of the flow ($<1\text{min}$), that is not completely saturated.
- In the next region, the fluid pressure still increases, but less strong. This part corresponds to the transitional zone in the flow. Here, the increase in pore pressure is due to the fact, that the flow transforms into a completely mixed uniform suspension state.
- In the last and main part of the flow, the measured fluid pressure coincides with the normal stress, indicating that the bulk flow is within a state of uniform suspension. This the tail of the flow.

The evaluated effective friction coefficient μ_{eff} varies with the state of vertical mixing. It constantly decreases in the head and the transitional zone down to a constant level in the suspended tail of the flow. Except for the unsaturated first couple of seconds, the flow

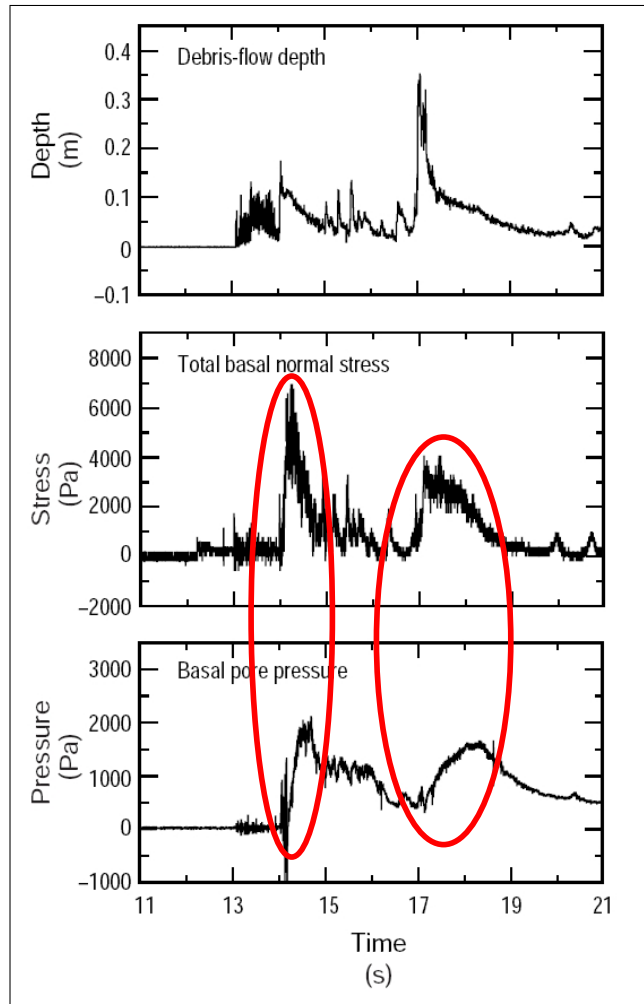


Figure 2.6: Results from the U.S. Geological Survey Debris flow Flume (taken from [49]) - Height, normal stress and basal fluid pressure measurements are plotted versus time

exhibits a more or less constant bulk density $\rho \approx 1800 \frac{\text{kg}}{\text{m}^3}$. This suggests, that the basal friction is a function of the vertical mass distribution.

2.3.2 USGS - Flume results

Figure 2.6 shows the results of an experiment in the USGS Debris flow Flume [49]. Again, height, total normal stress and effective fluid pressure are plotted. However, this time no shear stress results are available. In the plots, the passage of two distinct surges is seen. For both flume surges we make the same observation, than for the real scale Illgraben event. The increase of height and normal forces is abrupt, whereas the increase of the fluid pressure behind the front is much slower. This again suggests different vertical mixture states in head and tail of a particular surge.

Model	One-phase, Voellmy/Salm	Iverson/ Denlinger	Pitman/Le, Pelanti
Basic equations	one-component balance laws for mass and momentum	multi-components balance laws for mass and momentum (conservative form)	multi-component balance laws for mass and momentum (non-conservative form)
General appearance	depth-averaged bulk formulation	depth-averaged bulk formulation	depth-averaged single-component formulation
Horizontal structure	homogeneous in all directions	homogeneous, due to constant volume fractions	varies with integrated volume fractions
Vertical structure	homogeneous in all directions	homogeneous, due to constant volume fractions	homogeneous, due to constant volume fractions
Closure solid phase	Mohr-Coulomb relation with turbulent friction	Mohr-Coulomb relation	Mohr-Coulomb relation
Closure fluid phase	-	Newtonian fluid	ideal fluid
Basal Fluid pressure	does not appear	extra advection-diffusion equation	not explicitly taken into account

Table 2.5: Summary of the underlying assumptions of existing mathematical models for the dynamics of debris flows.

2.4 Measurements versus existing theories

Both, the USGS-flume data set, and the Illgraben measurements show, that the increase of height and normal stress at the front of a granular debris flow is instantaneous, whereas the basal fluid pressure increases slower and with a small delay. As illuminated in Section 1.3 this indicates, that different states of vertical mixing govern the head and tail of the flow. From the additional shear stress measurements at Illgraben we also know, that the basal friction varies with the vertical distribution of components. These results suggest, that in order to apply a realistic friction law at the base of the flow, a mathematical model must contain information on the composition and the vertical structure of the flowing body at a specific location. In the following, we briefly comment on the existing models with respect to the previously listed requirements. The model assumptions are summarized in Table 2.5.

2.4.1 One-phase, rheological models

By assuming the flow to consist of a single homogeneous material, redistribution of components is not possible. However, these approaches work perfectly fine for particle-fluid

flows, in which the effects of internal redistribution play a negligible role. This is for instance true for mud flows. Relevant publications on constitutive equations for them are due to Costa [21] and Coussot [22]. Also in the class of one-phase models belong those approaches, that assume a debris flows to be dry as first approximation. Then, the fluid phase is neglected and the complete dynamics of the flow is described by the solids (compare [40]). Within these models internal redistribution cannot be modeled, due to the absence of the fluid.

2.4.2 The Iverson/Denlinger model

Iverson starts from the single component balance laws for mass and momentum. In a next step, he formulates balance laws for the mixture and assumes, that the volume fractions of the single components are constant. Moreover, in vertical direction, along which the actual depth-integration is performed, the distribution of the components is assumed to be homogeneous. Hence, the possibility of horizontal and vertical re-distribution is not taken into account. The presence of two distinct species (fluid, solid) is considered insofar, as the bulk stress is composed by single stresses multiplied by their constant volume fraction. Consequently, the bulk stress and the bulk basal friction do always exhibit the same constant composition. With this approach, especially levee and deposition processes cannot be modeled in a satisfactory way.

Iverson overcame this problem, by imposing another equation on the system, an evolution diffusion equation for the basal fluid pressure. As we saw in Section 1.3, the basal fluid pressure influences changes with the state of vertical mixing. With this extra equation, Iverson implicitly re-introduces a vertically varying mass distribution into the system. Formally, a varying fluid pressure contradicts the initial assumption of a homogeneous, vertical distribution within the flowing body. Yet, the results achieved with that model are significant. This indicates, that a vertically varying structure of the flow is essential to attain a model that captures the basic features of a debris flow.

2.4.3 Existing depth-integrated multi-component approaches

Here, we focus on the model proposed by Pitman and Le [68], which was later generalized by Pelanti [67] to account for bulk mixture conservation. In both cases, the single-component balance laws for mass and momentum are integrated directly, and thus, the models allow for varying volume fraction in the horizontal, flowing direction. However, during the process of depth-integration, also a vertically homogeneous distribution of components is assumed. Hence, the development of a granular front with higher amount of solids in the head, than in the tail is possible, whereas the system cannot describe a change in the vertical structure.

2.4.4 Necessity of a model extension

Neither of the existing depth-averaged mathematical debris flow models allows for horizontally, as well a vertically varying internal structure within the flowing body. However, from analyzing existing data sets, we saw, that the varying internal structure seems to have a crucial influence on the dynamics of granular debris flows. We will therefore propose and analyze two different ways of deriving multi-component shallow flow equations, that explicitly account for a change in horizontal and vertical composition, and hence allow for a re-distribution of fluid and solid components.

Chapter 3

Derivation of a one-phase shallow flow model

A well-known and rigorously derived 1D-model to describe the dynamics of shallow granular flow is due to Savage and Hutter [77, 78]. Generalizations include the formulation as a 2D system and the flow over complex topography [33, 93], as well as the additional consideration of mass entrainment and deposition [32]. In the following the important steps of the derivation are presented. At first, balance laws for mass and momentum and boundary conditions for the interfaces are formulated. In a next step these equations are integrated over depth and closure relations are applied. The final result is a nonlinear, hyperbolic system of conservation laws, related to the shallow water equations.

In this chapter, and also later in the thesis, we will focus on the depth-averaging process. That is why, an explicit formulation of the equation in two space dimensions is omitted, and instead we refer to the comprehensive book of Hutter and Pudasaini [70]. However, it should be noted, that for plane stress states, all following one-dimensional models can be extended in a straight-forward manner to two space dimensions.

3.1 Framework and balance laws

3.1.1 Coordinate system

The surface profile $b : \mathbb{R} \rightarrow \mathbb{R}$ is given in an inclined coordinate system with a slope angle ζ . Both are plotted in Figure 3.1. The slope angle can be interpreted as the average inclination of the basal topography $b(x)$.

The free surface s of the flow is given as a function $s : \mathbb{R} \times \mathbb{R}^+ \rightarrow \mathbb{R}$. In contrast to the topography it varies in time and is a function of both x and t . For the sake of simplicity both b and s are assumed to be sufficiently smooth during the derivation.

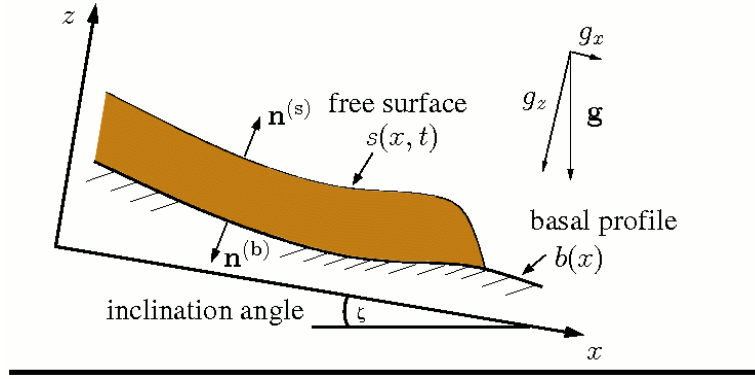


Figure 3.1: Coordinate system, basal profile and free surface of the flow

3.1.2 Basic set of equations

It is commonly accepted (compare [77, 78, 32]) to treat the granular material as a continuum with the corresponding field variables

$$\begin{aligned} \rho & : \text{density} \\ \mathbf{u} = \begin{pmatrix} u \\ w \end{pmatrix} & : \text{velocity} \\ \sigma = \begin{pmatrix} \sigma_{xx} & \sigma_{xz} \\ \sigma_{zx} & \sigma_{zz} \end{pmatrix} & : \text{Cauchy stress tensor} \end{aligned}$$

The field variables ρ , \mathbf{u} and σ are defined at every point within the flowing body, namely for the set $\{(x, z, t) : b(x) \leq z \leq s(x, t)\}$. According to convention in soil and rock mechanics, the Cauchy stress is positive in compression. It also includes pressure. Furthermore the material is assumed to be incompressible, such that ρ is constant. From first principles and along the lines of standard continuum mechanics for fluids one can deduce balance laws for mass and momentum (e.g. [7, 41]):

$$\begin{aligned} \nabla \cdot \mathbf{u} &= 0 \\ \partial_t (\rho \mathbf{u}) + \nabla \cdot (\rho \mathbf{u} \mathbf{u}) &= \nabla \cdot \sigma + \rho \mathbf{g} \end{aligned} \tag{3.1}$$

Here, $\mathbf{g} = \begin{pmatrix} g_x \\ g_z \end{pmatrix}$ stands for the vector of gravitational acceleration. Due to the inclination of the coordinate system both components of \mathbf{g} are non-zero.

3.2 Boundary conditions

Kinematic and dynamic boundary conditions are formulated at the interfaces $s(x, t)$ and $b(x)$. The kinematic conditions are geometrical statements, and implicitly describe the evolution of the interfaces with time. Later, this will be used to define the height of the

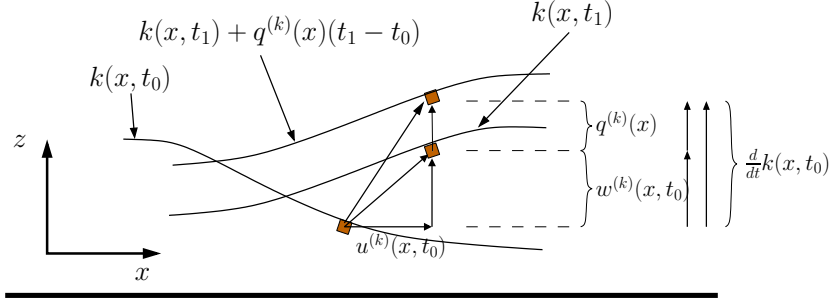


Figure 3.2: Motion of a material point on the interface k with a time-independent mass production rate

flow. Boundary conditions of dynamic type specify the applied stress at the interfaces and incorporate assumptions on the Cauchy stress tensor σ .

Within this section the unit normals $\mathbf{n}^{(s)}$ and $\mathbf{n}^{(b)}$ are frequently used. Due to the varying interfaces their orientation is local. By making use of the implicit function theorem one derives the following expression

$$\mathbf{n}^{(s)} = \frac{1}{\sqrt{1 + (\partial_x s)^2}} \begin{pmatrix} -\partial_x s \\ 1 \end{pmatrix} \quad \mathbf{n}^{(b)} = \frac{1}{\sqrt{1 + (\partial_x b)^2}} \begin{pmatrix} \partial_x b \\ -1 \end{pmatrix}$$

Both $\mathbf{n}^{(b)}$ and $\mathbf{n}^{(s)}$ are chosen as outside normals (compare Figure 3.1).

3.2.1 Kinematic conditions

Kinematic conditions reflect that the interfaces are material boundaries. In the case of zero mass production, this means that infinitesimal material points, which are initially on the boundary, will remain there for all times. Their positions can be tracked by changing to a Lagrangian framework and interpreting x and z as functions of t . The following considerations are formulated for a general interface $k(x, t)$, which can either stand for the free surface $s(x, t)$ or the basal profile $b(x, t)$. The vertical velocity $w^{(k)}(x(t), t)$ of a material point on k , is given by the total time derivative of the interface $\frac{d}{dt}k(x(t), t)$. Hence,

$$\frac{d}{dt}k(x(t), t) = \frac{\partial}{\partial t}k(x(t), t) + \frac{\partial}{\partial t}x(t) \frac{\partial}{\partial x}k(x(t), t) = w^{(k)}(x(t), t) \quad (3.2)$$

An important characteristic of geophysical mass flows is the deposition and entrainment of material during the flow. These are modeled as positive and negative mass production rates at the interface and indicated by $q^{(k)}(x(t), t)$. The vertical velocity of any material point is then given by $w^{(k)}(x(t), t) + q^{(k)}(x(t), t)$ (compare Figure 3.2). Furthermore $\partial_t x(t)$ is given by the velocity field evaluated at the interface, indicated $u^{(k)}(x(t), t)$. For the

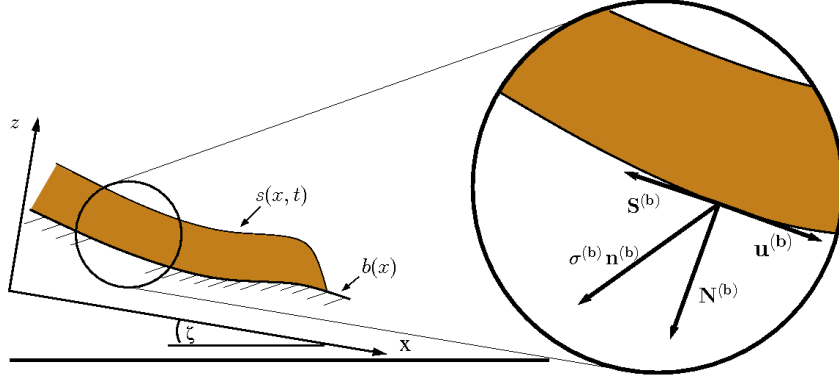


Figure 3.3: Normal, shear and effective stress at the bottom surface

basal profile b and the free surface s , we have

$$\begin{aligned}\partial_t s + u^{(s)} \partial_x s &= w^{(s)} + q^{(s)} \\ \partial_t b + u^{(b)} \partial_x b &= w^{(b)} + q^{(b)}\end{aligned}\quad (3.3)$$

Here, for the reason of being symmetric, the time derivative of b is written down explicitly. In fact b doesn't have any time dependency, thus for a fixed bottom topography $\partial_t b \equiv 0$.

3.2.2 Dynamic conditions

Normal components of the stresses at the surface and the bottom profile are prescribed as dynamic boundary conditions. Like above, superscripts on field variables stand for their evaluation at the interface.

At the free surface there is no stress at all, one speaks of a traction-free condition

$$\sigma^{(s)} \mathbf{n}^{(s)} = \mathbf{0} \quad \Rightarrow \quad \begin{aligned}\sigma_{xz}^{(s)} - \sigma_{xx}^{(s)} \partial_x s &= 0 \\ \sigma_{zz}^{(s)} - \sigma_{xz}^{(s)} \partial_x s &= 0\end{aligned}\quad (3.4)$$

The magnitude of the frictional shear force $\mathbf{S}^{(b)}$ evaluated at the bottom is assumed to be proportional to the magnitude of the normal stress $\mathbf{N}^{(b)}$, the factor of proportionality being the friction coefficient μ . This relation is known as Coulomb dry friction assumption and reads as

$$\|\mathbf{S}^{(b)}\| = \mu \|\mathbf{N}^{(b)}\| \quad (3.5)$$

The direction of $\mathbf{S}^{(b)}$ opposes the tangential flow velocity at the base $\mathbf{u}^{(b)}$. As indicated in Figure 3.3, in general b varies with x and the orientation of the bottom surface is local. Then the effective stress vector at the basis $\sigma^{(b)} \mathbf{n}^{(b)}$ is decomposed into its normal component $\mathbf{N}^{(b)} = \mathbf{n}^{(b)} \left(\mathbf{n}^{(b)T} \sigma^{(b)} \mathbf{n}^{(b)} \right)$ and its shear component $\mathbf{S}^{(b)} = \sigma^{(b)} \mathbf{n}^{(b)} - \mathbf{N}^{(b)}$

and the Coulomb relation is

$$\mathbf{S}^{(b)} = \sigma^{(b)} \mathbf{n}^{(b)} - \mathbf{N}^{(b)} = -\mu \left(\frac{\mathbf{u}^{(b)}}{\|\mathbf{u}^{(b)}\|} \right) \|\mathbf{N}^{(b)}\| \quad (3.6)$$

Equation (3.6) can easily be solved for $\sigma^{(b)} \mathbf{n}^{(b)}$ and one gets

$$\begin{aligned} \sigma_{xx}^{(b)} \partial_x b - \sigma_{xz}^{(b)} &= -\left(\mu \frac{u^{(b)}}{\|\mathbf{u}^{(b)}\|} + \partial_x b \right) \|\mathbf{N}^{(b)}\| \\ \sigma_{xz}^{(b)} \partial_x b - \sigma_{zz}^{(b)} &= -\left(\mu \frac{w^{(b)}}{\|\mathbf{u}^{(b)}\|} - 1 \right) \|\mathbf{N}^{(b)}\| \end{aligned} \quad (3.7)$$

3.3 Dimensionless coordinates

3.3.1 Definition of the scales

Following [77, 70], two length-scales can be defined in the governing differential equations (3.1), namely the characteristic flow height H and the characteristic flow length L . The flow is gravity induced, hence the potential for free fall drives the process and a reasonable choice for the characteristic time scale is the free fall time scale in x direction $\sqrt{\frac{L}{g}}$. Then velocity scales in x and z direction are given by \sqrt{gL} and $\frac{H}{L} \sqrt{gL}$ respectively. Typical stresses are of the order of the weight of the material $\rho g H$. The scaling for the shear stress directly incorporates the friction coefficient μ .

According to the previous considerations, the following dimensionless coordinates are introduced

$$\begin{aligned} x &= L \tilde{x} & z &= H \tilde{z} & t &= \sqrt{\frac{L}{g}} \tilde{t} \\ u &= \sqrt{gL} \tilde{u} & w &= \frac{H}{L} \sqrt{gL} \tilde{w} \\ \sigma_{xx} &= \rho g H \tilde{\sigma}_{xx} & \sigma_{xz} &= \mu \rho g H \tilde{\sigma}_{xz} & \sigma_{zz} &= \rho g H \tilde{\sigma}_{zz}. \end{aligned}$$

3.3.2 Scaled model formulation

By defining the shallowness parameter $\varepsilon := \frac{H}{L}$, the balance equations (3.1) transform into

$$\partial_{\tilde{x}} \tilde{u} + \partial_{\tilde{z}} \tilde{w} = 0 \quad (3.8)$$

$$\partial_{\tilde{t}} \tilde{u} + \partial_{\tilde{x}} (\tilde{u}^2) + \partial_{\tilde{z}} (\tilde{u} \tilde{w}) = \varepsilon \partial_{\tilde{x}} \tilde{\sigma}_{xx} + \mu \partial_{\tilde{z}} \tilde{\sigma}_{xz} + \sin \zeta \quad (3.9)$$

$$\varepsilon (\partial_{\tilde{t}} \tilde{w} + \partial_{\tilde{x}} (\tilde{u} \tilde{w}) + \partial_{\tilde{z}} (\tilde{w}^2)) = \varepsilon \mu \partial_{\tilde{x}} \tilde{\sigma}_{xz} + \partial_{\tilde{z}} \tilde{\sigma}_{zz} + \cos \zeta \quad (3.10)$$

3.3.3 Scaled boundary conditions

The rescaled kinematic boundary condition (3.3) is given by

$$\begin{aligned}\partial_{\tilde{t}} \tilde{s} + \tilde{u}^{(s)} \partial_{\tilde{x}} \tilde{s} &= \tilde{w}^{(s)} + \frac{1}{\sqrt{\varepsilon g H}} q^{(s)} \\ \partial_{\tilde{t}} \tilde{b} + \tilde{u}^{(b)} \partial_{\tilde{x}} \tilde{b} &= \tilde{w}^{(b)} + \frac{1}{\sqrt{\varepsilon g H}} q^{(b)}\end{aligned}\tag{3.11}$$

This motivates the definition of $\tilde{q}^{(s)} = (\varepsilon g H)^{-\frac{1}{2}} q^{(s)}$ and $\tilde{q}^{(b)} = (\varepsilon g H)^{-\frac{1}{2}} q^{(b)}$. Next, the dynamic boundary conditions are written in dimensionless coordinates. From (3.4), we obtain

$$\begin{aligned}\mu \tilde{\sigma}_{xz}^{(s)} - \varepsilon \tilde{\sigma}_{xx}^{(s)} \partial_{\tilde{x}} \tilde{s} &= 0 \\ \tilde{\sigma}_{zz}^{(s)} - \varepsilon \mu \tilde{\sigma}_{xz}^{(s)} \partial_{\tilde{x}} \tilde{s} &= 0\end{aligned}\tag{3.12}$$

Finally, (3.7) yields

$$\begin{aligned}\varepsilon \tilde{\sigma}_{xx}^{(b)} \partial_{\tilde{x}} \tilde{b} - \mu \tilde{\sigma}_{xz}^{(b)} &= -\left(\mu \frac{\tilde{u}^{(b)}}{\|\tilde{\mathbf{u}}^{(b)}\|} + \varepsilon \partial_{\tilde{x}} \tilde{b}\right) \|\tilde{\mathbf{N}}^{(b)}\| \\ \varepsilon \mu \tilde{\sigma}_{xz}^{(b)} \partial_{\tilde{x}} \tilde{b} - \tilde{\sigma}_{zz}^{(b)} &= -\left(\varepsilon \mu \frac{\tilde{w}^{(b)}}{\|\tilde{\mathbf{u}}^{(b)}\|} - 1\right) \|\tilde{\mathbf{N}}^{(b)}\|\end{aligned}\tag{3.13}$$

Tildes are dropped in the following and all calculations will be done in the transformed variables.

3.4 Integration over the flow depth

3.4.1 Flow height and shallow flow assumption

A fundamental assumption for all following considerations is, that the flow exhibits a small aspect ratio, namely $\varepsilon \ll 1$. The flow is integrated over its depth to reduce the spatial resolution and increase the computational efficiency. Afterwards, small terms can be identified and neglected.

The integration is performed along the z -axis. With $s(x, t)$ and $b(x)$, the height of the flow is given by

$$h(x, t) := s(x, t) - b(x)$$

3.4.2 Preliminary considerations

Relations (3.14) - (3.16) are derived from the boundary conditions. They are essential for the following integrations ($[\cdot]$ denotes the Gauss bracket).

$$\partial_t h + [u^{(z)} \partial_x z - w^{(z)}]_b^s = [q^{(z)}]_b^s \quad (3.14)$$

$$[u^{(z)} (\partial_t z + u^{(z)} \partial_x z - w^{(z)})]_b^s = [u^{(z)} q^{(z)}]_b^s \quad (3.15)$$

$$[\varepsilon \sigma_{xx}^{(z)} \partial_x z - \mu \sigma_{xz}^{(z)}]_b^s = \left(\mu \frac{u^{(b)}}{\|\mathbf{u}^{(b)}\|} + \varepsilon \partial_x b \right) \|\mathbf{N}^{(b)}\| \quad (3.16)$$

The first is derived by subtracting top and bottom kinematic condition (3.11) from each other and it provides an equation for the change of height in time. The second relation is also based on the kinematic condition, this time each equation in (3.11) is multiplied by the interface velocity prior to the subtraction. Finally, the third relation is the difference of the x -component dynamic conditions at the surface (3.12) and the basal topography (3.13).

In order to simplify further formulas, we introduce the following notation

$$\langle \cdot \rangle := \frac{1}{h} \int_b^s \cdot dz. \quad (3.17)$$

Hence $\langle f \rangle$ denotes the depth-averaged quantity of the function f and has no explicit dependency on z any more.

3.4.3 Depth-averaged mass conservation

Now, the mass conservation (3.8) is integrated along the z -axis. Care has to be taken, since the integral boundaries are functions of x and t , thus using the Leibniz-formula for parameter dependent integrals yields

$$\begin{aligned} \int_b^s (\partial_x u + \partial_z w) dz &= \int_b^s \partial_x u dz + \int_b^s \partial_z w dz \\ &= \partial_x (h \langle u \rangle) - [u^{(z)} \partial_x z - w^{(z)}]_b^s \end{aligned} \quad (3.18)$$

The bracketed term is now substituted by making use of (3.14) and the resulting depth-averaged mass conservation reads as

$$\partial_t h + \partial_x (h \langle u \rangle) = [q^{(z)}]_b^s \quad (3.19)$$

3.4.4 Depth-averaged momentum balance

The x -momentum balance (3.9) is treated in a similar manner. By making use of (3.15) the convective flux transforms into

$$\begin{aligned} & \int_b^s (\partial_t u + \partial_x (u^2) + \partial_x (uw)) dz \\ &= \partial_t (h \langle u \rangle) + \partial_x (h \langle u^2 \rangle) - [u^{(z)} q^{(z)}]_b^s. \end{aligned} \quad (3.20)$$

The dynamic condition (3.16) is incorporated in the depth-integrated right-hand side

$$\begin{aligned} & \int_b^s (\varepsilon \partial_x \sigma_{xx} + \mu \partial_z \sigma_{xz} + \sin \zeta) dz \\ &= \partial_x (\varepsilon h \langle \sigma_{xx} \rangle) - \left(\mu \frac{u^{(b)}}{\|\mathbf{u}^{(b)}\|} + \varepsilon \partial_x b \right) \|\mathbf{N}^{(b)}\| + h \sin \zeta \end{aligned} \quad (3.21)$$

Finally, the complete depth-averaged momentum balance can be found:

$$\begin{aligned} & \partial_t h + \partial_x (h \langle u^2 \rangle + \varepsilon h \langle \sigma_{xx} \rangle) = \\ & - \left(\mu \frac{u^{(b)}}{\|\mathbf{u}^{(b)}\|} + \varepsilon \partial_x b \right) \|\mathbf{N}^{(b)}\| + h \sin \zeta + [u^{(z)} q^{(z)}]_b^s \end{aligned} \quad (3.22)$$

With (3.19) and (3.22) there is a system of two partial differential equations given in the four unknowns $h, \langle u \rangle, \langle u^2 \rangle, \langle \sigma_{xx} \rangle$. Two unknowns can be eliminated, by formulating closure relations in terms h and $\langle u \rangle$. In particular that means, $\langle u^2 \rangle$ is closed by introducing a momentum shape factor and $\langle \sigma_{xx} \rangle$ by making use of the vertical momentum balance and a constitutive relation for the stress.

3.5 Remark on the shape factor

The relevant velocity field in the depth-averaged system is given by $\langle u \rangle$. By introducing the momentum shape factor $C_u := \frac{\langle u^2 \rangle}{\langle u \rangle^2}$, we can formally write

$$\langle u^2 \rangle = C_u \langle u \rangle^2$$

The value of C_u can be computed for explicit velocity profiles. These are results of a steady-state, or constant-acceleration flow analysis assuming a rheology based on experimental data. Sometimes C_u is then called a momentum flux parameter instead of shape factor, like in the rigorous studies on basic multi-component models and their averaging by Song and Ishii [79, 81].

The following velocity profiles and corresponding shape factors are motivated by experiments. Many of them have been conducted in the past decades in the field of granular and

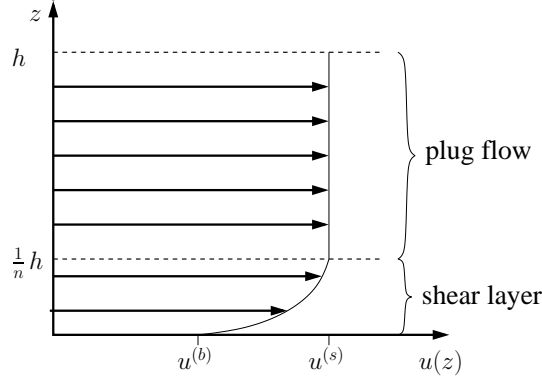


Figure 3.4: Typical velocity profile with a thin shear layer under a plug flow regime above

geophysical flow research [54], as well as visco-plastic shallow flow research [61]. In most cases the velocity profile is characterized by a relatively thin layer of intense shear with a non-zero slip velocity at the base and an overburden plug flow regime (compare Figure 3.4). The influence of shear layer thickness and shear layer curvature is demonstrated by considering two simple examples.

3.5.1 Shear layer thickness

The velocity profile is parametrized as a function of the shear layer thickness $\frac{1}{n}h$, $n \in \mathbb{N}$

$$u_n(z) = \begin{cases} u^{(s)} & \frac{1}{n}h \leq z \leq h \\ u^{(s)} + (u^{(b)} - u^{(s)})\left(1 - \frac{zn}{h}\right)^{\frac{3}{2}} & 0 \leq z \leq \frac{1}{n}h \end{cases} \quad (3.23)$$

Then the shape factor $C_{u,n}$ is computed to be

$$C_{u,n} = \frac{\langle u_n^2 \rangle}{\langle u_n \rangle^2} = \frac{u^{(s)} + \frac{4}{5n} u^{(s)}(u^{(b)} - u^{(s)}) + \frac{1}{4n} (u^{(b)} - u^{(s)})^2}{u^{(s)} + \frac{4}{5n} u^{(s)}(u^{(b)} - u^{(s)}) + \frac{4}{25n^2} (u^{(b)} - u^{(s)})^2} \quad (3.24)$$

and it is easily seen, that in the limit of plug flow, we obtain $\lim_{n \rightarrow \infty} C_{u,n} = 1$. However, when the shear layer is thicker C_u differs from 1. With $n = 1$ and $u^{(b)} = \frac{1}{2}$ (3.24) reduces to

$$C_{u,1} = \frac{1 - \left(\frac{37}{80}\right) u^{(s)}}{1 - \left(\frac{11}{25}\right) u^{(s)}} \quad (3.25)$$

thus one gets $C_u = 1.04$ for $u^{(s)} = 1$.

3.5.2 Shear layer curvature

To analyze the influence of the shear layer curvature, the profile is parametrized as a function of p in the following way

$$u_p(z) = u^{(s)} \left(\frac{z}{h}\right)^p \quad 0 \leq p \leq 1 \quad (3.26)$$

Then the shape factor is computed to be

$$C_{u,p} = \frac{(p+1)^2}{2p+1} \quad (3.27)$$

Hence, C_u is independent of the surface velocity and ranges between 1 in the plug flow limit and $\frac{4}{3}$ for a linear velocity profile. The shape factor is set to one, when the shallow flow theory is applied to actual geophysical flows, however, it is important to keep in mind the limits of such an assumption.

3.6 Constitutive Relation for the stress

3.6.1 Vertical momentum balance

We integrate the vertical momentum component (3.10) up to height z and derive an expression for σ_{zz}

$$\sigma_{zz}(x, z, t) = \cos \zeta (h(x, t) - z) + O(\varepsilon) \quad (3.28)$$

Additional use has been made of the (rescaled) static, normal stress at the ground $\sigma_{zz}^{(b)} = \cos \zeta h(x, t)$. Moreover, in the limit of a small aspect ratio ε , the normal stress component on planes parallel to the basal profile varies linearly with height and the vertical momentum balance reduces to a hydrostatic assumption. In the absence of vertical velocities and shear stresses, this relation is also valid for big ε . In a next step, σ_{xx} is expressed as a function of σ_{zz} .

3.6.2 Isotropic fluid

The simplest possible approach is to assume, that the material governs the properties of an isotropic fluid. Then, the stress tensor is uniform and a relation is given by

$$\sigma_{xx} = \sigma_{zz} \quad (3.29)$$

The integral (3.28) can then be evaluated

$$h \langle \sigma_{xx} \rangle = h \langle \sigma_{zz} \rangle = \frac{h^2}{2} \cos \zeta + O(\varepsilon). \quad (3.30)$$

3.6.3 Mohr-Coulomb material

Often the flow material is modelled as an ideal, cohesionless Coulomb material with an internal angle of friction Φ . For details, see [77, 70, 65, 42]. In this case, the whole flowing body is assumed to be in plastic yield, implying that shear and normal forces are related according to $\|\mathbf{S}^{(z)}\| = \tan \Phi \|\mathbf{N}^{(z)}\|$ for a shear plane at an arbitrary height z . Furthermore the shear stress at the bottom profile is determined by the Coulomb friction relation

$\|\mathbf{S}^{(b)}\| = \mu \|\mathbf{N}^{(b)}\|$. Admissible stress states exhibit an invariant, which is reflected by the fact, that they lie on a circle in a normal-/shear stress diagram. However, the previous restrictions do not specify the Mohr-circle uniquely, but allow for two solutions, such that

$$\begin{aligned} \sigma_{xx} &= K \sigma_{zz} \\ \text{with } K &= \frac{2}{\cos^2 \Phi} \left(1 \mp \sqrt{1 - \frac{\cos^2 \Phi}{\cos^2 \delta}} \right) - 1 \end{aligned} \quad (3.31)$$

Here $\delta := \arctan \mu$ and K has real values for all $\delta < \Phi$. The two solutions are referred to as the active and the passive earth pressure coefficient K_a and K_p respectively. They are associated with particular deformations within the flow. During acceleration the flow is dilated, which is considered as an active stress state. The passive earth pressure is appropriate when the velocity decreases and the flowing body is compressed. Therefore,

$$K = \begin{cases} K_a & : \quad \partial_x u \geq 0 \\ K_p & : \quad \partial_x u < 0 \end{cases}$$

Although there is experimental evidence, that a deformation dependent earth pressure coefficient is necessary to produce at least qualitatively right run-out distances [33] a sharp discontinuity in K could not be verified in laboratory. With the latter result $\langle \sigma_{xx} \rangle$ is evaluated to be

$$h \langle \sigma_{xx} \rangle = h \langle K \sigma_{zz} \rangle = K \frac{h^2}{2} \cos \zeta + O(\varepsilon) \quad (3.32)$$

With an earth pressure $K \equiv 1$ the isotropic fluid condition is recovered.

3.7 The Savage-Hutter model

3.7.1 Final formulation

In the final formulation of the model the abbreviation $U := \langle u \rangle$ is introduced. Terms in $O(\varepsilon^\gamma)$, $\gamma > 1$ are neglected, whereas order ε terms are kept in the system. To simplify the interfacial mass production a Boussinesq like approximation is introduced and one assumes $u^{(b)} = U + O(\varepsilon^\gamma)$ and $u^{(s)} = U + O(\varepsilon^\gamma)$. In the context of geophysical flows, positive mass production terms are referred to as entrainment, whereas negative mass production terms are referred to deposition. Then the resulting **Savage-Hutter model (SHM)** for the dynamics of shallow granular flow is given by the following system of conservation laws

$$\begin{aligned} \partial_t \begin{pmatrix} h \\ hU \end{pmatrix} + \partial_x \begin{pmatrix} hU \\ C_u hU^2 + \varepsilon K \cos \zeta \frac{h^2}{2} \end{pmatrix} &= \begin{pmatrix} [q^{(k)}]_b^s \\ S \end{pmatrix} \\ S := \underbrace{h \sin \zeta}_{\text{acceleration}} - \underbrace{\mu \frac{U}{\|U\|} h \cos \zeta}_{\text{dry Coulomb friction}} - \underbrace{\varepsilon \partial_x b h \cos \zeta}_{\text{variation in the topography}} + \underbrace{U [q^{(k)}]_b^s}_{\text{entrainment and deposition}} \end{aligned} \quad (3.33)$$

A very important generalization of this theory has been the extension to flow over complex topographies. Then the 1d reference coordinate system is extended to a 2d curvilinear reference surface [33].

3.7.2 Eigenvalues

The derived system (3.33) is similar to the well-known shallow water system. For a detailed discussion on the mathematical properties, we refer to [58]. However, the additional parameters K , ε and C_u do influence the eigenspeeds of the system. That has a direct consequence to practical applications, since it also affects the critical Froude number. To analyze the eigenspeeds, one has to consider the hyperbolic structure of the homogeneous system.

$$\partial_t \begin{pmatrix} h \\ hU \end{pmatrix} + \partial_x \begin{pmatrix} hU \\ C_u hU^2 + \beta \frac{h^2}{2} \end{pmatrix} = \begin{pmatrix} 0 \\ 0 \end{pmatrix}$$

with $\beta := \varepsilon K \cos \zeta$. In the full system K is a function of $\text{sgn } \partial_x U$, but for the time being, it is assumed to be constant. Thus considerations break down, when big changes in the topography are present, in all other cases they are reasonable. The parameter dependent eigenspeeds for the system are then given by

$$\lambda_{1,2} = C_u U \pm \sqrt{C_u(C_u - 1)U^2 + \beta h} \quad (3.34)$$

In shallow water flow a Froude number $\text{Fr} := \frac{U}{\cos \zeta h}$ smaller or bigger than the critical value $\text{Fr}_{\text{sh}} = 1$ indicates whether the flow is in a sub- or in a super-critical flow regime. From the derived eigenspeeds for the **SHM**, one can immediately deduce the critical value for shallow granular flow to be

$$\text{Fr}^{(crit)} \Big|_{\text{SHM}} = \sqrt{\frac{K}{C_u}} \quad (3.35)$$

Thus, for a shape factor $C_u = 1$ and isotropic conditions $K = 1$, the critical value is once again 1, but in general $\text{Fr}^{(crit)} \Big|_{\text{SHM}} \neq 1$.

3.8 Voellmy-Salm variation and practical use

Depth-averaged approximations of geophysical flows have existed for quite some time, and the Savage-Hutter theory provides a rigorous mathematical framework for the derivation of those. However, in practical use, modifications to the theory are necessary, based on open channel flow hydraulics. This is due to the fact, that the Mohr-Coulomb stress state, incorporated into the **SHM**, is of quasi-static type. Consequently the basal friction involves no rate-dependency. Most of the modifications propose a different basal friction relation. We therefore formulate the model in terms of a generalized basal friction relation

$F(h, U)$ as a function of flow height and flow velocity.

$$\partial_t \begin{pmatrix} h \\ hU \end{pmatrix} + \partial_x \begin{pmatrix} hU \\ hU^2 + \varepsilon K \cos \zeta \frac{h^2}{2} \end{pmatrix} = \begin{pmatrix} 0 \\ S \end{pmatrix}$$

$$S := h \sin \zeta - F(h, U) - \varepsilon \partial_x b h \cos \zeta$$

The **Voellmy-Salm model (VSM)** [6] is one of those modified system, although it should be noted, that it has existed even longer than the Savage-Hutter theory itself. It has been successfully applied to avalanche simulations since the mid 1960s. In contrast to the **SHM**, it incorporates an additional rate dependent friction term, similar to Chezy friction in hydraulic engineering. The **VSM** basal friction relation is given by

$$F(h, U) := \mu \frac{U}{\|U\|} h \cos \zeta + \xi U^2$$

The parameters μ and ξ have been calibrated with cadastre data of 60 years of avalanche observation and reasonable results can be achieved in predicting avalanche run-out [34, 19].

Chapter 4

A depth-integrated multi-component system for debris flows

The dynamics of shallow multi-component mixtures has always been a prominent topic in science, as they are highly relevant for many geophysical flow phenomena. Some 30 years ago Armi analyzed the hydraulics of two flowing layers of different densities in detail [3, 4] and later this model served as a basis to develop numerical solvers [1, 12] and perform extensive numerical simulations for two-layer shallow water flow [17]. Only recently Iverson [44], later Iverson and Denlinger [47, 27] proposed a shallow flow model for a highly concentrated and vertically well-mixed particle-fluid mixture. Their intention was to apply both soil mechanics and hydraulic concepts to model the quasi-static solid limit and fully developed flow limit. However, to overcome many of the subtleties in the derivation, they assumed the constituent's volume fractions and hence the bulk mixture density to be constant. As a consequence the multi-phase character of the system reduces to a stress tensor with contributions from both components (solid/fluid). Pitman and Le generalized this idea and allowed for horizontally varying volume fractions [68, 67]. The model derived within this work is the result of yet another generalization. The aim is to recover information on the vertical structure of the flow, while at the same time still make use of the simplifying framework of depth-integration. In the case of constant volume fractions and a well-mixed vertical structure the final model reduces to an extended version of the Iverson model, whereas it reduces to the two-layer shallow water equations in the limit of perfect vertical layering.

This chapter deals with the derivation of the model. Section 4.1 to 4.5 describe general concepts necessary for the extension of Savage-Hutter's shallow flow theory to multi-component systems. As previously mentioned the vertical distribution of the different species is of special interest, as it significantly affects the effective stresses in the mixture and the friction at the basis. In section 4.6 and 4.7 possible solutions for two special vertical distributions are suggested, namely for an uniform suspension of particles in a fluid and for a complete layering of two distinct components. In section 4.8 both approaches are combined to a unified shallow debris flow theory.

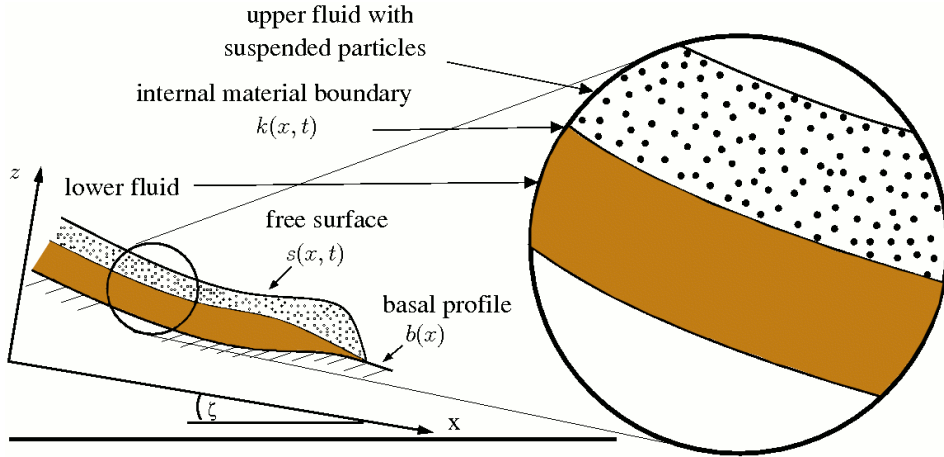


Figure 4.1: Two completely stratified fluids - the upper one contains suspended particles

4.1 Multi-component balance laws

4.1.1 General framework

The coordinate system is given as in Chapter 3 on one-phase flow. Basal topography b , free surface s and possible internal material boundaries k are assumed to be maps in x and t . Then according to 3.2, the unit normals are given by

$$\begin{aligned} \mathbf{n}^{(s)} &= \frac{1}{\sqrt{1 + (\partial_x s)^2}} \begin{pmatrix} -\partial_x s \\ 1 \end{pmatrix} & \mathbf{n}^{(b)} &= \frac{1}{\sqrt{1 + (\partial_x b)^2}} \begin{pmatrix} \partial_x b \\ -1 \end{pmatrix} \\ \mathbf{n}^{(k)} &= \frac{1}{\sqrt{1 + (\partial_x k)^2}} \begin{pmatrix} -\partial_x k \\ 1 \end{pmatrix} \end{aligned} \quad (4.1)$$

In contrast to the previous chapter, now the flowing body consists of several different constituents. The single components are assumed to be incompressible, such that the bulk is a particle-fluid mixture or a fluid-fluid mixture. The simplest multi-component mixture for debris flows considers particles in a fluid, but one could also think of more complicated mixtures, one of those is sketched in Figure 4.1.

4.1.2 Single component balance laws

Following Iverson [44], we base our derivation on the theory of multi-phase flows. This theory regards the system as being composed of two or more continuum components, each of which is supposed to exist simultaneously at each point within the set $\{(x, z, t) : b(x) \leq z \leq s(x, t)\}$. Different components are indicated with the subscript i . The field variables

are then given by

$$\begin{aligned} \rho_i & : \text{effective density of species } i \\ \mathbf{u}_i = \begin{pmatrix} u_i \\ w_i \end{pmatrix} & : \text{velocity of species } i \\ \sigma_i = \begin{pmatrix} \sigma_{i,xx} & \sigma_{i,xz} \\ \sigma_{i,zx} & \sigma_{i,zz} \end{pmatrix} & : \text{effective stress tensor of species } i \end{aligned}$$

Here, σ_i is the intra-species and inter-species Cauchy-stress that includes pressures. According to convention in soil and rock mechanics it is considered to be positive in compression.

The conservative formulation of the multi-component balance laws is well-established. Iverson starts his model derivation from the same basis [44]. (The Pitman/Le approach is uses non-conservative primary mass and momentum balances. For a discussion of the differences, we refer to [68, 53]). A detailed derivation of the equations from the local instant formulation will be omitted but can be found in recently published books by Ishii [43] and Drew [29]. The mass and momentum equations for the i -th component are

$$\begin{aligned} \partial_t \rho_i + \nabla \cdot (\rho_i \mathbf{u}_i) &= 0 \\ \partial_t (\rho_i \mathbf{u}_i) + \nabla \cdot (\rho_i \mathbf{u}_i \mathbf{u}_i) &= \nabla \cdot \sigma_i + \rho_i \mathbf{g} + I_i \end{aligned} \tag{4.2}$$

Conservation of angular momentum for every component implies that σ_i is symmetric. \mathbf{g} is the gravitational acceleration vector and I_i accounts for the momentum exchange due to relative motion between the components. Since there is no net mass transfer between the components, the mass of a single component is conserved and the right hand side of the mass balance vanishes. The bulk momentum balance law implies $\sum_i I_i = 0$.

We assume, that the material properties are temperature independent, hence the thermal energy balance is not taken into account. We likewise do not take into account the random fluctuations of the granular material (granular temperature).

4.1.3 Full saturation

The flow is assumed to be fully saturated, such that the condition

$$\sum_i \frac{\rho_i}{\rho_{i,0}} = \sum_i \phi_i = 1 \tag{4.3}$$

is satisfied. $\rho_{i,0}$ denotes the pure, material density of species i , namely its mass per unit volume and ϕ_i stands for the effective component's volume fraction.

4.1.4 Incompressibility and volume-averaged velocity

Incompressibility of the single components implies a constant material density $\rho_{i,0}$, such that the balance laws can be written in the form

$$\begin{aligned}\partial_t \phi_i + \nabla \cdot (\phi_i \mathbf{u}_i) &= 0 \\ \partial_t (\phi_i \mathbf{u}_i) + \nabla \cdot (\phi_i \mathbf{u}_i \mathbf{u}_i) &= -\frac{1}{\rho_{i,0}} \nabla \cdot \sigma_i + \phi_i \mathbf{g} + \frac{1}{\rho_{i,0}} I_i\end{aligned}\quad (4.4)$$

Differentiating equation (4.3) with respect to t and substituting in the mass conservation in the form (4.4) then gives

$$\nabla \cdot \left(\sum_i \phi_i \mathbf{u}_i \right) = 0 \quad (4.5)$$

Therefore, the volume-averaged velocity field \mathbf{u}_v is divergence free.

$$\mathbf{u}_v := \sum_i \phi_i \mathbf{u}_i \quad \Rightarrow \quad \nabla \cdot \mathbf{u}_v = 0 \quad (4.6)$$

It is important to note, that this is not in general true for the mass-averaged velocity field $\mathbf{u} := \frac{1}{\rho} [\sum_i \rho_i \mathbf{u}_i]$. The latter will be the relevant velocity field when formulating bulk mass and momentum balances for the whole mixture.

4.1.5 Viscous drag momentum exchange

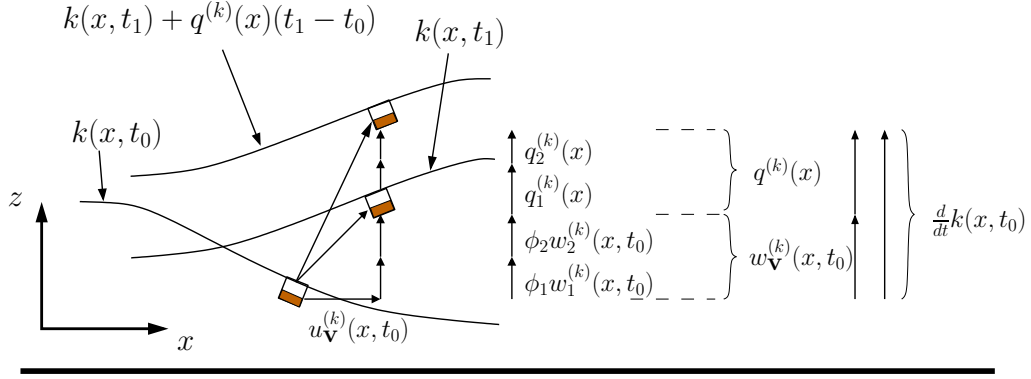
We allow for horizontal and vertical rearrangement of components and relative velocities between the solid and the fluid phase. However, slip velocities are considered to be small and momentum exchange is given by viscous drag. In the case of two components, this means

$$I_2 = -I_1 = \frac{\rho_1 \rho_2}{\rho} \frac{\mathbf{u}_1 - \mathbf{u}_2}{\tau} \quad (4.7)$$

The parameter τ denotes the characteristic relaxation timescale for the momentum exchange.

4.2 Kinematic boundary conditions

Kinematic boundary conditions are specified for every material boundary present in the flow. This includes the basal profile, as well as the upper free surface. The latter is well-defined for fully saturated flows. As a consequence of possible vertical layering, there may also exist material boundaries in the interior of the flow. In the context of debris flows, they are referred to as internal sedimentation lines (compare Figure 4.1).

Figure 4.2: Motion of a material point on the interface $k(x(t), t)$ in a mixture

4.2.1 Generalization to an arbitrary interface

The derivation of kinematic boundary conditions has been described rigorously in Subsection 3.2. It can be generalized in a straight-forward manner to arbitrary interfaces k , which may include the free surface and basal profile, as well as internal material boundaries. To track the position of k , a Lagrangian framework is considered and x and z denote positions on the interface k as functions of t . Since the flow both, consists of individually incompressible components and is fully saturated, the bulk volume is conserved. Hence, the interface is evolved with the volume-averaged velocity $\mathbf{u}_{\mathbf{v}}$, rather than the barycentric velocity \mathbf{u} . The flow then induces a vertical velocity $w_{\mathbf{v}}^{(k)}(x(t), t)$ of every material point, which is given by the total vertical change of k with time $\frac{d}{dt}k(x(t), t)$. For a sketch, we refer to Figure 4.2. In addition to that, the interface k is also affected by the rate of mass production $q_i^{(k)}(x)$ of every component. Of course, mass production rates at possible sedimentation lines in the interior of the flow are subject to further restrictions, and this issue will be addressed later. The bulk mass production rate is then defined as the sum $q^{(k)} = \sum_i q_i^{(k)}$. Similar to previous chapter one gets

$$\frac{\partial}{\partial t}k(x(t), t) + \frac{\partial}{\partial t}x(t) \frac{\partial}{\partial x}k(x(t), t) = w_{\mathbf{v}}^{(k)}(x(t), t) + q^{(k)}(x(t), t) \quad (4.8)$$

The horizontal velocity of a material point is given by $\partial_t x(t) = u_{\mathbf{v}}^{(k)}$, such that we can summarize the kinematic condition into its final version

$$\partial_t k + u_{\mathbf{v}}^{(k)} \partial_x k = w_{\mathbf{v}}^{(k)} + q^{(k)} \quad (4.9)$$

4.2.2 Autonomy assumption

Terms corresponding to the different components are assumed to be independent, such that for every constituent there will be a kinematic condition of the form

$$\phi_i \partial_t k + \phi_i u_i^{(k)} \partial_x k = \phi_i w_i^{(k)} + q_i^{(k)} \quad (4.10)$$

The latter equations are exact, if the composition of a moving material point on the interface is constant. In all other cases an error of the order of the relative velocities is introduced. Although the relative velocities do play a role in the bulk dynamics of the flow, they are considered to be negligible at the interfaces itself.

4.3 Dynamic boundary conditions

The dynamic boundary conditions, acting normal to the interfaces, differ with the type of the material boundary.

The free surface is stress-free for every constituent i

$$\sigma_{\mathbf{i}}^{(s)} \mathbf{n}^{(s)} = \mathbf{0} \quad \Rightarrow \quad \begin{aligned} \sigma_{i,xz}^{(s)} - \sigma_{i,xx}^{(s)} \partial_x s &= 0 \\ \sigma_{i,zz}^{(s)} - \sigma_{i,xz}^{(s)} \partial_x s &= 0 \end{aligned} \quad (4.11)$$

The frictional shear force for the i -th component $\mathbf{S}_{\mathbf{i}}^{(b)}$ at the basal profile acts opposite to the direction of the tangential boundary flow. Its value is given by the friction F_i , a function of the normal stress $\mathbf{N}_{\mathbf{i}}^{(b)} := \mathbf{n}^{(b)T} \left(\mathbf{n}^{(b)T} \cdot \sigma_{\mathbf{i}}^{(b)} \mathbf{n}^{(b)} \right)$ and the basal velocity of the component $\mathbf{u}_{\mathbf{i}}^{(b)}$, such that one gets

$$\mathbf{S}_{\mathbf{i}}^{(b)} = \sigma_{\mathbf{i}}^{(b)} \mathbf{n}^{(b)} - \mathbf{N}_{\mathbf{i}}^{(b)} = - \left(\frac{\mathbf{u}_{\mathbf{i}}^{(b)}}{\|\mathbf{u}_{\mathbf{i}}^{(b)}\|} \right) F_i \left(\mathbf{N}_{\mathbf{i}}^{(b)}, \mathbf{u}_{\mathbf{i}}^{(b)} \right) \quad (4.12)$$

Note that with

$$F_i^{(SH)} \left(\mathbf{N}_{\mathbf{i}}^{(b)}, \mathbf{u}_{\mathbf{i}}^{(b)} \right) := \mu_i \left\| \mathbf{N}_{\mathbf{i}}^{(b)} \right\|$$

one obtains a Coulomb dry friction relation in every component. Furthermore, with

$$F_i^{(VS)} \left(\mathbf{N}_{\mathbf{i}}^{(b)}, \mathbf{u}_{\mathbf{i}}^{(b)} \right) := \mu_i \left\| \mathbf{N}_{\mathbf{i}}^{(b)} \right\| + \xi_i \left(\mathbf{u}_{\mathbf{i}}^{(b)} \right)^2 \quad (4.13)$$

the Voellmy-Salm basal friction relation is recovered. If we solve for the stress normal component, we get

$$\begin{aligned}
\sigma_{i,xx}^{(b)} \partial_x b - \sigma_{i,xz}^{(b)} &= \frac{u^{(b)}}{\|\mathbf{u}^{(b)}\|} F_i \left(\mathbf{N}_i^{(b)}, \mathbf{u}_i^{(b)} \right) + \partial_x b \left\| \mathbf{N}_i^{(b)} \right\| \\
\sigma_{i,xz}^{(b)} \partial_x b - \sigma_{i,zz}^{(b)} &= \frac{w^{(b)}}{\|\mathbf{u}^{(b)}\|} F_i \left(\mathbf{N}_i^{(b)}, \mathbf{u}_i^{(b)} \right) - \left\| \mathbf{N}_i^{(b)} \right\|
\end{aligned} \tag{4.14}$$

At any internal material interface k within the flow, frictional shear forces $\mathbf{S}_i^{(k)}$ are assumed to be negligible. However, normal stresses $\mathbf{N}_i^{(k)} := \mathbf{n}^{(k)T} \left(\mathbf{n}^{(k)T} \cdot \sigma_i^{(k)} \mathbf{n}^{(k)} \right)$ are taken into account. Hence

$$\underbrace{\mathbf{S}_i^{(k)}}_{=\mathbf{0}} = \sigma_i^{(k)} \mathbf{n}^{(k)} - \mathbf{N}_i^{(k)} \tag{4.15}$$

Here $\mathbf{n}^{(k)}$ points in direction of the positive z -domain. All in all

$$\begin{aligned}
\sigma_{i,xz}^{(k)} - \sigma_{i,xx}^{(k)} \partial_x k &= -\partial_x k \left\| \mathbf{N}_i^{(k)} \right\| \\
\sigma_{i,xz}^{(k)} - \sigma_{i,xz}^{(k)} \partial_x k &= \left\| \mathbf{N}_i^{(k)} \right\|
\end{aligned} \tag{4.16}$$

4.4 Dimensionless coordinates

4.4.1 Definition of the scales

The characteristic flow height is denoted by H and the characteristic flow length by L . The one-phase scaling 3.3 is carried over to the multi-phase context, amended by the introduction of an additional characteristic scale for each density $\rho_{i,0}$. An obvious choice for it is given by the pure density of component i . This will also be used in the ongoing of this work. It implies $\rho_i \equiv \phi_i$. Especially for small density differences an alternative choice would be $\rho_{i,0} \equiv \rho_0$ for all i . The advantage of this formulation is, that all equations are rescaled with the same constant value ρ_0 . A characteristic scale for the momentum exchange is given by $g\rho_{i,0}$. Note that for a viscous drag assumption, \mathbf{I}_i is proportional to the horizontal and vertical velocities respectively. Thus, a scale for $I_{i,z}$ is given by $g\rho_{i,0} \frac{H}{L}$. Assuming, that the basal friction has a Coulomb type contribution, which is proportional to the vertical normal stress, the shear stress is scaled with the corresponding friction coefficient μ_i .

Based on the previous considerations, we introduce a scaling of the form

$$\begin{aligned}
x &= L \tilde{x} & z &= H \tilde{z} & t &= \sqrt{\frac{L}{g}} \tilde{t} & \rho_i &= \rho_{i,0} \tilde{\rho}_i \\
u_i &= \sqrt{Lg} \tilde{u}_i & w_i &= \sqrt{Lg} \frac{H}{L} \tilde{w}_i & I_{i,x} &= g\rho_{i,0} \tilde{I}_{i,x} & I_{i,z} &= g\rho_{i,0} \frac{H}{L} \tilde{I}_{i,z} \\
\sigma_{i,xx} &= \rho_{i,0} g H \tilde{\sigma}_{i,xx} & \sigma_{i,xz} &= \rho_{i,0} g H \mu_i \tilde{\sigma}_{i,xz} & \sigma_{i,zz} &= \rho_{i,0} g H \tilde{\sigma}_{i,zz} & & .
\end{aligned}$$

4.4.2 Scaled single component balance laws

In the transformed formulation of the balance laws (4.2), the shallowness parameter $\varepsilon = \frac{H}{L}$ appears several times

$$\begin{aligned} \partial_{\tilde{t}} \tilde{\rho}_i + \partial_{\tilde{x}} \tilde{\rho}_i \tilde{u}_i + \partial_{\tilde{z}} \tilde{\rho}_i \tilde{w}_i &= 0 \\ \partial_{\tilde{t}} (\tilde{\rho}_i \tilde{u}_i) + \partial_{\tilde{x}} (\tilde{\rho}_i \tilde{u}_i^2) + \partial_{\tilde{z}} (\tilde{\rho}_i \tilde{u}_i \tilde{w}_i) &= \varepsilon \partial_{\tilde{x}} \tilde{\sigma}_{i,xx} + \mu_i \partial_{\tilde{z}} \tilde{\sigma}_{i,xz} + \tilde{\rho}_i \sin \zeta + \tilde{I}_{i,x} \\ \varepsilon (\partial_{\tilde{t}} (\tilde{\rho}_i \tilde{w}_i) + \partial_{\tilde{x}} (\tilde{\rho}_i \tilde{u}_i \tilde{w}_i) + \partial_{\tilde{z}} (\tilde{\rho}_i \tilde{w}_i^2)) &= \varepsilon \mu_i \partial_{\tilde{x}} \tilde{\sigma}_{i,xz} + \partial_{\tilde{z}} \tilde{\sigma}_{i,zz} + \tilde{\rho}_i \cos \zeta + \varepsilon \tilde{I}_{i,z} \end{aligned} \quad (4.17)$$

4.4.3 Scaled boundary conditions

By defining $\tilde{q}_i^{(k)} = (\varepsilon g H)^{-\frac{1}{2}} q_i^{(k)}$ the rescaled kinematic condition (4.10) at a material interface k is given by

$$\rho_i \partial_{\tilde{t}} \tilde{k} + \rho_i \tilde{u}_i^{(k)} \partial_{\tilde{x}} \tilde{k} = \rho_i \tilde{w}_i^{(k)} + \tilde{q}_i^{(k)} \quad (4.18)$$

The dynamic boundary conditions for the stress-free surface (4.11) transform into

$$\begin{aligned} \mu_i \tilde{\sigma}_{i,xz}^{(s)} - \varepsilon \tilde{\sigma}_{i,xx}^{(s)} \partial_{\tilde{x}} \tilde{s} &= 0 \\ \tilde{\sigma}_{i,zz}^{(s)} - \varepsilon \mu_i \tilde{\sigma}_{i,xz}^{(s)} \partial_{\tilde{x}} \tilde{s} &= 0 \end{aligned} \quad (4.19)$$

For the bottom topography (4.14) they read as

$$\begin{aligned} \varepsilon \tilde{\sigma}_{i,xx}^{(b)} \partial_{\tilde{x}} \tilde{b} - \mu_i \tilde{\sigma}_{i,xz}^{(b)} &= - \frac{\tilde{u}_i^{(b)}}{\|\tilde{\mathbf{u}}_i^{(b)}\|} F_i \left(\tilde{\mathbf{N}}_i^{(b)}, \tilde{\mathbf{u}}_i^{(b)} \right) - \varepsilon \partial_{\tilde{x}} \tilde{b} \|\tilde{\mathbf{N}}_i^{(b)}\| \\ \varepsilon \mu_i \tilde{\sigma}_{i,xz}^{(b)} \partial_{\tilde{x}} \tilde{b} - \tilde{\sigma}_{i,zz}^{(b)} &= - \frac{\tilde{w}_i^{(b)}}{\|\tilde{\mathbf{u}}_i^{(b)}\|} \varepsilon F_i \left(\tilde{\mathbf{N}}_i^{(b)}, \tilde{\mathbf{u}}_i^{(b)} \right) + \|\tilde{\mathbf{N}}_i^{(b)}\| \end{aligned} \quad (4.20)$$

At internal material boundaries (4.16) transforms into

$$\begin{aligned} \mu_i \tilde{\sigma}_{i,xz}^{(k)} - \varepsilon \tilde{\sigma}_{i,xx}^{(k)} \partial_{\tilde{x}} \tilde{k} &= - \partial_{\tilde{x}} \tilde{k} \|\tilde{\mathbf{N}}_i^{(k)}\| \\ \tilde{\sigma}_{i,zz}^{(k)} - \varepsilon \mu_i \tilde{\sigma}_{i,xz}^{(k)} \partial_{\tilde{x}} \tilde{k} &= \|\tilde{\mathbf{N}}_i^{(k)}\| \end{aligned} \quad (4.21)$$

In the following, all computations will be done in the transformed variables, such that the tildes can be dropped.

4.5 Depth-integration

4.5.1 Flow mass, height and averaging concept

The multi-component system is now integrated along the z -axis. The height of the flow is again defined as

$$h(x, t) := s(x, t) - b(x)$$

However, due to possible differences in the species densities, a density weighted average will be applied. With $m_i := \int_b^s \rho_i dz$, being the (rescaled) mass per unit area of component i , the following notation is introduced

$$\langle \cdot \rangle_i := \frac{\int_b^s \cdot \rho_i dz}{\int_b^s \rho_i dz} = \frac{1}{m_i} \int_b^s \cdot \rho_i dz \quad (4.22)$$

Then $\langle f \rangle_i$ denotes the density weighted, depth-averaged quantity of the function f . Field variables might be discontinuous at internal material boundaries, in which case the integrals have to be evaluated by splitting them into the different layers.

4.5.2 Integrated single species mass conservation

The mass conservation of (4.17) is integrated and results in

$$\begin{aligned} & \int_b^s (\partial_t \rho_i + \partial_x \rho_i u_i + \partial_z \rho_i w_i) dz \\ &= \partial_t m_i + \partial_x (m_i \langle u_i \rangle) - \left[\rho_i \left(\partial_t z + u_i^{(z)} \partial_x z - w_i^{(z)} \right) \right]_b^s \end{aligned} \quad (4.23)$$

To close this equation, we must again derive relations from the boundary conditions. However, these differ with the type of vertical structure in the flow. We will therefore postpone the closure to following section, in which different vertical mixing states are discussed explicitly.

4.5.3 Integrated single species momentum balance

The integrated left-hand-side of the x -momentum balance (4.17) transforms into

$$\begin{aligned} & \int_b^s (\partial_t (\rho_i u_i) + \partial_x (\rho_i u_i^2) + \partial_z (\rho_i u_i w_i)) dz \\ &= \partial_t (m_i \langle u_i \rangle) + \partial_x (C_{u,i} m_i \langle u_i^2 \rangle) - \left[\rho_i u_i^{(z)} \left(\partial_t z + u_i^{(z)} \partial_x z - w_i^{(z)} \right) \right]_b^s \end{aligned} \quad (4.24)$$

Here $C_{u,i} := \frac{\langle u_i^2 \rangle_i}{\langle u_i \rangle_i^2}$ denotes a momentum shape factor for the single components. The right-hand side is given by

$$\begin{aligned} & \int_b^s (\varepsilon \partial_x \sigma_{i,xx} + \mu_i \partial_z \sigma_{i,xz} + \rho_i \sin \zeta) dz \\ &= \partial_x \left(\varepsilon \int_b^s \sigma_{i,xx} dz \right) - [\varepsilon \sigma_{i,xx} \partial_x z - \mu_i \sigma_{i,xz}]_b^s + m_i \sin \zeta + \int_b^s I_{i,x} dz \end{aligned} \quad (4.25)$$

Besides the bracketed terms, that are discussed explicitly in the following sections, we have to close for the depth-averaged squared velocity $\langle u_i^2 \rangle$ and the depth-averaged stress $\int_b^s \sigma_{i,xx} dz$. The depth-averaged momentum exchange $\int_b^s I_{i,x} dz$ will once again be closed by a viscous drag assumption.

4.5.4 Shape factor

In Section 3.5, we analyzed the appearing momentum shape factor C_u for single component flows. We found, that values are close to one for realistic velocity profiles. Pitman and Le carried out a similar analysis for the momentum shape factor $C_{u,i}$ in depth-averaged multi-component flow. An estimate for the range of the momentum shape factor can be found in the appendix to their paper [68]. Based on their results, we will also set $C_{u,i}$ to one.

4.5.5 Averaged stress and vertical center of mass

The normal stress $\sigma_{i,xx}$ has to be treated more carefully, since it contains information on the vertical structure of the flow. The normal stress at the free surface is zero, hence, integrating the vertical momentum balance (4.17), yields an expression for $\sigma_{i,zz}$

$$\sigma_{i,zz}(x, z, t) = \int_z^s \rho_i(x, z', t) \cos \zeta dz' + O(\varepsilon) \quad (4.26)$$

In the corresponding Section 3.6 on one-phase flows, we found a K_i , such that

$$\sigma_{i,xx} = K_i \sigma_{i,zz} \quad (4.27)$$

Under isotropic conditions, hence for a fluid, but also for particles in suspension, there holds $K_i \equiv 1$, whereas it stands for the earth pressure coefficient(3.31) in the case of a non-suspended Mohr-Coulomb material. In any case the coefficient K_i is independent of z and therefore $\int_b^s \sigma_{i,xx} dz$ can be evaluated to be

$$\begin{aligned}
& \int_b^s \sigma_{i,xx}(x, z, t) dz \\
&= K_i \int_b^s \left(\int_z^s \rho_i(x, z', t) \cos \zeta dz' \right) dz = K_i \cos \zeta \int_b^s (z - b) \rho_i(x, z, t) dz \quad (4.28) \\
& \quad K_i \cos \zeta h_i^{(cm)}(x, t) m_i(x, t)
\end{aligned}$$

We make use of the following identity $\int_b^s \int_z^s \rho_i(z') dz' dz = \int_b^s (z - b) \rho_i(z) dz$, which is derived by changing the order of integration. $h_i^{(cm)} := \langle z - b \rangle_i$ denotes the height of the vertical centre of mass at (x, t) . In the case of a homogeneous body, consisting of a single component ($i \equiv 1$), we find $h_1^{(cm)}(x, t) = \frac{1}{2} h(x, t)$, and relation (4.28) reduces to the well-known depth-averaged, hydrostatic pressure, that appears in the one-phase model (3.33).

The result of the integration (4.28) is essential, as it holds for general effective densities, that are not necessarily constant in z . It provides a framework to derive shallow flow equations of different, or even varying vertical states. In order to determine the height of the vertical centre of mass $h_i^{(cm)}$, two characteristic mixture states, namely a uniform suspension, and a completely stratified layering will be analyzed. This analysis will allow us to define a unified approach, combing the uniform suspension with the vertical layering.

4.6 Uniform suspension

Let us consider a uniform suspension of particles in a fluid, like it is sketched in Figure 4.3. The solids are evenly distributed throughout the flow depth, and there holds $\partial_z \rho_i \equiv 0$, $i \in \{1, 2\}$.

4.6.1 Inclusion of the boundary conditions

No internal material interface is present, thus from the boundary conditions derived in Section 4.2 and 4.3, we can deduce the relations

$$\begin{aligned}
\left[\rho_i \left(\partial_t z + u_i^{(z)} \partial_x z - w_i^{(z)} \right) \right]_b^s &= \left[q_i^{(z)} \right]_b^s \\
\left[\rho_i u_i^{(z)} \left(\partial_t z + u_i^{(z)} \partial_x z - w_i^{(z)} \right) \right]_b^s &= \left[u_i^{(z)} q_i^{(z)} \right]_b^s \\
\left[\varepsilon \sigma_{i,xx}^{(z)} \partial_x z - \mu_i \sigma_{i,xz}^{(z)} \right]_b^s &= - \frac{u_i^{(b)}}{\| \mathbf{u}_i^{(b)} \|} F_i \left(\mathbf{N}_i^{(b)}, \mathbf{u}_i^{(b)} \right) - \varepsilon \partial_x b \left\| \mathbf{N}_i^{(b)} \right\|
\end{aligned}$$

Substituting the latter into the depth-averaged mass and momentum balance laws for component i (4.23), (4.25) and (4.24) yields

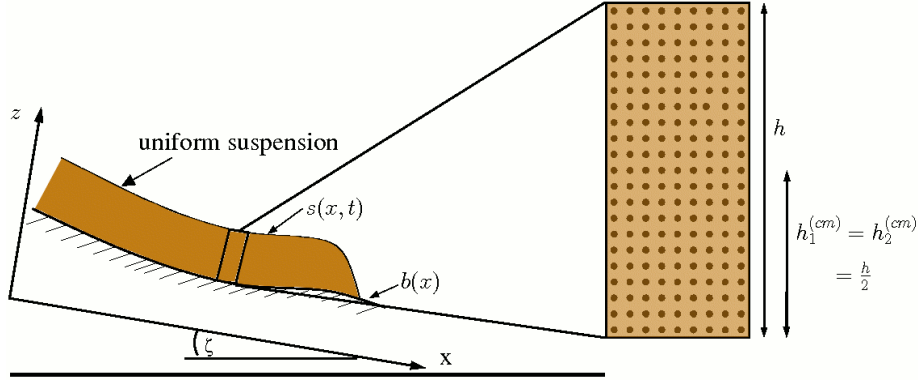


Figure 4.3: Uniform suspension of particles in a fluid - height and height of the vertical center of mass

$$\partial_t m_i + \partial_x (m_i \langle u_i \rangle) = \left[q_i^{(z)} \right]_b^s \quad (4.29)$$

$$\begin{aligned} \partial_t m_i + \partial_x \left(m_i \langle u_i \rangle - \varepsilon \int_s^b \sigma_{i,xx} dz \right) = & \quad (4.30) \\ - \frac{u_i^{(b)}}{\|\mathbf{u}_i^{(b)}\|} F_i \left(\mathbf{N}_i^{(b)}, \mathbf{u}_i^{(b)} \right) - \varepsilon \partial_x b \left\| \mathbf{N}_i^{(b)} \right\| + m_i \sin \zeta + \int_b^s I_{i,x} dz + \left[u_i^{(z)} q_i^{(z)} \right]_b^s \end{aligned}$$

4.6.2 Closure for the vertical center of mass

Due to the vanishing effective density gradient, ρ_i is independent of z . Consequently, the height of the center of mass of both components $h_i^{(cm)}$ is given by half the bulk height (compare once again Figure 4.3)

$$h_i^{(cm)} = \frac{h}{2} \quad (4.31)$$

The suspension is isotropic, such that $K_i = 1$ for all i . Then the equation for the depth-averaged stress (4.28) is closed as a function of h and m_i

$$\int_s^b \sigma_{i,xx} dz = \cos \zeta \frac{h}{2} m_i \quad (4.32)$$

Note, that according to Section 4.4, the effective densities ρ_i have been scaled with the material densities at 100% volume fraction $\rho_{i,0}$. Hence, m_i is nothing but the depth-integrated effective volume fraction per unit area, such that the bulk height is given by the sum over all m_i

$$h = \sum_i m_i \quad (4.33)$$

4.6.3 Averaged momentum exchange

We close the depth-averaged momentum exchange for $i = \{1, 2\}$ directly, and assume

$$\begin{aligned} R_1 &:= \int_b^s I_{1,x} dz = \frac{m_1 m_2}{r m_1 + m_2} \frac{\langle u_2 \rangle - \langle u_1 \rangle}{\tau} \\ R_2 &:= \int_b^s I_{2,x} dz = \frac{r m_1 m_2}{r m_1 + m_2} \frac{\langle u_1 \rangle - \langle u_2 \rangle}{\tau} \end{aligned} \quad (4.34)$$

Again, τ is the significant time scale for the momentum relaxation and $r := \frac{\rho_{1,0}}{\rho_{2,0}}$ is the components density ratio. Note, that the latter choice is consistent to the applied scaling.

4.6.4 Summarized model formulation

Similar to the given one-phase framework, we introduce the abbreviation $U_i := \langle u_i \rangle_i$, neglect terms in $O(\varepsilon^\gamma)$, $\gamma > 1$ and assume a Boussinesq like approximation $u_i^{(k)} = U_i + O(\varepsilon^\gamma)$, $k \in \{b, s\}$. The final depth-integrated model for a vertically uniform suspension of particles in a fluid is then

$$\partial_t \begin{pmatrix} m_1 \\ m_1 U_1 \\ m_2 \\ m_2 U_2 \end{pmatrix} + \partial_x \begin{pmatrix} m_1 U_1 \\ m_1 U_1^2 + \varepsilon \cos \zeta \frac{m_1 + m_2}{2} m_1 \\ m_2 U_2 \\ m_2 U_2^2 + \varepsilon \cos \zeta \frac{m_1 + m_2}{2} m_2 \end{pmatrix} = \begin{pmatrix} \left[q_1^{(z)} \right]_b^s \\ G_1 + S_1 + R_1 \\ \left[q_2^{(z)} \right]_b^s \\ G_2 + S_2 + R_2 \end{pmatrix} \quad (4.35)$$

$$\begin{aligned} G_1 &:= m_1 \sin \zeta - \frac{U_1}{\|U_1\|} \mu m_1 \cos \zeta & S_1 &:= -\varepsilon \cos \zeta m_1 \partial_x b + U_1 \left[q_1^{(z)} \right]_b^s \\ G_2 &:= \underbrace{m_2 \sin \zeta}_{\text{acceleration}} - \underbrace{\frac{U_2}{\|U_2\|} \mu m_2 \cos \zeta}_{\text{basal friction}} & S_2 &:= \underbrace{-\varepsilon \cos \zeta m_2 \partial_x b}_{\text{topography}} + \underbrace{U_2 \left[q_2^{(z)} \right]_b^s}_{\text{entrainment/deposition}} \end{aligned}$$

$$\begin{aligned} R_1 &:= \frac{1}{\tau} \frac{m_1 m_2}{r m_1 + m_2} (U_2 - U_1) \\ R_2 &:= \frac{1}{\tau} \frac{r m_1 m_2}{r m_1 + m_2} (U_1 - U_2) \end{aligned}$$

For the moment, a Coulomb dry friction relation with friction coefficients $\mu_1 = \mu_2 = \mu$ is assumed. It is important to keep in mind, that other friction relations may well include an explicit velocity dependency.

The resulting system (4.35) is in conservation form. The equations for the different components are coupled in the depth-averaged stresses.

4.6.5 Comparison to the Iverson and the Pitman/Le approach

Erosion and deposition rates are neglected for the moment. Multiplying the single component equations by their characteristic densities $\rho_{i,0}$ and summing them up, yields depth-averaged bulk mixture equations, that are similar to Iverson's model (before imposing the pore pressure relation).

Both, Iverson's mixture theory and the single-component Pitman/Le approach, implicitly use a uniform suspension assumption within their derivation. The difference between the Pitman/Le theory and the uniform suspension model, proposed within this thesis, is due to the different underlying formulation of the balance laws before the averaging step.

A final comment in this section is devoted to a clear advantage of the uniform suspension model (4.35). It can easily be extended to an arbitrary number of different components. As long as the requirement of a uniform suspension is fulfilled, the single species height of the vertical center of mass is determined by the bulk height according to $h_i^{cm} = \frac{h}{2}$.

4.7 Vertical layering

Now, we consider a vertical layering of two different components, as demonstrated in Figure 4.4. Differences to the previous section are that

- the single vertical center of masses $h_i^{(cm)}$ are not given by $\frac{h}{2}$ any longer
- next to the upper free surface and the bottom profile, an additional internal material interface k exists, which determines the boundary between both species

The layer heights are defined according to

$$h_1(x, t) := s(x, t) - k(x, t) \quad h_2(x, t) := k(x, t) - b(x, t) \quad (4.36)$$

At the internal interface the mass production rates are zero, meaning $q_i^{(k)} = 0$.

4.7.1 Incorporated boundary conditions

In the two-layer case, the field variables are discontinuous at the internal material boundary. That is why the depth-integration is performed layer-wise. However, the depth-integrated mass and momentum balances (4.23), (4.24), (4.25) are unchanged.

The kinematic conditions are unchanged in comparison to the uniform suspension case. This is a result of the zero mass production at the internal interface. In contrast to

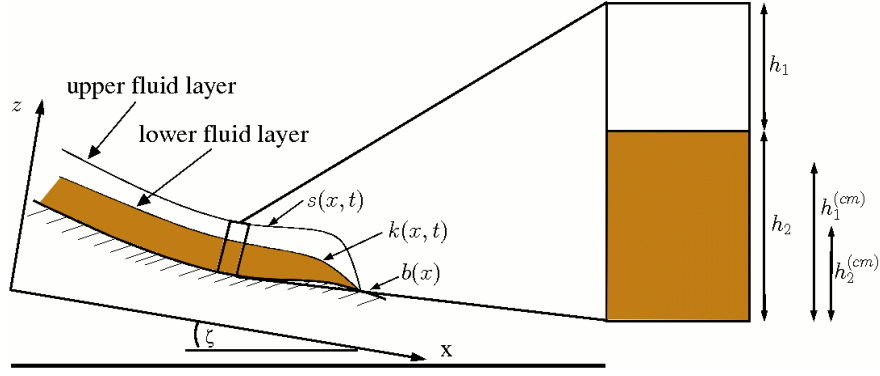


Figure 4.4: Layer heights and vertical center of masses of the single components in two-layer shallow flow

this, the dynamic conditions do change, as they directly reflect acting and reacting forces at the internal material boundary. The boundary conditions for the two-layer case are summarized as follows

$$\begin{aligned}
 [\rho_i (\partial_t z + u_i \partial_x z - w_i)]_b^s &= [q_i^{(z)}]_b^s \\
 [\rho_i u_i (\partial_t z + u_i \partial_x z - w_i)]_b^s &= [u_i^{(z)} q_i^{(z)}]_b^s \\
 [\varepsilon \sigma_{1,xx}^{(z)} \partial_x z - \mu_1 \sigma_{1,xz}^{(z)}]_k^s &= -\varepsilon \partial_x k \|\mathbf{N}_1^{(k)}\| \\
 [\varepsilon \sigma_{2,xx}^{(z)} \partial_x z - \mu_2 \sigma_{2,xz}^{(z)}]_b^k &= \varepsilon \partial_x k \|\mathbf{N}_2^{(k)}\| - \frac{u_2^{(b)}}{\|\mathbf{u}_2^{(b)}\|} F_2(\mathbf{N}_2^{(b)}, \mathbf{u}_2^{(b)}) - \varepsilon \partial_x b \|\mathbf{N}_2^{(b)}\|
 \end{aligned}$$

Due to the applied scaling and the fact, that we divided the equations by the single components material densities, the dimensionless values of the normal stresses are given by

$$\begin{aligned}
 \|\mathbf{N}_1^{(k)}\| &= \frac{1}{\rho_1^0 g H} \cdot (\rho_1^0 g_z h_1) = m_1 \cos \zeta \\
 \|\mathbf{N}_2^{(k)}\| &= \frac{1}{\rho_2^0 g H} \cdot (\rho_1^0 g_z h_1) = \frac{\rho_1^0}{\rho_2^0} m_1 \cos \zeta \\
 \|\mathbf{N}_2^{(b)}\| &= \underbrace{\frac{1}{\rho_2^0 g H}}_{\text{scaling}} \cdot \underbrace{(\rho_1^0 g_z h_1 + \rho_2^0 g_z h_2)}_{\text{normal stress}} = \frac{\rho_1^0}{\rho_2^0} m_1 \cos \zeta + m_2 \cos \zeta
 \end{aligned} \tag{4.37}$$

With r denoting the density ratio $\frac{\rho_{1,0}}{\rho_{2,0}}$, acting and reacting forces at the internal material

boundary are given by

$$\begin{aligned} A_1 &:= \varepsilon \partial_x k \left\| \mathbf{N}_1^{(k)} \right\| = \varepsilon \cos \zeta m_1 \partial_x k \\ A_2 &:= \varepsilon \partial_x k \left\| \mathbf{N}_2^{(k)} \right\| = \varepsilon \cos \zeta r m_1 \partial_x k \end{aligned} \quad (4.38)$$

In this formulation, it is not immediately obvious that both forces are equal in magnitude. However, this is only due to the different scaling applied in the single momentum equations, such that momentum conservation is fulfilled.

4.7.2 Averaged normal stresses

The normal stresses are depth-integrated in layers. For both layers relation (4.28) is applied. For the second, lower one however, the superimposed load m_1 has to be considered as a boundary condition and we compute $\int_b^k m_1 dz = h_2 m_1 = r h_1 m_2$. Then the depth-integrated stresses $\sigma_{1,xx}$ and $\sigma_{2,xx}$ are evaluated to be

$$\begin{aligned} \int_k^s \sigma_{1,xx} dz &= K_1 \cos \zeta \frac{h_1}{2} m_1 \\ \int_b^k \sigma_{2,xx} dz &= K_2 \cos \zeta \left(\frac{h_2}{2} + r h_1 \right) m_2 \end{aligned}$$

4.7.3 Summarized model formulation

Likewise to the previous section, U_i denotes the averaged velocity $\langle u_i \rangle_i$, and terms in $O(\varepsilon^\gamma)$, $\gamma > 1$ are neglected. Basal friction is assumed to be given by a dry Coulomb relation with respect to the bulk mass. Then, the final depth-integrated model for a completely layered shallow flow situation results in

$$\partial_t \begin{pmatrix} m_1 \\ m_1 U_1 \\ m_2 \\ m_2 U_2 \end{pmatrix} + \partial_x \begin{pmatrix} m_1 U_1 \\ m_1 U_1^2 + \varepsilon K_1 \cos \zeta \frac{h_1}{2} m_1 \\ m_2 U_2 \\ m_2 U_2^2 + \varepsilon K_2 \cos \zeta \left(\frac{h_2}{2} + r h_1 \right) m_2 \end{pmatrix} = \begin{pmatrix} \left[q_1^{(z)} \right]_b^s \\ G_1 + S_1 - A_1 \\ \left[q_2^{(z)} \right]_b^s \\ G_2 + S_2 + A_2 \end{pmatrix} \quad (4.39)$$

$$\begin{aligned} G_1 &:= m_1 \sin \zeta & S_1 &:= -\varepsilon \cos \zeta m_1 \partial_x b + U_1 \left[q_1^{(z)} \right]_b^s \\ G_2 &:= \underbrace{m_2 \sin \zeta}_{\text{acceleration}} - \underbrace{\frac{U_2}{\|U_2\|} \mu (r m_1 + m_2) \cos \zeta}_{\text{basal friction}} & S_2 &:= -\underbrace{\varepsilon \cos \zeta m_2 \partial_x b}_{\text{topography}} + \underbrace{U_2 \left[q_2^{(z)} \right]_b^s}_{\text{entrainment/deposition}} \end{aligned}$$

$$\begin{aligned} A_1 &:= \varepsilon \cos \zeta m_1 \partial_x h_2 \\ A_2 &:= \varepsilon \cos \zeta r m_1 \partial_x h_2 \end{aligned}$$

In contrast to the uniform suspension model, it is given in non-conservative form. This is due to the explicitly appearing forces at the interface on the right hand side of the equation.

4.7.4 Comparison to the two-layer shallow water theory

For the uniform suspension model, there is a close relation to Iverson's approach. Here, it is important to note the similarities to yet another shallow flow model, the two-layer shallow water equations. In the special case of a flat plane $\zeta = 0$, zero mass-production rates at the bottom and the surface $q_i^{(s)} = q_i^{(b)} = 0$ and isotropic stress in both components $K_1 = K_2 = 1$, one recovers the two-layer-shallow water model. Due to the scaling m_i and h_i are equivalent, such that $m_i \equiv h_i$. However, in contrast to the previously derived model formulation (4.39), the common way to write the two-layer shallow water system is the following

$$\partial_t \begin{pmatrix} h_1 \\ h_1 U_1 \\ h_2 \\ h_2 U_2 \end{pmatrix} + \partial_x \begin{pmatrix} h_1 U_1 \\ h_1 U_1^2 + \varepsilon \frac{h_1^2}{2} \\ h_2 U_2 \\ h_2 U_2^2 + \varepsilon \frac{h_2^2}{2} \end{pmatrix} = \begin{pmatrix} 0 \\ S_1 \\ 0 \\ S_2 \end{pmatrix} \quad (4.40)$$

$$\begin{aligned} S_1 &:= -\varepsilon h_1 \partial_x b - \varepsilon h_1 \partial_x h_2 \\ S_2 &:= -\varepsilon h_2 \partial_x b - \varepsilon r h_2 \partial_x h_1 \end{aligned}$$

Recent improvements of numerical methods for two-layer shallow flow are based on this formulation (e.g. Bouchut [12]). In comparison to (4.39), the coupling term in the flux function $r h_1 h_2$ has been shifted to the right hand side and expanded by means of the product rule

$$\partial_x (\varepsilon r h_1 h_2) = \varepsilon r h_1 \partial_x h_2 + \varepsilon r h_2 \partial_x h_1 \quad (4.41)$$

Hence, the first term cancels with the interface force and the remaining term is the second part of the cross-coupling in the flux. As a consequence of these rearrangements, the flux function of the vertically layered model \mathbf{F}_{v12} involves coupling between the components,

which is indicated by the red term (\mathbf{V} being the vector of state variables).

$$\mathbf{F}_{\text{vl2}}(\mathbf{V}) = \begin{pmatrix} h_1 U_1 \\ h_1 U_1^2 + \varepsilon \frac{h_1^2}{2} \\ h_2 U_2 \\ h_2 U_2^2 + \varepsilon \frac{h_2^2}{2} + \varepsilon r h_1 h_2 \end{pmatrix}$$

In the flux function of the two-layer shallow water system \mathbf{F}_{sw2} the two species are uncoupled.

$$\mathbf{F}_{\text{sw2}}(\mathbf{V}) = \begin{pmatrix} h_1 U_1 \\ h_1 U_1^2 + \varepsilon \frac{h_1^2}{2} \\ h_2 U_2 \\ h_2 U_2^2 + \varepsilon \frac{h_2^2}{2} \end{pmatrix}$$

The latter resumes two individual one-phase shallow water systems. It should be noted, that the proposed model for a vertical layering of different components is easily extended to more than 2 components.

4.8 Combined approach

The last two sections dealt with two special vertical flow structures. They can be interpreted as the limiting states of a unified theory. Let us once again consider a fluid-particles mixture. Due to gravity and the fact, that the solids are denser than the surrounding fluid, the particles will eventually settle down to the ground. In contrast to this, a non-zero horizontal flow velocity generates shear stresses at the interface and causes for re-suspension of the particles, meaning vertical mixing of the species. Hence, sedimentation and re-suspension are competing physical processes. A combined approach that includes both, is modeled as follows.

4.8.1 General setting

The bulk of the flow is split into two layers. For a sketch of the vertical structure, see Figure 4.5. In the upper layer, particles are uniformly suspended in the surrounding fluid. The fluid is denoted by the subscript 1, the particles by the subscript 2. The lower layer consists of completely settled particles in its maximum packing state. Although they have the same density as the suspended particles, they are referred to as a third component within the flow, indicated by the subscript 3. Recalling on the effective stress concept introduced in the Chapter 1.3, the fraction of settled particles is exactly the kind of information one needs to reconstruct the effective fluid pressure at the base of the flow. The material densities are given by $\rho_{f,0}$ for the fluid (component 1) and $\rho_{s,0}$ for both, suspended and settled particles (component 2 and 3). Note that this differs from the convention within the previous section, where the pure densities of species i have consistently

been denoted by $\rho_{i,0}$.

The layers are separated by the sedimentation line k . The layer heights are defined according to

$$h_{12}(x, t) := s(x, t) - k(x, t) \quad h_3(x, t) := k(x, t) - b(x, t)$$

The upper layer is in uniform suspension, such that m_{12} and the effective density ρ_{12} are given by

$$m_{12} = m_1 + m_2 \quad \rho_{12} = \frac{m_1 \rho_{f,0} + m_2 \rho_{s,0}}{m_1 + m_2}$$

The ratio between fluid and solid pure density r and between effective density of the upper and lower layer r_{12} are evaluated to be

$$r = \frac{\rho_{f,0}}{\rho_{s,0}} \quad r_{12} = \frac{\rho_{12}}{\rho_{s,0}} = \frac{r m_1 + m_2}{m_1 + m_2}$$

Note that r_{12} is not constant, but varies with the amount of settled particles. It eventually reduces to r , when all particles have settled down to the ground ($m_2 \rightarrow 0$).

4.8.2 Boundary conditions

The mass production rate at the sedimentation line k accounts for sedimentation and re-suspension of the particles. Hence, it influences component 2 and 3, whereas the mass production rate of the fluid is zero. Due to mass conservation and the requirement of full saturation, the production rates are related according to

$$q_2 = -q_3,$$

such that only a single production rate $q := q_2 = -q_3$ has to be taken into account. The additional consideration of sedimentation and re-suspension makes a layer-wise formulation of the boundary conditions necessary. Only the relevant relations are listed.

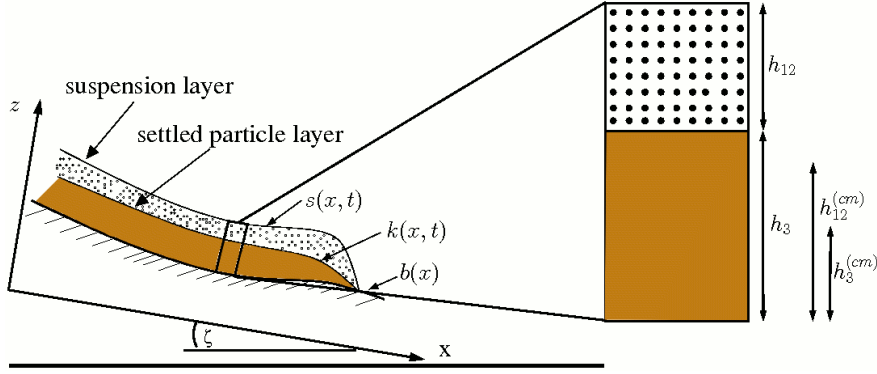


Figure 4.5: The particles are uniformly suspended in the upper layer and completely settled in the lower layer

Kinematic conditions:

$$\begin{aligned}
 [\rho_1 (\partial_t z + u_1 \partial_x z - w_1)]_k^s &= 0 \\
 [\rho_2 (\partial_t z + u_2 \partial_x z - w_2)]_k^s &= -q \\
 [\rho_3 (\partial_t z + u_3 \partial_x z - w_3)]_b^k &= q \\
 [\rho_1 u_1 (\partial_t z + u_1 \partial_x z - w_1)]_k^s &= 0 \\
 [\rho_2 u_2 (\partial_t z + u_2 \partial_x z - w_2)]_k^s &= -u_2 q \\
 [\rho_3 u_3 (\partial_t z + u_3 \partial_x z - w_3)]_b^k &= u_3 q
 \end{aligned}$$

Dynamic conditions:

$$\begin{aligned}
 [\varepsilon \sigma_{1,xx}^{(z)} \partial_x z - \mu_1 \sigma_{1,xz}^{(z)}]_k^s &= -\varepsilon \partial_x k \|\mathbf{N}_1^{(k)}\| \\
 [\varepsilon \sigma_{2,xx}^{(z)} \partial_x z - \mu_2 \sigma_{2,xz}^{(z)}]_b^k &= -\varepsilon \partial_x k \|\mathbf{N}_2^{(k)}\| \\
 [\varepsilon \sigma_{xx}^{(z)} \partial_x z - \mu_3 \sigma_{xz}^{(z)}]_b^k &= \varepsilon \partial_x k \|\mathbf{N}_3^{(k)}\| - \frac{u_3^{(b)}}{\|\mathbf{u}_3^{(b)}\|} F_3(\mathbf{N}_3^{(b)}, \mathbf{u}_3^{(b)}) - \varepsilon \partial_x b \|\mathbf{N}_3^{(b)}\|
 \end{aligned}$$

4.8.3 Averaged normal stresses

Computation of the depth-averaged stresses is once again performed in layers and relies on (4.28). Compare also 4.6.2 and 4.7.2. The stress state in the upper layer is isotropic ($K_i \equiv 1, i \in \{1, 2\}$), whereas it follows a Coulomb criteria in the lower one ($K := K_3$).

The depth-averaged normal stresses are then evaluated to be

$$\begin{aligned}\int_k^s \sigma_{1,xx} dz &= \cos \zeta \frac{h_{12}}{2} m_1 \\ \int_k^s \sigma_{2,xx} dz &= \cos \zeta \frac{h_{12}}{2} m_2 \\ \int_b^k \sigma_{3,xx} dz &= K \cos \zeta \left(\frac{h_3}{2} + r_{12} h_{12} \right) m_3\end{aligned}$$

4.8.4 Final model formulation

For the sake of simplicity, we assume a flow without deposition and entrainment at the free surface and the basal profile. These can be included in a straight-forward manner analogously to the previous sections. According to the established notation convention, the full set of equations is given by

$$\partial_t \begin{pmatrix} m_1 \\ m_1 U_1 \\ m_2 \\ m_2 U_2 \\ m_3 \\ m_3 U_3 \end{pmatrix} + \partial_x \begin{pmatrix} m_1 U_1 \\ m_1 U_1^2 + \varepsilon \cos \zeta \frac{h_{12}}{2} m_1 \\ m_2 U_2 \\ m_2 U_2^2 + \varepsilon \cos \zeta \frac{h_{12}}{2} m_2 \\ m_3 U_3 \\ m_3 U_3^2 + \varepsilon K \cos \zeta \left(\frac{h_3}{2} + r_{12} h_{12} \right) m_3 \end{pmatrix} = \begin{pmatrix} 0 \\ G_1 + S_1 + R_1 - A_1 \\ -q \\ G_2 + S_2 + R_2 - A_2 \\ q \\ G_3 + S_3 + A_3 \end{pmatrix} \quad (4.42)$$

$$\begin{aligned}R_1 &:= \frac{1}{\tau} \frac{m_1 m_2}{r m_1 + m_2} (U_2 - U_1) \\ R_2 &:= \frac{1}{\tau} \frac{r m_1 m_2}{r m_1 + m_2} (U_1 - U_2)\end{aligned}$$

$$\begin{aligned}A_1 &:= \varepsilon \cos \zeta m_1 \partial_x h_3 \\ A_2 &:= \varepsilon \cos \zeta m_2 \partial_x h_3 \\ A_3 &:= \varepsilon \cos \zeta r_{12} (m_1 + m_2) \partial_x h_3\end{aligned}$$

$$\begin{aligned}G_1 &:= m_1 \sin \zeta & S_1 &:= -\varepsilon \cos \zeta m_1 \partial_x b \\ G_2 &:= m_2 \sin \zeta & S_2 &:= -\varepsilon \cos \zeta m_2 \partial_x b \\ G_3 &:= \underbrace{m_3 \sin \zeta}_{\text{acceleration}} - \underbrace{\frac{U_3}{\|U_3\|} \mu (r_{12} (m_1 + m_2) + m_3) \cos \zeta}_{\text{basal friction}} & S_3 &:= -\underbrace{\varepsilon \cos \zeta m_3 \partial_x b}_{\text{topography}}\end{aligned}$$

In a completely stratified state, averaged mass and momentum equations for the suspended particles are redundant and the equations reduce to the vertically layered state, discussed in Section 4.7. In the suspension limit component 3 vanishes, and the system reduces to the uniform suspension model analyzed in Section 4.6. In between, the vertical structure varies according to the mass production rate q , that accounts for sedimentation and re-suspension of the particles.

4.8.5 Sedimentation and Re-suspension

When we want to solve the system, we have to specify the mass production rate q at the sedimentation line. We identify sedimentation and re-suspension of particles to be the competing physical processes, such that as a first approximation, q is formulated as the superposition of both

$$q = q_{\text{sed}} + q_{\text{re}} \quad (4.43)$$

Sedimentation

Consider a simple bucket situation, likewise to the initial motivation in Section 1.3. The bottom is flat, such that $\zeta = 0$ and $b \equiv b_{\text{const.}}$. Horizontal flow vanishes, meaning $U_i \equiv 0, i \in \{1, 2, 3\}$, and consequently $\partial_x(\cdot) \equiv 0$ for every quantity in the system. Then, system (4.42) reduces to an ordinary differential equation for the sedimentation process.

$$\frac{d}{dt} \begin{pmatrix} m_1 \\ m_2 \\ m_3 \end{pmatrix} = \begin{pmatrix} 0 \\ -q_{\text{sed}} \\ q_{\text{sed}} \end{pmatrix} \quad (4.44)$$

Note, that within the framework of pure sedimentation, q_{re} is zero, from which it is immediately obvious, that q_{re} is proportional to some exponent of the horizontal flow.

Due to the applied scaling, the mass production rate q_{sed} reduces to a settling velocity. In the simplest case, which is also valid for a single particle in a fluid, q_{sed} is given by the final settling, or Stokes velocity u_{st} . The latter can also be interpreted as the product of the momentum relaxation timescale τ and gravitational acceleration, such that $u_{\text{st}} = \tau \mathbf{g}$. However, in a high-concentrated suspension, the velocity is also affected by the presence of many other particles, and one speaks of hindered settling. Various forms for the hindered settling have been suggested throughout the years. A rather simple, yet successful approach is due to Kynch (compare [56]). According to his theory, the settling velocity is given by

$$q_{\text{sed}} = (1 - \rho_2) u_{\text{st}} = \rho_1 u_{\text{st}} \quad (4.45)$$

Thus, for a vanishing amount of particles in the suspension layer ($\rho_2 \approx 0$), the settling velocity is given by u_{st} , whereas in the other limit ($\rho_2 \approx \rho_{12}$), no sedimentation will occur. By substituting $\rho_{\text{max}} - \rho_2$ for $1 - \rho_2$ in the latter expression, we can account for a theoretical maximum packing fraction smaller than one $\rho_{\text{max}} < 1$. For other, recently achieved results on hindered settling velocities, we refer to [9, 8].

Re-suspension

Non-vanishing horizontal velocity differences at the sedimentation line causes shear stresses and re-suspension takes place. Models for the latter correspond to those for the entrainment process at the base of a granular flow. In the simplest case the amount of entrained, or re-suspended material or in our case, is proportional to the dynamic pressure at the interface \mathbf{P}_{dyn} . The latter is defined by the product of the density ρ_{12} and the effective barycentric velocity U_{12} with respect to the interface.

$$\mathbf{P}_{\text{dyn}} := \rho_{12} U_{12}^2 = \frac{m_1 \rho_{f,0} + m_2 \rho_{s,0}}{m_1 + m_2} \left(\left(\frac{m_1}{m_1 + m_2} U_1 + \frac{m_2}{m_1 + m_2} U_2 - U_3 \right) \right)^2$$

4.9 Connection to the basal fluid pressure

The proposed depth-averaged single component model provides a framework for the formulation of shallow flow equations. It explicitly allows for changes in the vertical structure. However, to apply the model and compare computations to actual measurements, we still have to fill the gap between theoretical model quantities and observable data in realistic events.

The initial motivation of this thesis, was mainly based on measurements of the normal stresses and basal fluid pressure in different debris flow events. Both quantities do not appear explicitly in the equations, however, the normal stress is simply given by the bulk mass per unit area ($m := \sum_i \rho_{i,0} m_i$) times the gravitational acceleration. To illuminate the basal fluid pressure, let us assume, that the settled particles in the lower layer exhibit a void fraction, that is big enough to maintain a hydrostatic fluid pressure. Then the fluid pressure is computed from the variables in our system according to

$$\tilde{\mathbf{P}}_{\text{eff}} = \mathbf{g} (m_3 \rho_{f,0} + (m_1 + m_2) \rho_{12}) \quad (4.46)$$

The tilde on \mathbf{P}_{eff} denotes, that here the formulation is given in terms of the scaled quantities. In the absence of horizontal flow, and by making use of (4.44), we can directly deduce a differential equation for the basal fluid pressure.

$$\frac{d}{dt} \mathbf{P}_{\text{eff}} = \mathbf{g} (\rho_{f,0} - \rho_{12}) q \quad (4.47)$$

Thus, in the stationary state, no particles are present any more in the suspension. Hence, we get $\rho_{f,0} = \rho_{12}$, and the basal fluid pressure is constant. The latter results holds also for the simplest possible closure for q , according to which a simple Stokes velocity is assumed.

Chapter 5

Mathematical properties

In the previous chapter, we derived a depth-averaged system of conservation laws for shallow multi-component flow. It allows for a change in the vertical mass distribution. In one limit it models a uniform suspension, whereas in the other limit, it coincides with the two-layer shallow water equations. The latter is well-known and a discussion of its mathematical properties can be found in the pioneering work of Armi [3, 4], but also in recently published work on numerical schemes for the two-layer shallow water model [1, 12]. The uniform suspension limit however is discussed in detail, since this part is found to be new and a detailed analysis of its mathematical properties does not exist so far.

5.1 Wave speeds and region of hyperbolicity

The shallow water model, as well as any existing one-phase shallow flow model for geophysical flows, is strictly hyperbolic within its physical domain of positive masses. In the case of zero heights, it is linearly degenerate. In the multi-component context subtleties come into play, as the system is conditionally hyperbolic. However, the ellipticity in the system is not a result of the depth-integration itself, but a familiar problem in multi-phase modeling (e.g. [80, 79, 31]).

5.1.1 Characteristic polynomial

In the following the hyperbolic structure of the uniform suspension limit of a two-component flow is analyzed. Let us consider the homogeneous version of the system. With $C_{i,u} = 1$, $c := \varepsilon \cos \zeta$, $\mathbf{c} := (c, c)^T$ and $\mathbf{m} := (m_1, m_2)^T$, it is given by

$$\partial_t \mathbf{V} + \partial_x \mathbf{F}(\mathbf{V}) = \mathbf{0} \tag{5.1}$$

with

$$\mathbf{V} := \begin{pmatrix} m_1 \\ m_2 \\ m_1 U_1 \\ m_2 U_2 \end{pmatrix} \quad \mathbf{F}(\mathbf{V}) := \begin{pmatrix} m_1 U_1 \\ m_2 U_2 \\ m_1 U_1^2 + \frac{1}{2}(\mathbf{c}^T \mathbf{m}) m_1 \\ m_2 U_2^2 + \frac{1}{2}(\mathbf{c}^T \mathbf{m}) m_2 \end{pmatrix}$$

Conserved quantities are the depth-averaged masses m_1, m_2 and the depth-averaged momenta $m_1 U_1, m_2 U_2$ of both components. The Jacobian of the flux function is evaluated to be

$$D\mathbf{F}(\mathbf{V}) = \begin{pmatrix} 0 & 0 & 1 & 0 \\ 0 & 0 & 0 & 1 \\ -U_1^2 + cm_1 + \frac{1}{2}cm_2 & \frac{1}{2}cm_1 & 2U_1 & 0 \\ \frac{1}{2}cm_2 & -U_2^2 + cm_2 + \frac{1}{2}cm_1 & 0 & 2U_2 \end{pmatrix}$$

Hence, the characteristic function is a 4th order polynomial of the form

$$p_{(m_1, m_2, U_1, U_2, c)}(\lambda) = \lambda^4 + A\lambda^3 + B\lambda^2 + C\lambda + D$$

$$A := -2(U_1 + U_2)$$

$$B := -\frac{3}{2}cm_1 - \frac{3}{2}cm_2 + U_1^2 + 4U_1U_2 + U_2^2$$

$$C := -2U_1^2U_2 - 2U_2^2U_1 + 2cm_1U_2 + cm_1U_1 + 2cm_2U_1 + cm_2U_2$$

$$D := -\frac{1}{2}cm_2U_2^2 - cm_1U_2^2 - \frac{1}{2}U_1^2cm_1 - U_1^2cm_2 + \frac{1}{2}c^2m_1^2 + cm_2cm_1 + \frac{1}{2}c^2m_2^2 + U_1^2U_2^2$$

The polynomial reduces into a much simpler form, when it is shifted by the components mean velocity $\frac{U_1+U_2}{2}$ and written in the weighted slip velocity u^* and the weighted mass difference m^* . Hence, we introduce the transformation

$$\eta := \frac{\lambda - \frac{U_1+U_2}{2}}{\sqrt{\mathbf{c}^T \mathbf{m}}} \quad u^* := \frac{U_1 - U_2}{\sqrt{\mathbf{c}^T \mathbf{m}}} \quad m^* := \frac{(m_2 - m_1)}{m_1 + m_2} \quad (5.2)$$

and the polynomial turns into

$$p_{(u^*, m^*, \mathbf{c}^T \mathbf{m})}(\eta) = (\mathbf{c}^T \mathbf{m})^2 \cdot \left(\eta^4 - \frac{1}{2}(u^{*2} + 3)\eta^2 + \frac{1}{2}u^* m^* \eta + \frac{1}{16}(u^{*2} - 4)(u^{*2} - 2) \right)$$

In the case of vanishing horizontal slip ($u^* \equiv 0$) the linear terms drops out, and all other coefficients reduce to constants. Then, the roots are evaluated to be

$$\eta_{1,2} = \pm 1 \quad \eta_{3,4} = \pm \frac{1}{\sqrt{2}}$$

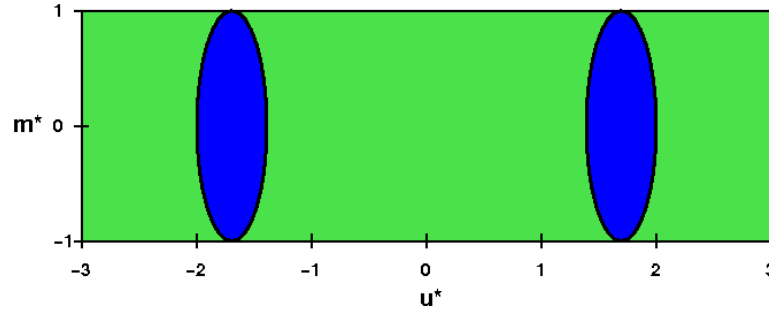


Figure 5.1: Hyperbolic region of the two-component uniform suspension system. Regions with 4 real eigenvalues are green, regions with 2 real and 2 complex eigenvalues are blue

They do not depend on the mass difference, because with the linear term also m^* disappears from the equation.

If on the other hand the slip velocity is non-zero, but the masses coincide ($m^* \equiv 0$), the roots of the polynomial have an explicit u^* -dependency. We get

$$\eta_{1,2} = \pm \frac{1}{2} \sqrt{u^{*2} + 3 + \sqrt{12 u^{*2} + 1}} \quad \eta_{3,4} = \pm \frac{1}{2} \sqrt{u^{*2} + 3 - \sqrt{12 u^{*2} + 1}}$$

Here, the first pair of roots $\eta_{1,2}$ is always real. However, the second is real only for reasonably small and very large slip velocities. In particular we have

$$\eta_{3,4} \in \mathbb{R} \quad \Leftrightarrow \quad |u^*| \notin [\sqrt{2}, 2]$$

5.1.2 Remark on the two-layer system

It should be noted, that also the vertical layering limit of the combined single component mixture approach is conditionally hyperbolic. However, this time, the elliptic region in the system has a clear physical interpretation. For a small velocity difference $U_1 - U_2$, one can derive a sufficient criteria for the roots to be real. It is given by

$$(U_1 - U_2)^2 < (1 - r)g(m_1 + m_2) \quad (5.3)$$

In fact, condition (5.3) is well known in fluid mechanics of shear layer flow. Any violation leads to Kelvin Helmholtz instabilities [28].

5.1.3 Region of hyperbolicity

For arbitrary u^* and m^* the roots cannot be written in a simple closed form. However, by direct curve sketching it becomes obvious, that the polynomial is W-shaped with two

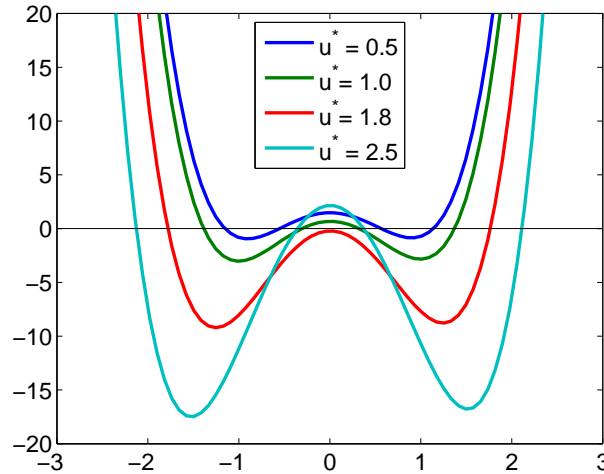


Figure 5.2: Characteristic polynomial along a path through the phase space for $m^* = 0.3$

local minima and a local maximum in the middle. Independent of m^* and u^* , the minima are negative, while the asymptotic behavior of p is given by

$$\lim_{\eta \rightarrow \pm\infty} p_{(u^*, m^*, \mathbf{c}^T \mathbf{m})}(\eta) = \infty$$

Hence, by applying the intermediate value theorem, we can immediately deduce the existence of two real roots on the outer side of both of the minima. These correspond to the first pair of roots $\eta_{1,2}$. For a positive intermediate local maximum, a second pair of real roots exists, this time corresponding to $\eta_{3,4}$. Hence, the system has a complete set of real roots and is hyperbolic. For a negative local maximum however, the second pair is complex and hyperbolicity is lost. Figure 5.1 shows a plot of the projected phase space, the axis being m^* and u^* . The green region denotes hyperbolicity of the system, in the blue region the second pair of roots is complex.

Figure 5.2 shows a plot of the polynomial for various locations along the path $m^* \equiv 0.3, u^* \geq 0$. For a small slip velocity, the polynomial has a positive local maximum, thus four real roots. As u^* increases, the local maximum decreases and it eventually becomes negative. However, as u^* gets larger, the local maximum enters the positive domain again and the system recovers its hyperbolic properties. The same behavior holds true for paths into the negative u^* -domain.

The momentum shape factors $C_{i,u}$, which indicate the deviation of the velocity profile from the plug flow limit, have been set to one in the eigenvalue analysis. Note, that for positive shape factors different from one, the general structure of the hyperbolic regions is still similar. The elliptic regions are distorted and shifted, but they are still present in the phase space. Note also, that negative $C_{i,u}$ are not possible and are therefore not

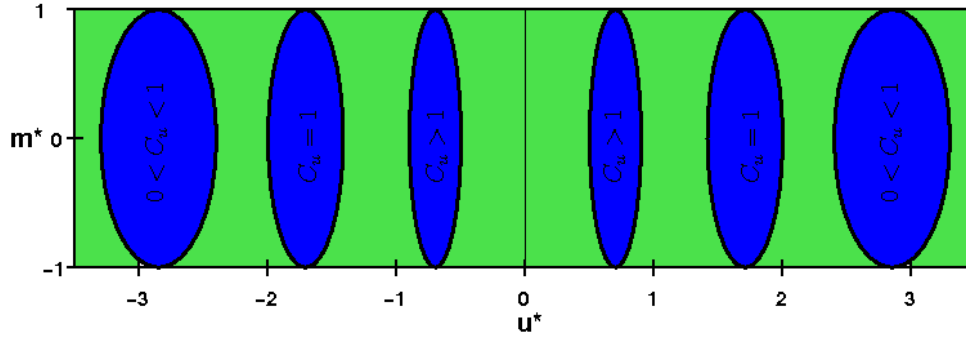


Figure 5.3: Hyperbolic region of the two-component uniform suspension system for different values of the momentum shape factor C_u

considered. Figure 5.3 shows the elliptic regions for a momentum shape factor chosen to be the same in both components $C_{1,u} = C_{2,u} = C_u$.

5.1.4 Eigenspeeds

In order to gain the eigenspeeds of the system, we have to back-transform the roots according to (5.2). Then the eigenvalues are of the form

$$\lambda_{1,2,3,4} = \frac{U_1 + U_2}{2} \pm \sqrt{\mathbf{c}^T \mathbf{m}} \cdot w(u^*, m^*) \quad (5.4)$$

with weights w , that depend only on u^* and m^* . They are given by absolute values of the roots $\eta_{1,2,3,4}$.

The first pair of eigenvalues is the one corresponding to $\eta_{1,2}$. It is referred to as the fast pair of eigenspeeds of the system. If we consider the case of vanishing slip, meaning $U_1 = U_2 = U$ and $u^* = 0$, this means

$$\lambda_{1,2} = U \pm \sqrt{\mathbf{c}^T \mathbf{m}}$$

Here, $\mathbf{c}^T \mathbf{m} = \varepsilon \cos \zeta h$ is nothing but the celerity of the shallow water theory written in dimensionless coordinates. Hence, the fast pair of eigenspeeds corresponds to the shallow water waves.

The second pair of eigenvalues $\lambda_{3,4}$ corresponding to $\eta_{3,4}$, is conditionally real arbitrary u^* and m^* . However for vanishing slip, that means

$$\lambda_{3,4} = U \pm \sqrt{\frac{1}{2} \mathbf{c}^T \mathbf{m}}$$

This pair of eigenvalues is referred to as the slow pair of eigenspeeds in the system. Later we will see, that these speeds are associated with the phase diffusion between the components.

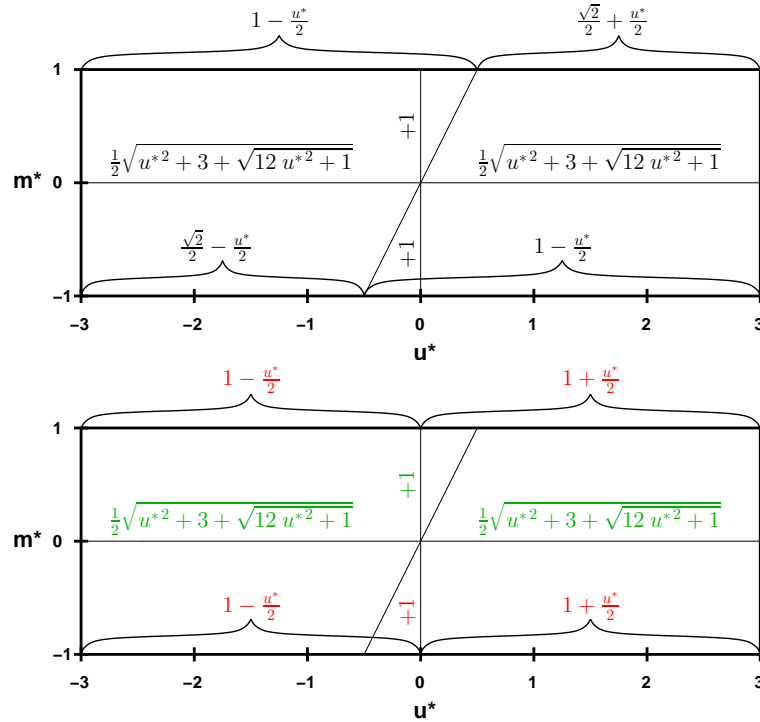


Figure 5.4: Upper picture: Celerity weights $w(u^*, m^*)$ for the exact fastest right-going eigenvalue. Lower picture: Approximated celerity weights $\tilde{w}(u^*, m^*)$ for the fastest right-going eigenvalue.

5.1.5 An approximation for the fast waves

A concluding paragraph within this section is devoted to an approximation for the fast pair of eigenspeeds. It will be essential in the formulation of a numerical solution scheme. As we saw, the eigenvalues are of the form $\frac{U_1 + U_2}{2} \pm \sqrt{\mathbf{c}^T \mathbf{m}} \cdot w(u^*, m^*)$, with $w(u^*, m^*)$ being a weighting factor for the shallow water celerity. The weighting factor is determined by the roots of the transformed characteristic polynomial p , thus simple solutions exist for $m^* \in \{-1, 0, 1\}$ and $u^* = 0$. Figure 5.4 shows the projected phase space twice. In the upper schematic, the exact celerities are given, in the lower one, two possible approximations $\tilde{w}(u^*, m^*)$ are suggested. Both assume, that the weighting factor is constant in m^* . The first approximation (green) relies on the first pair of roots of p for $m^* \equiv 0$. The second approximation (red) takes the maximum of the two exact solutions available for $m^* = \pm 1$ for every u^* . Formally, that means

$$\lambda_{1,2}^{(\text{first})} = \frac{(U_1 + U_2)}{2} + \sqrt{\mathbf{c}^T \mathbf{m}} \frac{1}{2} \sqrt{u^{*2} + 3 + \sqrt{12u^{*2} + 1}}$$

$$\lambda_{1,2}^{(\text{second})} = \frac{(U_1 + U_2)}{2} \pm \left(\sqrt{\mathbf{c}^T \mathbf{m}} + \frac{1}{2} |(U_1 - U_2)| \right)$$

In the upper picture of Figure 5.5, the weighting factor w for the fastest right-going eigenspeed is plotted as a function of u^* and m^* . In the lower plots first and second

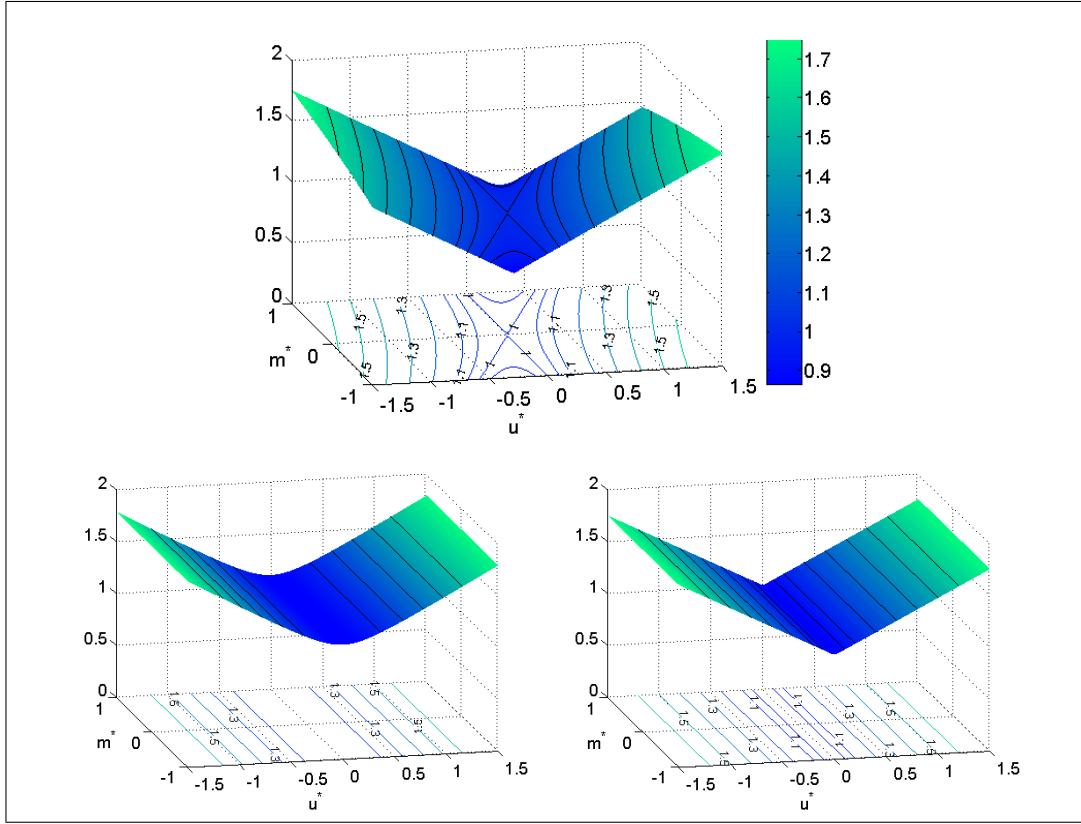


Figure 5.5: Upper picture: Exact weighting factor w for the fastest, right-going eigenspeed as a functions of m^* and u^* ; Lower left: First approximation to the weighting factor. Lower right: Second approximation to the weighting factor.

approximations are given. For the formulation of a numerical solution scheme, an approximation of the fastest left-going wave is necessary as well, and it is derived in a similar way.

5.2 Simplified Riemann problem

The uniform suspension limit of the multi-component shallow flow model is now simplified by neglecting the convective flux in the momentum equation. With $\mathbf{m} := (m_1, m_2)^T$ defined as before and $\mathbf{q} := (m_1 U_1, m_2 U_2)^T$ the system reads as

$$\partial_t \begin{pmatrix} \mathbf{m} \\ \mathbf{q} \end{pmatrix} + \partial_x \left(\frac{1}{2} (\mathbf{c}^T \mathbf{m}) \mathbf{m} \right) = \mathbf{0}$$

5.2.1 Hyperbolic structure

Let us define $\mathbf{M} := \frac{1}{2} ((\mathbf{c}^T \mathbf{m}) \mathbf{I} + \mathbf{m} \mathbf{c}^T)$. Then, the linearized system and characteristic polynomial of the simplified model are given by

$$\partial_t \begin{pmatrix} \mathbf{m} \\ \mathbf{q} \end{pmatrix} + \begin{pmatrix} \mathbf{0} & \mathbf{I} \\ \mathbf{M} & \mathbf{0} \end{pmatrix} \partial_x \begin{pmatrix} \mathbf{m} \\ \mathbf{q} \end{pmatrix} = \mathbf{0}$$

$$f(\lambda) = \det \begin{pmatrix} \lambda \mathbf{I} & -\mathbf{I} \\ -\mathbf{M} & \lambda \mathbf{I} \end{pmatrix} = \det(\lambda^2 \mathbf{I} - \mathbf{M}) = 0$$

The last equality indicates, that the roots of f correspond to the eigenvalues of \mathbf{M} . \mathbf{M} owes a first eigenvalue $\mathbf{c}^T \mathbf{m}$ corresponding to the eigenvector \mathbf{m} , and a second one $\frac{1}{2} \mathbf{c}^T \mathbf{m}$ corresponding to the eigenvector \mathbf{c}^\perp .

$$\begin{aligned} \mathbf{M} \mathbf{m} &= \frac{1}{2} ((\mathbf{c}^T \mathbf{m}) \mathbf{I} + \mathbf{m} \mathbf{c}^T) \mathbf{m} = (\mathbf{c}^T \mathbf{m}) \mathbf{m} \\ \mathbf{M} \mathbf{c}^\perp &= \frac{1}{2} ((\mathbf{c}^T \mathbf{m}) \mathbf{I} + \mathbf{m} \mathbf{c}^T) \mathbf{c}^\perp = \frac{1}{2} (\mathbf{c}^T \mathbf{m}) \mathbf{c}^\perp \end{aligned}$$

Finally, the eigenspeeds of the Jacobian itself are given by their roots. Together with the eigenvectors, we get

$$\begin{aligned} \lambda_{1,2} &= \pm \sqrt{\mathbf{c}^T \mathbf{m}} & \mathbf{e}_{1,2} &= \begin{pmatrix} \mathbf{m} \\ \pm \sqrt{\mathbf{c}^T \mathbf{m}} \mathbf{m} \end{pmatrix} \\ \lambda_{3,4} &= \pm \sqrt{\frac{1}{2} \mathbf{c}^T \mathbf{m}} & \mathbf{e}_{3,4} &= \begin{pmatrix} \mathbf{c}^\perp \\ \pm \sqrt{\frac{1}{2} \mathbf{c}^T \mathbf{m}} \mathbf{c}^\perp \end{pmatrix} \end{aligned}$$

Note again, that $\sqrt{\mathbf{c}^T \mathbf{m}}$ is the scaled celerity of the shallow water equations. Hence, like in the uniform suspension model, we have a fast and a slow pair of eigenspeeds. The fast one is associated with the shallow water waves itself, the second one with the phase diffusion process. Both pairs are positive and pairwise different within the physical domain of positive masses. Consequently, the system is strictly hyperbolic in that region.

5.2.2 Rankine Hugenoit jump conditions

Discontinuities have to satisfy the Rankine Hugenoit conditions. They are given by

$$\begin{aligned} s[\mathbf{m}] &= [\mathbf{q}] \\ s[\mathbf{q}] &= \left[\frac{1}{2} (\mathbf{c}^T \mathbf{m}) \mathbf{m} \right] \end{aligned}$$

Here, s is the propagation speed of the jump. Eliminating $[\mathbf{q}]$ gives

$$s^2[\mathbf{m}] = \left[\frac{1}{2} (\mathbf{c}^T \mathbf{m}) \mathbf{m} \right] \quad (5.5)$$

This statement holds also true for an arbitrary number of different components in the system. However, to analyze the jump conditions in detail, we will restrict ourselves to two components $i \in \{1, 2\}$ in the following. The phase states before and after the jump are denoted by the superscripts l and r respectively. Mass and momentum vectors are given by

$$\mathbf{m}^{(l)} := \begin{pmatrix} m_1^{(l)} \\ m_2^{(l)} \end{pmatrix} \quad \mathbf{m}^{(r)} := \begin{pmatrix} m_1^{(r)} \\ m_2^{(r)} \end{pmatrix} \quad \mathbf{q}^{(l)} := \begin{pmatrix} q_1^{(l)} \\ q_2^{(l)} \end{pmatrix} \quad \mathbf{q}^{(r)} := \begin{pmatrix} q_1^{(r)} \\ q_2^{(r)} \end{pmatrix}$$

and the jump conditions (5.5) transform into

$$s^2 (\mathbf{m}^{(r)} - \mathbf{m}^{(l)}) = \frac{1}{2} ((\mathbf{c}^T \mathbf{m}^{(r)}) \mathbf{m}^{(r)} - (\mathbf{c}^T \mathbf{m}^{(l)}) \mathbf{m}^{(l)}) \quad (5.6)$$

Component-wise, we get

$$\begin{aligned} s^2 - \frac{c}{2}(m_1^{(r)} + m_1^{(l)}) - \frac{c}{4}(m_2^{(r)} + m_2^{(l)}) + \frac{m_1^{(r)} + m_1^{(l)}}{m_1^{(r)} - m_1^{(l)}}(m_2^{(r)} - m_2^{(l)}) &= 0 \\ s^2 - \frac{c}{2}(m_2^{(r)} + m_2^{(l)}) - \frac{c}{4}(m_1^{(r)} + m_1^{(l)}) + \frac{m_2^{(r)} + m_2^{(l)}}{m_2^{(r)} - m_2^{(l)}}(m_1^{(r)} - m_1^{(l)}) &= 0 \end{aligned} \quad (5.7)$$

The left state $\mathbf{m}^{(l)}$ is initially prescribed, thus (5.7) provide two equations for the three unknowns s , $m_1^{(r)}$ and $m_2^{(r)}$. Hence, possible solutions are parametrized by one of the unknowns and the left phase state. In the following, we will discuss the two solution families.

5.2.3 Slow discontinuities

By substituting the pair of slow eigenspeeds $s = \pm \sqrt{\frac{1}{2} \mathbf{c}^T \mathbf{m}^{(l)}}$ of the left state $\mathbf{m}^{(l)}$ into (5.6), we immediately get

$$\begin{aligned} \frac{1}{2} (\mathbf{c}^T \mathbf{m}^{(l)}) \mathbf{m}^{(r)} - \frac{1}{2} (\mathbf{c}^T \mathbf{m}^{(l)}) \mathbf{m}^{(l)} &= \frac{1}{2} (\mathbf{c}^T \mathbf{m}^{(r)}) \mathbf{m}^{(r)} - \frac{1}{2} (\mathbf{c}^T \mathbf{m}^{(l)}) \mathbf{m}^{(l)} \\ \Rightarrow \mathbf{c}^T \mathbf{m}^{(r)} &= \mathbf{c}^T \mathbf{m}^{(l)} \end{aligned} \quad (5.8)$$

Let us define the visible heights for the left and the right state as $h^{(l)} := \frac{1}{c} (\mathbf{c}^T \mathbf{m}^{(l)})$ and $h^{(r)} := \frac{1}{c} (\mathbf{c}^T \mathbf{m}^{(r)})$. Then, from equation (5.8) we immediately see, that the visible height is constant across the corresponding jumps. Hence, for the slow discontinuity, it is sufficient to consider only one visible height $h := h^{(l)} = h^{(r)}$.

Across the jump, only the mass distribution is subject to change according to

$$m_1^{(r)} + m_2^{(r)} = h^{(r)} = h = h^{(l)} = m_1^{(l)} + m_2^{(l)} \quad (5.9)$$

Moreover, the jump speed is independent on the initial strength, thus it is a linear wave. A curve for the momenta of the single components is given by

$$\begin{aligned} q_1^{(r)} &= q_1^{(l)} \mp \sqrt{\frac{c}{2} h} (2m_1^{(l)} - h) \\ q_2^{(r)} &= q_2^{(l)} \mp \sqrt{\frac{c}{2} h} (2m_2^{(l)} - h) \end{aligned} \quad (5.10)$$

It is obvious, that the momenta change with the masses, but similar to the visible height, the bulk momentum $p^{(k)} := \mathbf{c}^T \mathbf{q}^{(k)}$, $k \in \{l, r\}$ is conserved across the discontinuity.

$$\begin{aligned} p^{(r)} = \mathbf{c}^T \mathbf{q}^{(r)} &= \mp \sqrt{\frac{c}{2} h} \underbrace{(2cm_1^{(l)} - ch + 2m_2^{(l)} - ch)}_{=0} + \mathbf{c}^T \mathbf{q}^{(l)} \\ &= \mathbf{c}^T \mathbf{q}^{(l)} = p^{(l)} = \text{const} \end{aligned} \quad (5.11)$$

5.2.4 Fast discontinuities

Multiplication of (5.5) with \mathbf{c}^T results in

$$\mathbf{c}^T s^2 [\mathbf{m}] = \mathbf{c}^T \left[\frac{1}{2} (\mathbf{c}^T \mathbf{m}) \mathbf{m} \right] \quad (5.12)$$

By making use of the previously defined visible heights $h^{(l)}$ and $h^{(r)}$ of the left and right states, we can immediately solve (5.12) for the propagating speed s for the fast discontinuity.

$$\begin{aligned} s^2 (\mathbf{c}^T \mathbf{m}^{(l)} - \mathbf{c}^T \mathbf{m}^{(r)}) &= \frac{1}{2} (\mathbf{c}^T \mathbf{m}^{(l)2} - \mathbf{c}^T \mathbf{m}^{(r)2}) \\ \Rightarrow s &= \pm \sqrt{\frac{c}{2} (h^{(l)} + h^{(r)})} \end{aligned} \quad (5.13)$$

For the bulk momenta, we derive

$$\begin{aligned} s \mathbf{c}^T [\mathbf{m}] &= \mathbf{c}^T [\mathbf{q}] \\ \Rightarrow s (ch^{(l)} - ch^{(r)}) &= p^{(l)} - p^{(r)} \end{aligned} \quad (5.14)$$

The curve determining the propagation of the fast discontinuity in the phase space is given by

$$s = \pm \sqrt{\frac{c}{2} (h^{(l)} + h^{(r)})} \quad p^{(r)} = p^{(l)} \pm c (h^{(l)} - h^{(r)}) \sqrt{\frac{c}{2} (h^{(l)} + h^{(r)})}$$

It is parametrized in $h^{(r)}$ and corresponds to the solution of the one-phase shallow water equations in the case of negligible convective flux. All in all, it is to say that the simplified system projected into the bulk quantities $h := \frac{1}{c} (\mathbf{c}^T \mathbf{m})$ and $p := \mathbf{c}^T \mathbf{q}$ conserves the same hyperbolic structure, than the shallow water equations. However in detail, that is in the single component variables, there exist additional waves, for which height and bulk momentum are invariant. In these waves only the single phases change.

5.3 Horizontal mixing of components

5.3.1 Depth-averaged slip

Let us consider the equations for small momentum exchange timescales τ in the absence of mass production rates and for negligible effective acceleration. By expanding the derivatives in the momentum equations and making additional use of the mass conservation, we derive

$$\begin{aligned} \partial_t U_1 + U_1 (\partial_x U_1) + \frac{1}{m_1} \partial_x \left(\varepsilon \cos \zeta \frac{m_1 + m_2}{2} m_1 \right) &= R_1 \\ \partial_t U_2 + U_2 (\partial_x U_2) + \frac{1}{m_2} \partial_x \left(\varepsilon \cos \zeta \frac{m_1 + m_2}{2} m_2 \right) &= R_2 \end{aligned} \quad (5.15)$$

$$R_1 = -\frac{m_2}{rm_1 + m_2} \frac{U_1 - U_2}{\tau} \quad R_2 = \frac{rm_1}{rm_1 + m_2} \frac{U_1 - U_2}{\tau}$$

Subtracting them from each other, results in an evolution equation for the velocity difference $D := U_1 - U_2$. Here, \bar{U} denotes the average velocity $\bar{U} := \frac{1}{2} (U_1 + U_2)$.

$$\begin{aligned} \partial_t D + \partial_x (D \bar{U}) &= \\ - \left(\frac{1}{m_1} \partial_x \left(\varepsilon \cos \zeta \frac{m_1 + m_2}{2} m_1 \right) + \frac{1}{m_2} \partial_x \left(\varepsilon \cos \zeta \frac{m_1 + m_2}{2} m_2 \right) \right) - \frac{D}{\tau} \end{aligned} \quad (5.16)$$

We now assume τ to be very small, which corresponds to a strong momentum exchange. Furthermore, let us write D as an asymptotic expansion in powers of τ .

$$D = D^{(0)} + \tau D^{(1)} + \mathcal{O}(\tau^2) \quad (5.17)$$

Substituting (5.17) into (5.16), and comparison to the lowest order results in an explicit equation for D .

$$m_1 m_2 D = \tau \left(m_2 \partial_x \left(\varepsilon \cos \zeta \frac{m_1 + m_2}{2} m_1 \right) + m_1 \partial_x \left(\varepsilon \cos \zeta \frac{m_1 + m_2}{2} m_2 \right) \right) \quad (5.18)$$

5.3.2 Phase diffusion

We also formulate the mass conservation for the first component in terms of the averaged velocity \bar{U} and get

$$\partial_t m_1 + \partial_x (m_1 \bar{U}) = -\partial_x \left(m_1 \frac{D}{2} \right) \quad (5.19)$$

Now, the explicit expression (5.18) for the depth-averaged slip velocity D is substituted in (5.19) and results in

$$\begin{aligned} \partial_t m_1 + \partial_x (m_1 \bar{U}) = \\ -\tau \partial_x \left(\frac{m_1}{2} \left(\partial_x \left(\varepsilon \cos \zeta \frac{m_1 + m_2}{2} m_1 \right) + \frac{m_1}{m_2} \partial_x \left(\varepsilon \cos \zeta \frac{m_1 + m_2}{2} m_2 \right) \right) \right) \end{aligned} \quad (5.20)$$

Hence, when following the average velocity of the flow, the first component is diffused according to the nonlinear right hand side of (5.20). To illuminate this further, we consider the two components to be approximately similar in their masses ($m_1 \approx m_2$). In that case, equation (5.20) reduces to

$$\partial_t m_1 + \partial_x (m_1 \bar{U}) = -\partial_x (C_{\text{diff}} \partial_x m_1) \quad (5.21)$$

with the nonlinear diffusion coefficient $C_{\text{diff}} := 2\tau\varepsilon \cos \zeta m_1^2$.

Chapter 6

A shallow flow model based on the theory of mixtures

The previous chapter was inspired by the work of Pitman and Le [68], in which the depth-integration of the system was performed on the single component equations. However, also the bulk mixture equations can be depth-averaged with respect to a varying vertical mass distribution as will be demonstrated in the following chapter.

The mixture theory for multi-component flow is a well-established approach. Very formative work done in the field is published in [55] and [5]. Iverson picked up this idea and depth-integrated the mixture equations under the assumption of constant volume fractions. We will demonstrate, that the same can be done for varying volume fractions. That results into a generalized version of Iverson's model accounting for vertical particle distributions. However, then the system is not closed any more, which implies the need of an additional equation for the vertical center of mass. We show, that an evolution equation for the center of mass is derived by depth-integrating the first moment of the bulk mass conservation. At the end of the chapter, the mixture model is compared to the single component model derived in the previous chapter.

6.1 Mixture theory

6.1.1 Single component equations

Let us consider a binary mixture of particles in a fluid, the two components being denoted by $i \in \{1, 2\}$. The single species mass and momentum balance laws have already been introduced in 4.1.

$$\begin{aligned}\partial_t \rho_i + \nabla \cdot (\rho_i \mathbf{u}_i) &= 0 \\ \partial_t (\rho_i \mathbf{u}_i) + \nabla \cdot (\rho_i \mathbf{u}_i \mathbf{u}_i) &= \nabla \cdot \sigma_i + \rho_i \mathbf{g} + I_i\end{aligned}\tag{6.1}$$

6.1.2 Bulk formulation

A common way to formulate balance laws for the whole mixture is by defining the bulk density ρ , the mass fractions c_i , the barycentric velocity \mathbf{u} and the bulk stress σ according to

$$\rho := \sum \rho_i \quad \mathbf{c}_i := \frac{\rho_i}{\rho} \quad \mathbf{u} := \sum_i c_i \mathbf{u}_i \quad \sigma := \sum_i \sigma_i$$

In a next step, the single component's balance laws are summed up. Furthermore, we restrict ourselves to the case of a binary mixture. Then relative velocity \mathbf{d} between the components, also called the slip velocity, is defined according to

$$\mathbf{d} := \mathbf{u}_1 - \mathbf{u}_2 \tag{6.2}$$

The slip \mathbf{d} is assumed to be small, such that any square term in it may be neglected. Mass and momentum balance for the bulk mixture then result into

$$\begin{aligned} \partial_t \rho + \nabla \cdot (\rho \mathbf{u}) &= 0 \\ \partial_t (\rho \mathbf{u}) + \nabla \cdot (\rho \mathbf{u} \mathbf{u}) &= \nabla \cdot \sigma + \rho \mathbf{g} \end{aligned} \tag{6.3}$$

The assumption of constant volume fractions, that forms the basis of Iverson's model [44], implies constant bulk density ρ . In that case, the mixture system (6.3) formally reduces to the one-phase balance laws (3.1). The difference to a model for one homogeneous material however is, that the stress tensor has (fixed) contributions from both components.

It is important to mention, that in flow situations, in which the local bulk density is subject to change (segregation, sedimentation, re-suspension ...), the velocity field \mathbf{u} is not divergence free. We saw in Chapter 4), that the latter property is only true for the volume-averaged velocity field \mathbf{u}_v (compare (4.6)). However, writing the system in terms of \mathbf{u}_v gives rise to additional diffusive source terms, although an effective mass production is not present.

6.1.3 First species mass conservation

The bulk system (6.3) is completed by the first species mass conservation equation, written in terms of the barycentric velocity. An equation of the latter form is necessary, to track the varying composition of the flow.

$$\partial_t \rho_1 + \nabla \cdot (\mathbf{u} \rho_1) = -\nabla \cdot \left(\mathbf{d} \frac{\rho_1 \rho_2}{\rho} \right) \tag{6.4}$$

Note, that in Iverson's derivation, an equation of the form (6.4) would have been redundant, and hence does not appear.

6.2 Slip velocity

We consider square terms in the slip \mathbf{d} to be negligible, but want to keep first order terms in the system. However, we still assume \mathbf{d} to be small, such that it is reasonable write the momentum exchange as viscous drag.

$$I_2 = -I_1 = \frac{\rho_1 \rho_2}{\rho} \frac{\mathbf{d}}{\tau} \quad (6.5)$$

Here, τ is some characteristic relaxation timescale, that may depend on the concentration, the shape of the flow, etc.. By substituting this expression into the momentum equations of the system (6.1), the following evolution equation for the slip velocity is derived.

$$\partial_t \mathbf{d} + \mathbf{d} \cdot \nabla \mathbf{u} + \mathbf{u} \cdot \nabla \mathbf{d} = -\frac{1}{\rho_1} \nabla \cdot \sigma_1 + \frac{1}{\rho_2} \nabla \cdot \sigma_2 - \frac{\mathbf{d}}{\tau} \quad (6.6)$$

Within the considered flow regimes, the momentum exchange happens almost instantaneously, such that the relaxation timescale τ is very small, i.e. $\tau \ll 1$. Thus, \mathbf{d} can be written as an asymptotic expansion in powers of τ .

$$\mathbf{d} = \mathbf{d}^{(0)} + \tau \mathbf{d}^{(1)} + \mathcal{O}(\tau^2) \quad (6.7)$$

Comparison to the lowest order corresponds to instantaneous relaxation and results into an explicit equation for \mathbf{d}

$$\frac{\mathbf{d}}{\tau} = \frac{1}{\rho_2} \nabla \cdot \sigma_2 - \frac{1}{\rho_1} \nabla \cdot \sigma_1 \quad (6.8)$$

The single species stresses σ_i are written as a proportion of the bulk stress, the coefficient ϕ_i being the volume fraction.

$$\nabla \cdot \sigma_i = \nabla \cdot \phi_i \sigma = \phi_i \nabla \cdot \sigma + \sigma \nabla \phi_i \quad (6.9)$$

Here, the first term accounts for the buoyancy and the second gives rise to dispersion of the species. This is a common way of defining the single stress components in a mixture (compare Drew [29]).

With the latter considerations on the slip, and by making use of the saturation property $\sum_i \phi_i = 1$, $\sum_i c_i = 1$, the first species mass conservation (6.4) transforms into

$$\partial_t \rho_1 + \nabla \cdot (\mathbf{u} \rho_1) = \nabla \cdot (\tau(c_1 - \phi_1) \nabla \cdot \sigma) + \nabla \cdot (\tau \sigma \nabla \phi_1)$$

It accounts for change in the material composition within the flow, when moving with the centre-of-mass velocity.

6.3 Evolution of the concentration

The latter evolution equation is written in terms of the concentration c_1 .

$$\partial_t c_1 + \mathbf{u} \cdot \nabla c_1 = \frac{1}{\rho} \nabla \cdot (\tau(c_1 - \phi_1) \nabla \cdot \sigma) + \frac{1}{\rho} \nabla \cdot (\tau \sigma \nabla \phi_1) \quad (6.10)$$

As mentioned earlier, the additional consideration of an extra concentration equation is new in comparison to other debris flow models based on mixture theory.

In the following, we briefly comment on the two source terms.

6.3.1 Sedimentation

Let us consider pressure to be the main stress, and furthermore assume a state of approximate hydrostatic equilibrium. Then the gradient of the stress tensor reduces to

$$\nabla \sigma = \nabla p = \mathbf{g} \rho \quad (6.11)$$

In Section 4.8.5, we discussed several concepts to describe sedimentation in a highly-concentrated suspension. Here, we will again use the basic hindered settling concept proposed by Kynch [56].

The particles (component 1) settle with the velocity \mathbf{u}_1 , defined according to

$$\mathbf{u}_1 = (1 - \phi_1) \mathbf{u}_{st} = \phi_2 \mathbf{u}_{st} \quad (6.12)$$

Here \mathbf{u}_{st} denotes a final sedimentation velocity given by the product of the momentum exchange time scale τ and the gravitational acceleration $\mathbf{u}_{st} = \tau \mathbf{g}$. For small horizontal slip, we can make use of the divergence-free volume-averaged velocity field, and derive

$$\tau(c_1\phi_2 - c_2\phi_1)\nabla p = \Delta\rho\phi_1\phi_2\mathbf{u}_{st} \quad (6.13)$$

Here, $\Delta\rho$ denotes the density difference of the two components, such that there will be no change in concentration, when either one of the components occupies the full space, or there is no difference in their densities. Also the concentration will not be influenced, if the volume concentrations are constant.

6.3.2 Phase diffusion

The second source term in the concentration equation (6.10) determines phase diffusion. By defining the diffusion coefficient $D := \frac{\tau p}{\rho_{1,0}}$, the second term reduces to $\nabla \cdot (D\nabla\rho_1)$, and the interpretation as inter-component diffusion becomes even more obvious.

A final version of the concentration equation is written as

$$\partial_t c_1 + (\mathbf{u} \cdot \nabla) c_1 = \frac{\Delta\rho}{\rho} \nabla \cdot (\phi_1\phi_2\mathbf{u}_{st}) - \frac{1}{\rho} \nabla \cdot (D\nabla\rho_1) \quad (6.14)$$

6.4 Depth-Integration

The process of depth-integration is performed along the lines of the previous two chapters. That is why a detailed description will be omitted and only the main results are given.

In addition to the depth-integrated quantities m_i , U_i and h , introduced in Chapter 4, let us consider the following bulk depth-averaged variables.

$$\begin{aligned} m &:= m_1 + m_2 & c &:= \frac{m_1}{m} \\ U &:= cU_1 + (1-c)U_2 & h^{(cm)} &:= \frac{1}{m} \int z\rho dz \end{aligned}$$

The bulk mass per unit area is denoted by m , c stands for the depth-averaged concentration of the first component, U for the depth-averaged barycentric velocity, and $h^{(cm)}$ indicates the vertical center of the bulk mass. It should be noted, that although here, c and U are defined in terms of the depth-averaged single-component variables, their definition is consistent with the density weighted formulation. Thus, by making use of $\langle \cdot \rangle := \frac{\int \cdot \rho dz}{\int \rho dz}$, we get the equivalent formulations

$$m = \int \rho dz \quad c = \langle c_1 \rangle \quad U = \langle u \rangle \quad h^{(cm)} = \langle z \rangle$$

6.4.1 Mass- and Momentum equation

Depth-averaged mass conservation and momentum balance result into

$$\begin{aligned} \partial_t m + \partial_x(Um) &= 0 \\ \partial_t(Um) + \partial_x(C_u U^2 m + \cos \zeta h^{(cm)} m) &= m \sin \zeta - \frac{U}{\|U\|} F[c, h^{(cm)}, m, U] \end{aligned} \quad (6.15)$$

Here $F[c, h^{(cm)}, m, U]$ stands for a general friction relation, and will be closed later.

6.4.2 Concentration equation

An evolution equation for the depth-averaged concentration of the first component c is derived by depth-integrating the associated first species mass conservation.

$$\partial_t(cm) + \partial_x(C_c cmU) = \int_b^s \text{Mixing } dz \quad (6.16)$$

$C_c := \frac{\langle c_1 u \rangle}{\langle c_1 \rangle \langle u \rangle}$ is a concentration shape factor. Due to linearity of $\langle \cdot \rangle$, we immediately see, that for either constant vertical concentration or constant velocity profile, there holds $C_c = 1$. Also in more general, yet relevant situations, this choice is appropriate. The integral on the right hand side involves the previously discussed mixing terms, including sedimentation and phase diffusion.

$$\int_b^s \text{Mixing } dz = \int_b^s (\Delta \rho \nabla \cdot (\phi_1 \phi_2 \mathbf{u}_{st}) - \nabla \cdot (D \nabla \rho_1)) dz \quad (6.17)$$

Integrated sedimentation

For a small inclination, the sedimentation does not affect the depth-averaged concentration, such that the first term simply vanishes. However, it does play a role for big inclination angles ζ , since then z -axis of the inclined coordinate system varies significantly from the settling direction. Within this derivation, we will consider ζ to be reasonably small, such that neglecting the depth-averaged sedimentation is justified.

$$\int_b^s \Delta \rho \nabla \cdot (\phi_1 \phi_2 \mathbf{u}_{st}) dz = 0 \quad (6.18)$$

Integrated diffusive term

In the diffusive term, the x -component is the dominating one. By making use of the previously defined diffusion constant D , we observe

$$\int_0^\infty \nabla \cdot (D \nabla \alpha_1) dz = \partial_x \left(\tilde{D} \partial_x (cm) \right) \quad (6.19)$$

with a modified \tilde{D} , that accounts for coefficients arising in the depth integration. We drop the tilde in the following. Substituting (6.19) into (6.16) and setting the concentration shape factor to one, we get

$$\partial_t (cm) + \partial_x (cmU) = \partial_x (D \partial_x (cm)) \quad (6.20)$$

6.4.3 Vertical center of mass

To close (6.15), we formulate an additional equation for the vertical centre of mass $h^{(cm)}$. At first the bulk mass conservation is multiplied by z , and can be interpreted as the first moment of the mass equation.

$$\partial_t (z\rho) + \partial_x (z\rho U) = -z \partial_z (v\rho) \quad (6.21)$$

The depth-average of the left hand side is evaluated in a straight-forward manner, and the appearing shape factor is once again set to one. The right hand side is simplified by performing integration by parts.

$$\partial_t (h^{(cm)} m) + \partial_x (h^{(cm)} m U) = \int_b^s v \rho dz \quad (6.22)$$

Here, the product $h^{(cm)} m$ denotes the depth-integrated gravitational potential energy. The key issue now is, to close for the barycentric vertical velocity v . It is subject to change by two different physical processes:

- Vertical velocity v_f due to horizontal bulk mass flow
- Vertical velocity v_r due to internal redistribution of the components
(sedimentation and re-suspension)

Let us consider the effective v to be a superposition of both, such that

$$v = v_f + v_r \quad (6.23)$$

Horizontal mass flow

If the internal distribution of components is constant $v_r = 0$, v_f evaluated at the top is given by the height change of the free surface. At the bottom, v_f is zero and in between, we use a linear interpolation of both values:

$$v_f = \frac{z}{h} \frac{D}{Dt} h$$

Here $\frac{D}{Dt}$ denotes the material derivative. Then, the depth-integrated first moment reduces to a conservation equation for the height of the vertical center of mass.

$$\partial_t h^{(cm)} + \partial_x (h^{(cm)} U) = 0$$

Internal redistribution

v_r describes any change of the vertical center of mass due to sedimentation and resuspension. In the following, we propose a simplifying framework, that allows for an explicit solution of (6.22). It corresponds to the assumptions, that we used in the combined approach in the previous Chapter 4.8. We assume, that in an upper layer particles are uniformly suspended. It is referred to as the suspension layer. In a lower layer particles are completely settled to the ground and form a settled layer. The two layers are separated by the sedimentation line k .

In the settled layer, we have $v_r = 0$ and the right hand side of (6.22) reduces to the evaluation of the integral in the suspension layer.

$$\int_b^s v \rho dz = \int_k^s v \rho dz \quad (6.24)$$

In the suspension layer, no bulk density gradient is present. Then due to the conservation of mass, concentration c_i and volume fraction ϕ_i will be functions of k . Evaluating them in the suspension layer (denoted by the superscript (s)) results in

$$\begin{aligned} \phi_1^{(s)} &= \frac{h_1 - k}{h - k} & \phi_2^{(s)} &= \frac{h_2}{h - k} \\ c_1^{(s)} &= \frac{(h_1 - k)\rho_{1,0}}{(h_1 - k)\rho_{1,0} + h_2\rho_{2,0}} & c_2^{(s)} &= \frac{h_2\rho_{1,0}}{(h_1 - k)\rho_{1,0} + h_2\rho_{2,0}} \end{aligned}$$

Using the hindered settling velocity according to Kynch (4.45), now v_r given as a function of the height of the sedimentation line k

$$v_r = \begin{cases} 0 & \text{for } 0 \leq z < k \\ \left(c_1^{(s)} - \phi_1^{(s)} \right) u_{st} & \text{for } k \leq z \leq s \end{cases}$$

Now, we can completely evaluate the integral and obtain

$$\int_b^s v_r \rho dz = \int_k^s v_r \rho^{(s)} dz = \frac{h_2(h_1 - k)}{k - k} u_{st} \Delta \rho \quad (6.25)$$

If the whole bulk is uniformly mixed in vertical direction, there holds $k = 0$ and the sedimentation rate corresponds to $\frac{h_2 h_1}{h} u_{st} \Delta \rho$. In the stationary, settled limit however, there holds $k = h_1$ and the term vanishes. We also have a zero right hand side, if the densities of both components coincide, such that $\Delta \rho = 0$.

A short calculation yields the sedimentation line k as a function of $h^{(cm)}$.

$$k = \frac{h - 2h^{(cm)}}{h_2 \Delta \rho} m \quad (6.26)$$

The latter expression degenerates, if the components densities coincide ($\Delta \rho = 0$), or the second component vanishes ($h_2 = 0$). In both cases, an evaluation of changes in the vertical centre of mass are irrelevant.

The final version of the evolution equation for the vertical centre of mass $h^{(cm)}$, is written as

$$\partial_t h^{(cm)} + \partial_x (h^{(cm)} U) = \frac{1}{m} \frac{h_2 (h_1 - k)}{h - k} u_{st} \Delta \rho \quad (6.27)$$

6.5 Summarized formulation

Basal friction

Any information on the amount of settled particles is now coded in the height of the sedimentation line k . Let us consider, that the basal friction is composed of two part. One being due to the suspension $F_{sus}[c, h^{(cm)}, m, U]$, and the other being due to the settled layer $F_{sed}[c, h^{(cm)}, m, U]$. As a first attempt, we choose it to be

$$\begin{aligned} F[c, h^{(cm)}, m, U] &= \frac{k}{h_1} F_{sed}[c, h^{(cm)}, m, U] + \frac{h_1 - k}{h_1} F_{sus}[c, h^{(cm)}, m, U] \\ &= \frac{k}{h_1} m \cos \zeta \mu_{sed} + \frac{h_1 - k}{h_1} (m \cos \zeta \mu_{sus} + \xi_{sus} U^2) \end{aligned}$$

Summarized Model

Then, the summarized system is given by

$$\partial_t \begin{bmatrix} m \\ cm \\ mU \\ h^{(cm)} \end{bmatrix} + \partial_x \begin{bmatrix} mU \\ cmU \\ mU^2 + \cos \zeta h^{(cm)} m \\ h^{(cm)} U \end{bmatrix} = \begin{bmatrix} 0 \\ -D \partial_x^2 (cm) \\ S \\ \frac{1}{m} \frac{h_2 (h_1 - k)}{h - k} u_{st} \Delta \rho \end{bmatrix} \quad (6.28)$$

$$S := \underbrace{m_2 \sin \zeta}_{\text{acceleration}} - \frac{U}{\|U\|} \left(\underbrace{\frac{k}{h_1} m \cos \zeta \mu_{sed}}_{\text{friction due to the settled particles}} + \underbrace{\frac{h_1 - k}{h_1} (m \cos \zeta \mu_{sus} + \xi_{sus} U^2)}_{\text{friction due to the suspension layer}} \right)$$

Note, that we implicitly included that the diffusion coefficient D is constant in x , and moreover the momentum shape factor C_u is set to one. If the whole body is in uniform suspension, or the densities of both materials coincide, then $h^{(cm)} \equiv \frac{h}{2}$ and the evolution equation for the vertical centre of mass is superfluous. Still it is necessary to evaluate the concentration equation, since the visible height h , is a function of m and c .

$$h = \left(\frac{1}{\rho_{2,0}} - \frac{\Delta \rho}{\rho_{1,0} \rho_{2,0}} c \right) m \quad (6.29)$$

The fact, that the visible height is a function of c and m , i.e. $h = h(c, m)$, makes obvious, that the momentum equation of the system is coupled to all three of the other evolution equations.

6.6 Hyperbolic properties

The Jacobian of the flux function with respect to the set of conserved quantities $\mathbf{V} := [m, cm, Um, h^{(cm)}]^T$ is given by

$$DF(\mathbf{V}) := \begin{bmatrix} 0 & 0 & 1 & 0 \\ -cU & U & c & 0 \\ -U^2 + \cos \zeta h^{(cm)} & 0 & 2U & \cos \zeta m \\ -\frac{h^{(cm)}}{m} U & 0 & \frac{h^{(cm)}}{m} & U \end{bmatrix}$$

with the height h as in (6.29). The character of the system is determined by the eigenvalues of $DF(\mathbf{V})$, which are computed to be

$$\lambda_{1,2} = U \pm \sqrt{2h^{(cm)} \cos \zeta} \quad \lambda_{3,4} = U \quad (6.30)$$

Hence, the system is strictly hyperbolic in the physical domain of positive heights $h > 0$ and linearly degenerate for zero heights. Like one would expect, the eigenspeeds of the suggested mixture model reduces to the shallow water eigenspeeds for the case of one single homogeneous component, because then we have $h^{(cm)} = \frac{h}{2}$.

6.7 Pure sedimentation and basal fluid pressure

Similar to the combined approach in Chapter 4, the proposed mixture model is formulated in a shallow flow framework. However, we have shown, that it still allows for change in

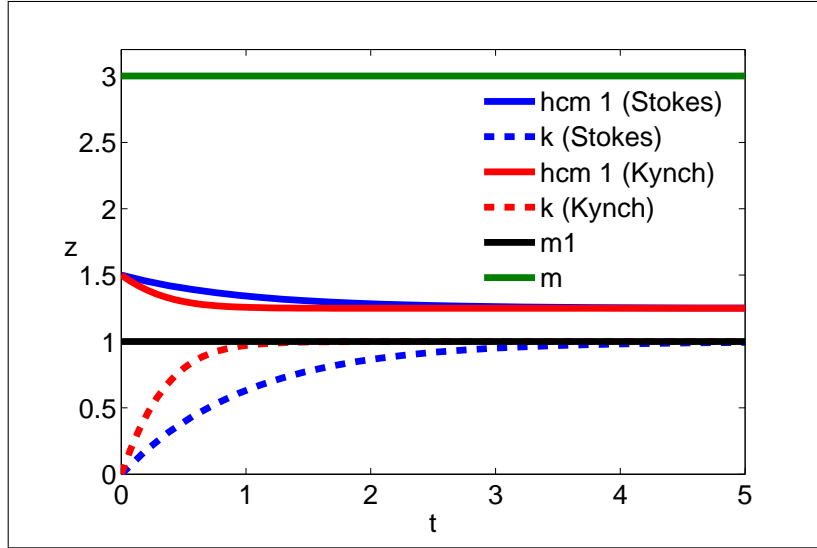


Figure 6.1: Sedimentation in the multi-phase mixture formulation: The drawn through, upper lines described the decrease in the vertical centre of mass for standard Stokes settling (blue) and the hindered settling velocity proposed by Kynch (red). The dashed, lower lines show the corresponding increase of the sedimentation line.

the vertical structure. In the absence of horizontal flow velocity $U = 0$ and any gradients in x -direction, the depth-integrated concentration c is constant, and the only dynamics we are left with is sedimentation. Because in that situation, we also get $\partial_t m = \partial_t c = U = 0$, the full system reduces to

$$\frac{d}{dt} h^{(cm)} = \frac{1}{m} \frac{h_2(h_1 - k)}{h - k} u_{st} \Delta \rho \quad (6.31)$$

Note, that k is defined according to (6.26). Starting from a vertically uniform suspension $h^{(cm)} = \frac{h}{2}$, the evolution of the vertical center of mass is determined by (6.31). Figure 6.1 shows the numerical approximation of the decay in the vertical center of mass, as well as the location of the sedimentation line as a function of time. The red curves correspond to the Kynch hindered settling velocity, the blue ones to a constant Stokes settling velocity.

6.8 Relevance of the depth-averaged mixture model

In a final section, we want to discuss the relevance of the new mixture model. Similar to the single component model, it allows for sedimentation and re-suspension of particles. However, by formulating a bulk momentum equation, one loses information about the single component velocities. In contrast to the single component model, the mixture approach is fully hyperbolic, and as such well-posed.

For a uniform suspension throughout the flow and in the absence of any sedimentation

and re-suspension rates, no sedimentation line is present and this system is a simple variation of Iverson's model.

The comparison of the theoretical results with actually measured data is subject of future work. However, it should be noted, that to do so, we still have to connect the system variables to the basal fluid pressure \mathbf{P}_{eff} . Let us consider enough voids in the settled layer, to maintain the hydrostatic fluid pressure, a short calculation results in

$$\mathbf{P}_{\text{eff}} = g (k\rho_{1,0} + (h - k) \rho^{(s)}) \quad (6.32)$$

Chapter 7

Numerical solution of the suspension model

The last two chapters were devoted to a comprehensive discussion of the modeling possibilities to carry over a varying vertical distribution of components into a multi-phase shallow flow model. The major concern of this chapter is the development of an appropriate numerical solver. Various authors worked on the formulation of numerical methods for the two-layer model [1, 12, 67]. A numerical scheme for the mixture model can be realized by a simple extension to existing codes for the shallow water equations.

The focus of this chapter is on a scheme for the uniform suspension model in a simple framework. Simple refers to the fact, that we neglect any variation in the topography $\partial_x b = 0$, and entrainment and deposition rates are set to zero. The basal friction is given by Coulomb friction with friction coefficients μ_1 and μ_2 in the two components. The model then consists of three contributing parts, referred to as the homogeneous flux $\mathbf{F}(\mathbf{V})$, the momentum exchange $\mathbf{R}(\mathbf{V})$ and accelerating and frictional forces $\mathbf{G}(\mathbf{V})$:

$$\partial_t \mathbf{V} + \partial_x \mathbf{F}(\mathbf{V}) = \mathbf{G}(\mathbf{V}) + \mathbf{R}(\mathbf{V}) \quad (7.1)$$

$$\mathbf{V} := \begin{pmatrix} m_1 \\ m_2 \\ m_1 U_1 \\ m_2 U_2 \end{pmatrix} \quad \mathbf{F}(\mathbf{V}) := \begin{pmatrix} m_1 U_1 \\ m_2 U_2 \\ m_1 U_1^2 + \frac{1}{2} (\mathbf{c}^T \mathbf{m}) m_1 \\ m_2 U_2^2 + \frac{1}{2} (\mathbf{c}^T \mathbf{m}) m_2 \end{pmatrix} \quad \mathbf{G}(\mathbf{V}) := \begin{pmatrix} 0 \\ 0 \\ G_1 \\ G_2 \end{pmatrix} \quad \mathbf{I}(\mathbf{V}) := \begin{pmatrix} 0 \\ 0 \\ R_1 \\ R_2 \end{pmatrix}$$

$$\begin{aligned} G_1 &:= m_1 \left(\sin \zeta - \frac{U_1}{\|U_1\|} \mu \cos \zeta \right) & R_1 &:= \frac{1}{\tau} \frac{m_1 m_2}{r m_1 + m_2} (U_1 - U_2) \\ G_2 &:= m_2 \left(\sin \zeta - \frac{U_2}{\|U_2\|} \mu \cos \zeta \right) & R_2 &:= -\frac{1}{\tau} \frac{r m_1 m_2}{r m_1 + m_2} (U_1 - U_2) \end{aligned}$$

The aim of the first section is, to introduce general concepts and corresponding notation associated with finite volume methods, as far as they are necessary for the ongoing of

this thesis. After that, step-wise a numerical scheme to solve the model is developed. Special effort is put on an alleviation of the problems associated with the breakdown of hyperbolicity for big slip velocities. However, we will demonstrate, that relaxation will keep the system away from ellipticity. It should also be noted, that modeling geophysical flows in real terrain always includes the additional difficulty of a complex basal topography. An outlook into the latter topic will be given in the last chapter.

7.1 General framework

The basic idea of the finite volume approach is to discretize the computational domain into small control volumes and change to an integral formulation of the system. By means of the Gauss' theorem, divergence terms can be converted into surface integrals. The numerical approximation can now be interpreted as the rate of exchange of one control volume with its adjacent cells per time step. Hence, it directly reflects the original physical meaning of the model system. Major advantages of the finite volume method are: (1) Due to the integral representation of the equations, it allows for discontinuous solutions, which are likely to be present in hyperbolic systems. (2) Finite volume methods do not require a structured mesh in general.

7.1.1 Hyperbolic systems

For the spatial dimension d and the dimension of the phase space m , let $\Omega \subseteq \mathbb{R}^d$ and $\mathcal{X} \subseteq \mathbb{R}^m$ be open sets and $\mathbf{F}, \mathbf{S} : \mathcal{X} \rightarrow \mathbb{R}^m$ be smooth functions. Then a balance law in d space dimensions is a system of first order partial differential equations of the form

$$\begin{aligned} \partial_t \mathbf{V}(\mathbf{x}, t) + \nabla \cdot \mathbf{F}(\mathbf{V}(\mathbf{x}, t)) &= \mathbf{S}(\mathbf{V}(\mathbf{x}, t)) \\ (\mathbf{x}, t) &\in \Omega \times \mathbb{R}^+ \end{aligned} \quad (7.2)$$

Here, $\mathbf{V} : \Omega \times \mathbb{R}^+ \rightarrow \mathcal{X} \subset \mathbb{R}^m$ denotes a vector field, the entries of $\mathbf{V}(\mathbf{x}, t)$ are called the state variables and $\mathbf{F}(\cdot)$ is called the flux.

Conservation laws

For $\mathbf{S} \equiv \mathbf{0}$, the system is called homogeneous and the balance law turns into a conservation law. The state variables are then referred to as conserved quantities. This property is seen best, when integrating the homogeneous system over an arbitrary (but constant in time) subset $\mathcal{C} \subset \mathbb{R}^d$ and applying Gauss' theorem.

$$\frac{d}{dt} \int_{\mathcal{C}} \mathbf{V} \, d\mathbf{x} = - \oint_{\partial \mathcal{C}} \mathbf{F}(\mathbf{V}) \cdot \mathbf{n} \, d\sigma \quad (7.3)$$

Here, \mathbf{n} denotes the outward pointing unit normal of \mathcal{C} . If \mathbf{V} was a concentration, the

integral of \mathbf{V} over \mathcal{C} represents the total mass in that volume. This mass is changed only due to in- and outflow through the surface.

Initial value problems

At time $t = 0$ the state variables have a particular configuration and the goal is to compute them forward in time. This problem, given by a balance law, together with an initial data set is called a **Cauchy problem**.

$$\begin{aligned} \partial_t \mathbf{V}(\mathbf{x}, t) + \nabla \cdot \mathbf{F}(\mathbf{V}(\mathbf{x}, t)) &= \mathbf{S}(\mathbf{V}(\mathbf{x}, t)) \\ \mathbf{V}(\mathbf{x}, 0) &= \mathbf{V}_0(\mathbf{x}) \end{aligned} \tag{7.4}$$

A one-dimensional Cauchy problem of a conservation law with piecewise constant initial data, that exhibits a single discontinuity at $\mathbf{x} = x = 0$ is called a **Riemann problem**.

$$\mathbf{V}_0(x) = \begin{cases} \mathbf{V}_L & \text{if } x \geq 0 \\ \mathbf{V}_R & \text{if } x < 0 \end{cases}$$

A function $\mathbf{V} \in C^1(\Omega \times \mathbb{R}^+; \mathcal{X})$ is called a classical solution of (7.2), if it satisfies the balance law at every point of its domain. However, working with hyperbolic systems often means dealing with discontinuities, which may appear, disappear, or split on the different components of the state variables. In this context, a discontinuity is also called a **shock** and the appropriate solution concept is given by the weak solution. A function $\mathbf{V} \in L_1(\Omega \times \mathbb{R}^+; \mathcal{X})$ is called a weak solution of (7.2), if it satisfies the integral formulation at every point of its domain. Obviously every classical solution is a weak solution and every weak C^1 solution is a classical solution. When we speak of a solution in the ongoing of this thesis, this in general we refers to a weak solutions.

7.1.2 Finite volume formulation

Discretization

The 1D computations are performed on structured discretization of the bounded interval $[x_0, x_n] \subset \mathbb{R}$, given by the grid $[x_0, x_1, \dots, x_{n-1}, x_n]$ with equidistant grid size $\Delta x := x_i - x_{i-1}, i \in \{1, \dots, n\}$.

The 2D computations are done on a structured discretization of the bounded domain $\mathcal{C} := [x_0, x_n] \times [y_0, y_m] \subset \mathbb{R}^2$. The equidistant grid size in x -direction is given by $\Delta x := x_j - x_{j-1}, j \in \{1, \dots, m\}$, and in y -direction by $\Delta y := y_k - y_{k-1}, k \in \{1, \dots, m\}$ respectively.

In both, one and two dimensions, the cells, also referred to as control volumes, are denoted by $\mathcal{C}_{(i)}$. The length/area of the cells is denoted by $|\mathcal{C}_{(i)}|$ and the outward pointing unit

normals are given by $n_{(i,k)}$. k is only relevant in more than one dimension, as it accounts for the different cell interfaces.

The discrete time levels are denoted by $\{t^{(0)}, t^{(1)}, \dots\}$. However, the time steps will have to fulfill certain stability requirements, such that $t^n - t^{n-1}$ is not constant in general.

Finite volume formulation

Integration of the balance law (7.2) over the control volume $\mathcal{C}_{(i)}$ results in

$$\int_{\mathcal{C}_{(i)}} \partial_t \mathbf{V} \, d\mathbf{x} + \oint_{\partial \mathcal{C}_{(i)}} \mathbf{F}(\mathbf{V}) \cdot n_{(i)} \, d\sigma = \int_{\mathcal{C}_{(i)}} \mathbf{S}(\mathbf{V}) \, d\mathbf{x} \quad (7.5)$$

Averaged quantities for the phase variables are stored at the center of each cell. They are defined according to

$$\mathbf{V}_i := \frac{1}{|\mathcal{C}_{(i)}|} \int_{\mathcal{C}_{(i)}} \mathbf{V} \, d\mathbf{x} \quad (7.6)$$

The cells $\mathcal{C}_{(i)}$ are constant in time, such that with the previous definition the integral formulation (7.5) is written as

$$\frac{d}{dt} \mathbf{V}_i = - \oint_{\partial \mathcal{C}_{(i)}} \mathbf{F}(\mathbf{V}) \cdot n_{(i)} \, d\sigma + \int_{\mathcal{C}_{(i)}} \mathbf{S}(\mathbf{V}) \, d\mathbf{x} \quad (7.7)$$

To formulate a numerical scheme, one now has to (1) discretize the line integral or surface flux by means of a numerical flux function, (2) evaluate the volume integral accounting for the source terms and (3) discretize the time-ordinary differential equation.

Harten-Lax-van Leer scheme

Within this thesis, the discretization of the surface integral is based on the HLL flux [30, 36]. To guarantee second order convergence in space and time, a linear reconstruction of the averaged, conserved cell quantities is applied. The time-integration is given by a Runge-Kutta Heun scheme [58]. The cell-averaged quantities of the state variables on a time-discrete level are denoted by $\mathbf{V}_i^{(n)}$, and $\mathbf{V}^{(n)}$ stands for the whole grid function on time level $t^{(n)}$. Then a one-dimensional formulation of the scheme is given by

$$\begin{aligned} \mathbf{V}_i^{(*)} &= \mathbf{V}_i^{(n)} + \frac{\Delta t}{\Delta x} \Delta \mathbf{F}_i^{(\text{HLL})}(\mathbf{V}^{(n)}) \\ \mathbf{V}_i^{(**)} &= \mathbf{V}_i^{(*)} + \frac{\Delta t}{\Delta x} \Delta \mathbf{F}_i^{(\text{HLL})}(\mathbf{V}^{(*)}) \\ \mathbf{V}_i^{(n+1)} &= \frac{1}{2} \left(\mathbf{V}_i^{(n)} + \mathbf{V}_i^{(**)} \right) \end{aligned}$$

Here, $\Delta t := t^{(n+1)} - t^{(n)}$ and $\Delta \mathbf{F}_i^{(\text{HLL})}$ being the actual approximation of the surface integral defined according to

$$\Delta \mathbf{F}_i^{(\text{HLL})}(\mathbf{V}^{(n)}) := \mathbf{F}_{i-\frac{1}{2}}^{(\text{HLL})}(\mathbf{V}^{(n)}) - \mathbf{F}_{i+\frac{1}{2}}^{(\text{HLL})}(\mathbf{V}^{(n)})$$

The HLL flux $\mathbf{F}_{i-\frac{1}{2}}^{(\text{HLL})}(\mathbf{V}^{(n)})$ approximates the local Riemann problem at the interface between the two adjacent cells i and $i-1$. It approximates the local solution as to consist of two waves with one intermediate state. The wave speed estimates are denoted by s_R for the fast wave and s_L for the slow wave, respectively. With $\mathbf{V}_L^{(n)}$ and $\mathbf{V}_R^{(n)}$ being the reconstructions of $\mathbf{V}^{(n)}$ on the left and right sides of the interface $i - \frac{1}{2}$, the numerical flux is given by

$$\mathbf{F}_{i-\frac{1}{2}}^{(\text{HLL})}(\mathbf{V}^{(n)}) = \begin{cases} \mathbf{F}(\mathbf{V}_L^{(n)}) & 0 \leq s_L \\ \frac{s_R \mathbf{F}(\mathbf{V}_L^{(n)}) - s_L \mathbf{F}(\mathbf{V}_R^{(n)}) + s_R s_L (\mathbf{V}_R^{(n)} - \mathbf{V}_L^{(n)})}{s_R - s_L} & s_L \leq 0 \leq s_R \\ \mathbf{F}(\mathbf{V}_R^{(n)}) & s_R \leq 0 \end{cases}$$

The approximate wave speeds s_R and s_L , are chosen as upper bounds for the maximal and minimal eigenvalues λ_{\max} and λ_{\min} of the system.

$$\lambda_{\max} < s_R \quad \lambda_{\min} > s_L \quad (7.8)$$

For systems with more than two state variables, the solution of a Riemann problem in general exhibits more than two waves. The basic HLL assumption simplifies the solution structure significantly. However, this approach has two main advantages:

- There is no need for a decomposition of the flux Jacobian, as the numerical flux function solely relies on the evaluation of the flux itself
- As shown by Einfeldt [30], the system is positivity conserving. That means, that in the absence of source terms, a strictly positive function remains positive for all times

The latter property is essential in the numerical solution of shallow flow models, in which the height is always non-negative. The same is true for compressible fluid flow, in which density and internal energy are intrinsically positive quantities as well.

Any two-dimensional computation will be done on a Cartesian grid, such that a generalization of the scheme to two dimensions is straight-forward. That is why an explicit formulation of the scheme in two dimensions will be omitted. For details we refer to [58].

Stability

The scheme is formulated in a consistent way to the model equations [35]. Hence, additional stability guarantees convergence. As for any kind of finite volume method, the CFL-condition (Courant-Friedrichs-Lewy-condition) is a necessary condition for the scheme to be stable. It states, that the time step has to be chosen, such that information traveling with the realistic physical speed, can only affect neighboring cells. Formally, that means

$$\frac{\lambda_{\max} \Delta t}{\Delta x} < 1$$

Because of the non-linearity in the underlying system, yet another stability concept is required, the so-called TV-stability (total variation stability). The latter is fulfilled in particular, if the method exhibits the TVD-property (total variation diminishing-property). For details on the non-linear stability concept, we refer to [58].

We can ensure the scheme to be TVD, by applying slope limitation to the linear reconstruction on the cell values. The limiter applied in most of the computations within this thesis is the Minmod limiter [75]. However for testing and cross-checking we sometimes also use van-Leer limiter [57].

7.2 Homogeneous system

7.2.1 HLL Wave speeds

When applying the HLL scheme, the big issue is the choice of appropriate wave speeds. If the full spectrum is given in a closed form, one can take the explicit expressions for the fastest and the slowest waves. For systems, which exhibit a Roe matrix, this choice can be relaxed to speeds suggested by Einfeldt [30]. In our system however, we have neither an explicit expression for the fastest and slowest wave, nor a Roe-matrix, such that we make use of the previously derived upper and lower bounds on the systems' eigenvalues. Then according to the presented eigenvalue analysis in Section 5.1, λ_{\max} and λ_{\min} are given by

$$\begin{aligned}\lambda_{\min} &= \frac{(U_1 + U_2)}{2} - \sqrt{\mathbf{c}^T \mathbf{m}} \cdot w(u^*, m^*) \\ \lambda_{\max} &= \frac{(U_1 + U_2)}{2} + \sqrt{\mathbf{c}^T \mathbf{m}} \cdot w(u^*, m^*)\end{aligned}$$

with weights of the celerity $w(u^*, m^*)$, that depend only on the scaled absolute value of the velocity difference and a scaled mass difference. Substituting the previously derived upper bounds $\tilde{w}(u^*, m^*) = \frac{|u^*|}{2} + 1$ for the exact values, the expressions simplifies reasonably.

Before writing down the wave speed estimates in their final version, we have to consider a last subtlety. In shallow geophysical flows, states of zero heights, so-called dry states, can appear. In such cases, we will follow an approach, originally proposed by Toro [87] for the shallow water equations. All in all one gets

$$\begin{aligned}
 s_L &= \begin{cases} \frac{1}{2}(U_1 + U_2) - \left(\sqrt{\mathbf{c}^T \mathbf{m}} + \frac{1}{2}|(U_1 - U_2)|\right) & \text{left side wet} \\ \frac{1}{2}(U_1 + U_2) - 2\left(\sqrt{\mathbf{c}^T \mathbf{m}} + \frac{1}{2}|(U_1 - U_2)|\right) & \text{left side dry} \end{cases} \\
 s_R &= \begin{cases} \frac{1}{2}(U_1 + U_2) + \left(\sqrt{\mathbf{c}^T \mathbf{m}} + \frac{1}{2}|(U_1 - U_2)|\right) & \text{right side wet} \\ \frac{1}{2}(U_1 + U_2) + 2\left(\sqrt{\mathbf{c}^T \mathbf{m}} + \frac{1}{2}|(U_1 - U_2)|\right) & \text{right side dry} \end{cases}
 \end{aligned}$$

Note, that in two dimensions, the averaged velocity is projected in the direction of the interface unit normal $n^{(k)}$ and the same is true for the weighted velocity difference u^* . However, for a Cartesian grid, which will be applied in the ongoing of this work, the direction of $n_{(i,k)}$ either corresponds to the x - or the y - axis normals and the previously mentioned projection reduces to the choice of the relevant velocity component.

A final remark is devoted to the problem of ellipticity in the system. The presented choice of wave-speeds is always well-defined and real, and the same is true for first pair of exact eigenvalues in the system. Thus, by making the HLL assumption of only two waves to be present in the local solution, we completely avoid the problem of ellipticity, at least in the construction of the numerical scheme. We will investigate the numerical consequences below.

7.2.2 Empirical Convergence

To test the empirical order of convergence of the numerical scheme for the homogeneous system, the computational domain $[-1, 1]^2$ is discretized with quadrilateral cells of cell size $\Delta x = \Delta y$. The grid hierarchy is given by 4 levels and a reference grid. For every level, the number of cells per row N_i and the resulting grid size Δx_i are listed

N_0 :	10 cells	Δx_0	= 0.2
N_1 :	20 cells	Δx_1	= 0.1
N_2 :	40 cells	Δx_2	= 0.05
N_3 :	80 cells	Δx_3	= 0.025
N_{ref} :	400 cells	Δx_{ref}	= 0.005

The bulk mass of the computed solution on grid level k is denoted by $m^{(k)} = \sum m_i^{(k)}$, $k \in \{0, 1, 2, 3, ref\}$. Then the L_1 -error of the bulk mass, with respect to the reference solution

	HLL + Euler	HLL + CD + Heun	HLL + MM + Heun
Err_0	0.3622	0.1045	0.2258
Err_1	0.1829	0.0301	0.0816
Err_2	0.0948	0.0076	0.0253
Err_3	0.0447	0.0018	0.0070
EOC	1.01	1.94	1.67

Table 7.1: Empirical order of convergence for three test runs: Without a limiter (first column), with central differences (second column) and with a Minmod limiter (third column)

is given by

$$Err_k = \Delta x_k^d \sum |m^{(k)} - m^{(ref)}| \quad (7.9)$$

The sum is taken over all cell of the particular grid level, d is the dimension of the computational domain. The empirical order of convergence between two grid levels is then computed to be

$$Eoc_{k,l} = \frac{\log\left(\frac{err_k}{err_l}\right)}{\log\left(\frac{N_l}{N_k}\right)} \quad (7.10)$$

To analyze the empirical convergence order, let us consider smooth, periodic initial data, defined according to ($i \in \{1, 2\}$)

$$\begin{aligned} m_i(x, y) &= 1.5 + 0.5 \sin(\pi x) + 0.25 \cos(\pi y) \\ m_i(x, y)U_i(x, y) &= 1 + 0.25 \cos(\pi x) + 0.5 \sin(\pi y) \\ m_i(x, y)V_i(x, y) &= 1 + 0.5 \sin(\pi x) + 0.25 \cos(\pi y) \end{aligned}$$

Table 7.1 summarizes the empirical order of convergence for three test runs. In the first, the second-order Heun-scheme was applied without a linear reconstruction of the cell values and the time integration was given by an explicit Euler step. In the second run, central differences have been used for the linear reconstruction in the cells, and the time integration is given by a Heun scheme. The third calculation incorporates a Minmod limitation of the slopes, and time integration is again done by a Heun scheme.

7.2.3 Two-dimensional column collapse

The following column collapse problem demonstrates the achievements of the second order scheme in comparison to the first order calculation. On the flat, square computational

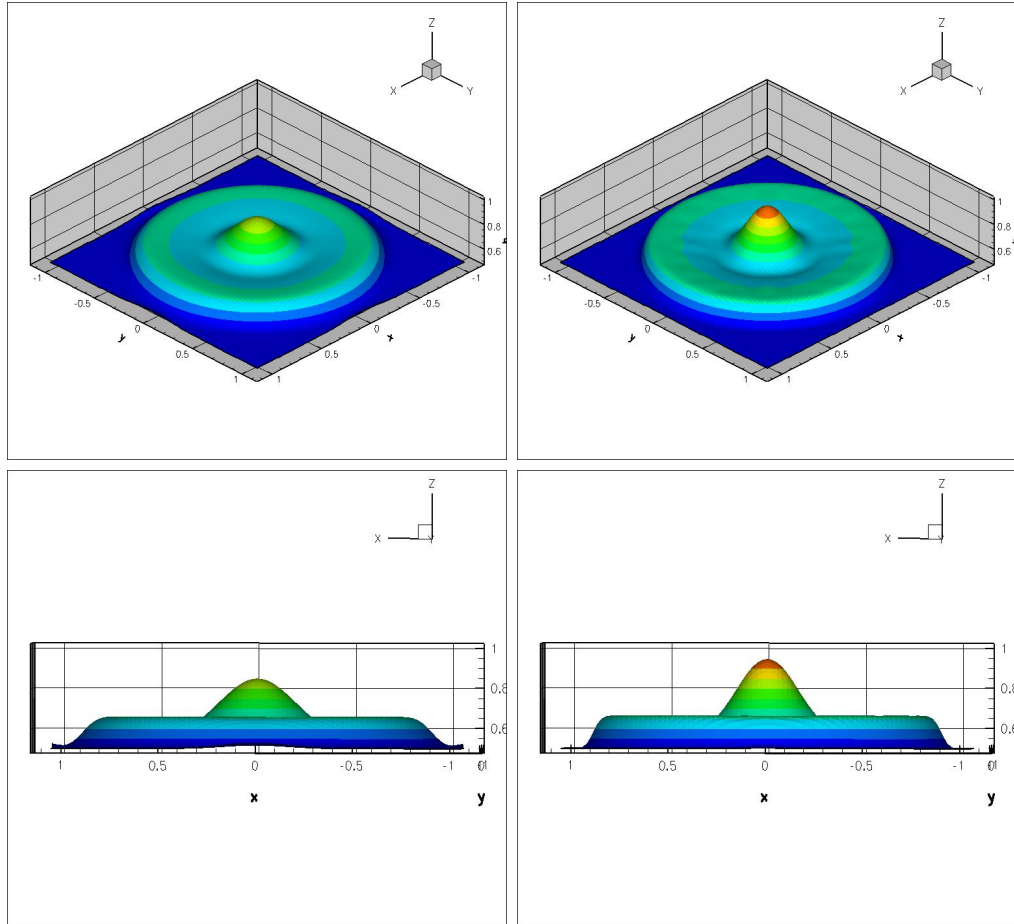


Figure 7.1: Upper left and lower left: First order solution to the two-dimensional column collapse problem; Upper right and lower right: Second order solution to the two-dimensional column collapse problem; The quality difference is seen in the height of the local maximum and the slope of the outwards traveling surge.

domain $\mathcal{C} := [-1, 1]^2$, the initial configuration of the variables is given by

$$m_1(x, y, 0) = \begin{cases} 0.5 & \text{if } \sqrt{x^2 + y^2} \leq 0.25 \\ 0.0 & \text{else} \end{cases}$$

$$m_2(x, y, 0) = \begin{cases} 0.5 & \text{if } \sqrt{x^2 + y^2} \leq 0.25 \\ 0.0 & \text{else} \end{cases}$$

$$U_1(x, y, 0) = 0.0$$

$$U_2(x, y, 0) = 0.0$$

The calculation has been done with a CFL-number of 0.9. In Figure 7.1, results of the computation are shown. All four plots show a surface plot of the bulk mass at the final computation time. Upper left and lower left picture correspond to the first order scheme, Upper right and lower right picture to the second order scheme. One clearly sees

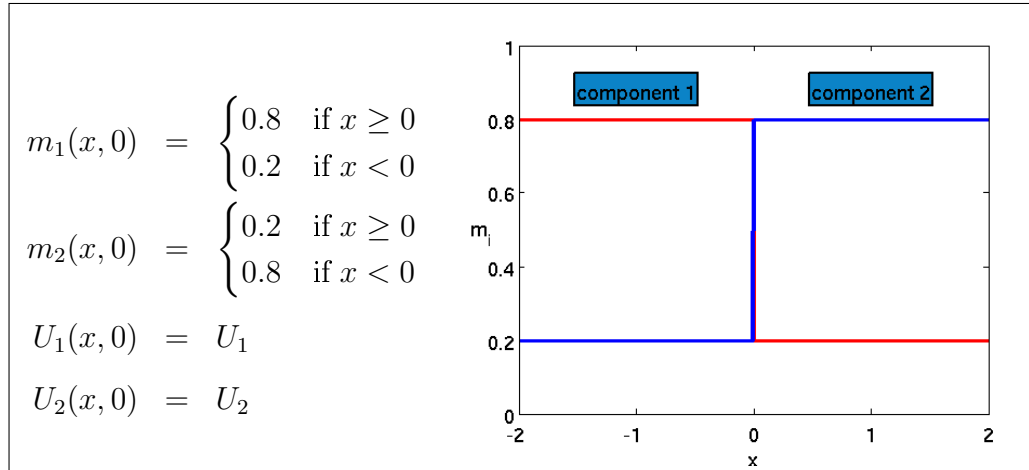


Figure 7.2: Initial Data of the 1D Riemann problem. The components' masses have a discontinuity at $x = 0$, the components' velocities are constant over the whole computational domain

the difference, as the second order computation exhibits a higher local maximum in the center of the column, and the front of the outwards traveling surge is steeper.

7.3 One-dimensional Riemann examples

Let us consider a one-dimensional Riemann problem. The applied numerical scheme is second order in time (Runge-Kutta-Heun) and space (linear reconstruction with minmod limiter). It involves the HLL-approximate Riemann solver derived in the previous section. The bounds on the wave speeds have also been used to determine the time-step. The latter is chosen corresponding to a CFL-number 0.9. The computational domain is given by the interval $[-2, 2]$, discretized by 2000 cells, such that the uniform grid size is $\Delta x \equiv 0.002$.

In Figure 7.2, the initial data for the problem is summarized. A discontinuity at $x = 0$ is assumed for the masses, whereas the velocities of the single components are initially constant in whole computational domain. Now four test cases **(A)**-**(D)** with increasing initial relative velocity are analyzed. In case **(A)** both velocities are chosen to be zero $U_1 = U_2 = 0$, which corresponds to a the dam-break problem. In case **(B)**, we set $U_1 = 1.0$ and $U_2 = -0.3$, and **(C)** starts with $U_1 = 1.0$ and $U_2 = -0.7$. The final case **(D)** has the initial data $U_1 = 1.0$ and $U_2 = -2.2$. In figure 7.3, the initial states are projected into the (u^*-m^*) phase space. The blue ellipses indicate elliptic regions, such that one sees, that the initial configurations of **(A)**, **(B)** and **(D)** fall into the hyperbolic regions, whereas test case **(C)** is within the non-hyperbolic region.

Moreover in Figure 7.3, the solution at the final computation time $t_{final} = 0.4$ is projected into the (u^*-m^*) phase space. The corresponding final heights are plotted in the Figure 7.4. In the computational test cases **(A)** and **(D)** the intermediate states correspond to

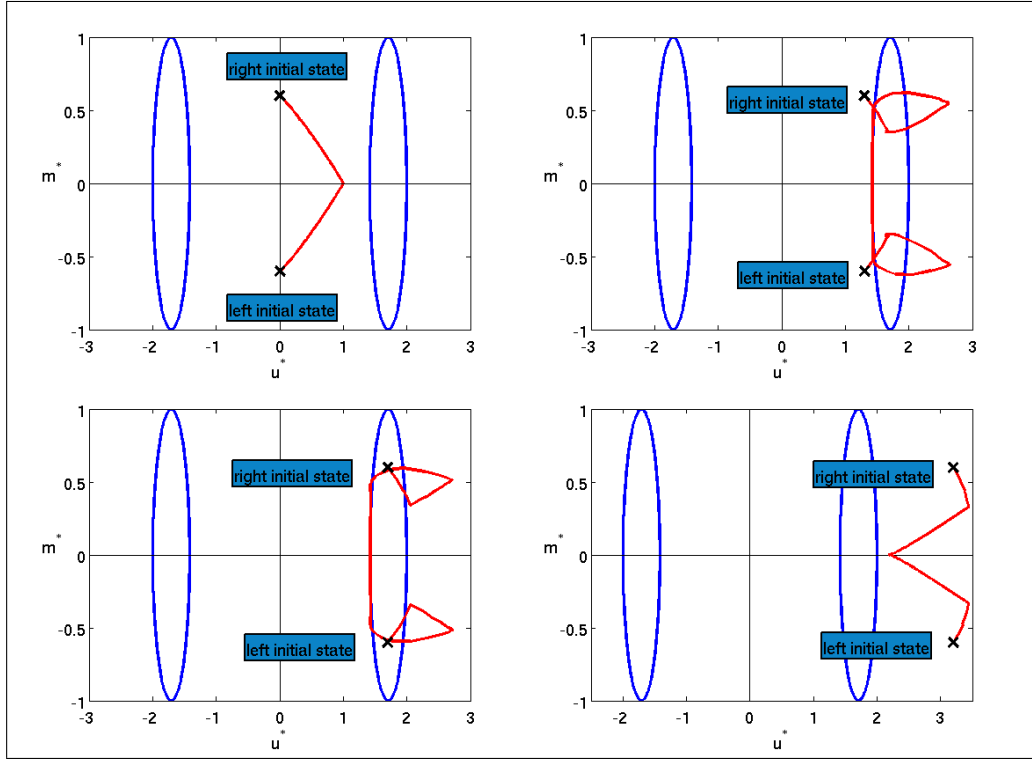


Figure 7.3: Phase space with initial configuration and path of the solution: L.u. **(A)** and R.l. **(D)** - the connecting path is completely within the hyperbolic region. R.u. **(B)** and L.l. **(C)** - the connecting path enters the elliptic region

the locations in the phase space, where the direction of the connecting path changes and the solution follows a different Riemann invariant. However, the first and third location are hard to be seen for **(A)**. In both cases the region right in the middle corresponds to a mixed configuration of both components, we will therefore talk about the mixed state in the following. The solutions of **(B)** and **(C)** both enter the elliptic region. In this region the slow pair of eigenvalues is complex, such that the mixed state cannot be established. Instead of two slow waves that connect, the mixed state, here, instabilities occur in the middle region, that are clearly unphysical.

We saw already in the eigenvalue analysis of the system, that the fast pair of eigenvalues is associated with the shallow water waves, whereas the second, slow pair is associated with the mixing of components. This is now supported by the consideration of this simple one-dimensional Riemann problem. However, the slow waves are not the only mechanism causing for mixing of components, but the interact with the momentum relaxation due to relative slip and result into phase diffusion. In fact, for our kind of problems, the time scale for the momentum relaxation is so small, that the domains, in which the hyperbolicity of the system breaks down can be considered to be unphysical.

To exclude, that the instabilities are caused by the way the approximate Riemann solver is constructed, all computations have been redone with a rigorous solution for the fastest wave speeds. These were computed at each time step by applying a Newton-scheme to find the first and fourth root of the characteristic polynomial. Using the computational ap-

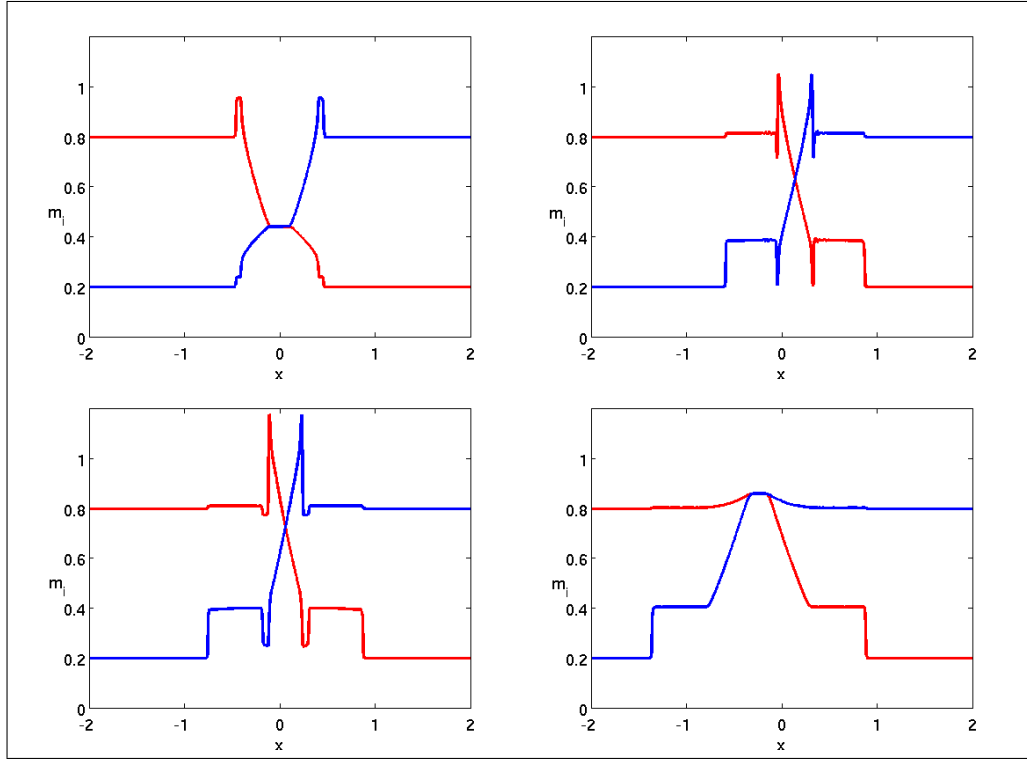


Figure 7.4: Plot of the computed single component masses at $t_{final} = 0.4$. Test case (A) and (D) clearly develop three intermediate states corresponding to the solutions path. Test case (B) and (C) develop instabilities in the middle region.

proximated wave speeds, rather than the analytically approximated ones, did not change the results of the computation to any significant order. Also a calculation with a van-Leer limiter gave the same results.

1D simplified Riemann problem

Finally the test case (C) is considered in the absence of inertial terms. For a plot of the solution see Figure 7.5. This corresponds to the simplified Riemann problem, which is unconditionally hyperbolic.

7.4 Momentum relaxation and phase diffusion

Now the momentum relaxation $\mathbf{R}(\mathbf{V})$ is included into the numerical scheme. Together with the flux $\mathbf{F}(\mathbf{V})$, the system is given by

$$\partial_t \mathbf{V} + \partial_x \mathbf{F}(\mathbf{V}) = \mathbf{R}(\mathbf{V}) \quad (7.11)$$

At first, invariant and variant contributions of the relaxation will be identified. Next,

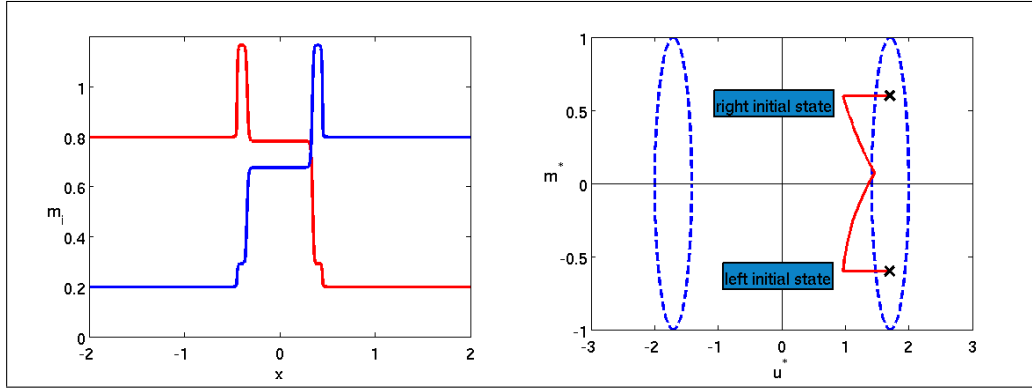


Figure 7.5: Computed masses and phase space for the solution of the Riemann problem for the simplified model

a stable way to include a scalar relaxation into the second order Heun scheme is introduced. Afterwards, this concept is applied to the general suspension model. Finally a 1D-Riemann problem, this time solved with additional momentum exchange demonstrates the relaxation behavior.

7.4.1 Invariant and variant part of the relaxation

For a zero flux $\mathbf{F}(\mathbf{V}) \equiv 0$, system (7.11) reduces to

$$\begin{aligned} \frac{d}{dt} m_1 &= 0 \\ \frac{d}{dt} m_2 &= 0 \\ \frac{d}{dt} (m_1 U_1) &= -\frac{1}{\tau} \frac{m_1 m_2}{r m_1 + m_2} (U_1 - U_2) \\ \frac{d}{dt} (m_2 U_2) &= \frac{1}{\tau} \frac{r m_1 m_2}{r m_1 + m_2} (U_1 - U_2) \end{aligned} \quad (7.12)$$

Prior to the formulation of the actual numerical scheme, invariant and variant components of the momentum exchange are identified. In the absence of the flux, the masses m_1 and m_2 are constant. Let us consider the following transformation $T : \mathbb{R}^4 \rightarrow \mathbb{R}^4$.

$$\begin{pmatrix} m_1 \\ m_2 \\ W_1 \\ W_2 \end{pmatrix} := T \begin{pmatrix} m_1 \\ m_2 \\ m_1 U_1 \\ m_2 U_2 \end{pmatrix} = \begin{pmatrix} m_1 \\ m_2 \\ U_1 - U_2 \\ \frac{r m_1 + m_2}{m_2} U_1 + \frac{r m_1 + m_2}{r m_1} U_2 \end{pmatrix} \quad (7.13)$$

By making use of (7.12), a short calculation gives

$$\frac{d}{dt} W_1 = -\frac{1}{\tau} W_1 \quad \text{and} \quad \frac{d}{dt} W_2 = 0 \quad (7.14)$$

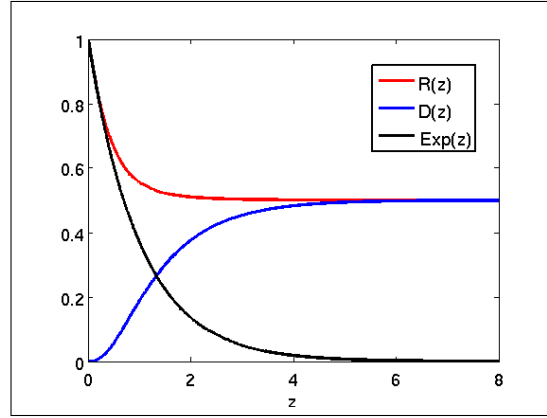


Figure 7.6: Consistency factor $R(z)$ and analytical solution $\text{Exp}(z)$ to the relaxation. $D(z)$ denotes the difference between both.

Hence, the momentum exchange acts as a scalar relaxation on the velocity difference W_1 , whereas a certain concentration weighted average of the velocities W_2 is invariant. This is a crucial results, as it states, that changing to the transformed variables W_1 and W_2 , the coupled momentum exchange reduces to a scalar relaxation and the invariant quantities m_1 , m_2 and W_2 .

7.4.2 Relaxation in the Runge-Kutta Heun scheme

To introduce the basic scheme, an ordinary differential equation for the scalar function $V(t)$ is considered. With a right hand side, that consists of an autonomous contribution $f(V)$ and a relaxation part $-\frac{1}{\tau}V$ the differential equation is given by

$$\frac{d}{dt}V = f(V) - \frac{1}{\tau}V \quad (7.15)$$

V on a discrete level is denoted by $V^{(n)}$, $n \in \{0, \dots, N\}$.

For small τ the relaxation becomes stiff and an explicit discretization, as in Heun, is stable only for very small time steps Δt . In those cases, an implicit discretization is the appropriate choice. This motivates to account for the relaxation, by introducing a relaxation factor $r : \mathbb{R}^+ \rightarrow \mathbb{R}$ in $z := \frac{\Delta t}{\tau}$ in every predictor step. The Heun-relaxation scheme with such a relaxation factor is then defined as

$$\begin{aligned} V^{(*)} &= r(z)U^{(n)} + \Delta t f(V^{(n)}) \\ V^{(**)} &= r(z)U^{(*)} + \Delta t f(V^{(*)}) \end{aligned}$$

$$V^{(n+1)} = \frac{1}{2} (V^{(n)} + V^{(**)}) = \frac{1}{2} (1 + r^2(z)) V^{(n)} + \frac{\Delta t}{2} (r(z)f(V^{(n)}) + f(V^{(*)}))$$

According to [90], the relaxation factor $r(z)$ has to fulfill

$$\begin{aligned} r(0) = 1 \quad r'(0) = -1 \quad r''(0) = 0 \\ r(z) > 0 \quad \lim_{z \rightarrow \infty} r(z) = 0 \end{aligned} \quad (7.16)$$

in order to result into an overall second order Heun update. The first conditions can be interpreted as a consistency condition.

For the choice $r(z) := \frac{1}{1+z}$, the method corresponds to an incorporated implicit Euler discretization in every predictor step. However, this does not match the requirements, as we get $r''(0) \neq 0$. The choice $r(z) := 1 - z$ leads to an explicit Euler approximation of the relaxation and exactly recovers the standard Heun scheme. But as previously mentioned, it has poor stability properties for $\tau \ll 1$. The discrete relaxation factor that will be used in the ongoing of this work is given by

$$r(z) := \frac{1}{1 + z + z^2} \quad (7.17)$$

To demonstrate the performance of the latter, the case of a trivial function $f(V) \equiv 0$ is considered. Then the Heun-relaxation scheme reduces to a single evaluation of the consistency factor $R(z)$.

$$V^{(n+1)} = \frac{1}{2} (1 + r^2(z)) V^{(n)} = R(z) V^{(n)} \quad (7.18)$$

Figure 7.6 shows a plot of the consistency factor $R(z)$, as well as the analytical solution to the exponential, and their difference. It is immediately obvious, that the agreement is very good for $z < 1$, whereas it is rather poor for $z \gg 1$. This corresponds to the fact, that the leading error in the local truncation error is a function of $\frac{1}{\tau}$, such that it will be big for small τ . However, the computation is stable and of second order asymptotically.

One could now think of improving the results by considering yet another relaxation factor, and in fact, instead of (7.17) every function of the form

$$r_k(z) := \frac{1}{\sum_{i=0}^k z^i} = \frac{1 - z}{1 - z^{k+1}} \quad (7.19)$$

fulfills the requirements (7.16), too. As indicated in Figure 7.7, a higher order k of function $r_k(z)$ brings improvement for time step of the order of τ , such that $z = \frac{\Delta t}{\tau} \approx 1$. In our system however, the relaxation is assumed to be more or less instantaneous, hence $\tau \ll \Delta t$. According to [90], the Heun-relaxation scheme is stable with a CFL number of $\frac{1}{2}$ independent of τ .

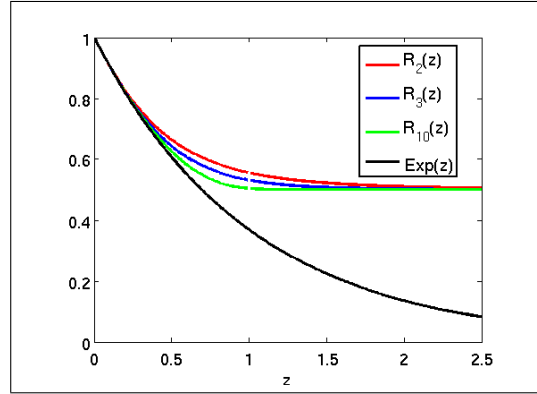


Figure 7.7: Consistency factor $R(z)$ and exponential function for different choices of the relaxation factor $r(z)$

7.4.3 Momentum relaxation in the uniform suspension model

Now, once again following [90], the previously introduced Heun-relaxation scheme is incorporated into the numerical scheme for the uniform suspension model by defining it as

$$\begin{aligned}\mathbf{V}_i^{(*)} &= \mathbf{r}\left(\mathbf{V}_i^{(n)}\right) + \frac{\Delta t}{\Delta x} \Delta \mathbf{F}_i^{(\text{HLL})}\left(\mathbf{V}^{(n)}\right) \\ \mathbf{V}_i^{(n+1)} &= \frac{1}{2} \left(\mathbf{V}_i^{(n)} + \mathbf{r}\left(\mathbf{V}_i^{(*)}\right) + \frac{\Delta t}{\Delta x} \Delta \mathbf{F}_i^{(\text{HLL})}\left(\mathbf{V}^{(*)}\right) \right)\end{aligned}$$

This time $\mathbf{r}(\cdot)$ is a relaxation operator, rather than the relaxation factor $r(z)$. However, due to the fact, that we identified variant and invariant part of the momentum exchange, the relaxation operator $\mathbf{r}(\cdot)$ can be reduced to an application of the previously introduced scalar relaxation factor $r(z)$ by defining.

$$\mathbf{r} \begin{pmatrix} m_1 \\ m_2 \\ m_1 U_1 \\ m_2 U_2 \end{pmatrix} := T^{-1} \begin{pmatrix} m_1 \\ m_2 \\ r(z) W_1 \\ W_2 \end{pmatrix} \quad (7.20)$$

Here, $T(\cdot)$ is the previously introduced transformation (7.13) of the state vector, hence $T^{-1}(\cdot)$ its inverse. It exists for a non-zero bulk mass.

The scheme has been applied to the 1D-Riemann test case (**C**) for $\tau \in \{\infty, 0.5, 0.1, 0.005\}$. $\tau = \infty$ corresponds to the absence of a momentum relaxation. In Figure 7.20 one can see the solutions' path through the phase space. Note that in the constant states, left and right relaxation takes place because $U_1 \neq U_2$. The smaller the time scale for the momentum relaxation, the faster the components velocities are relaxed to a mean value, meaning $u^* \rightarrow 0$. Hence, for strong momentum exchange, the projected state variables are constrained

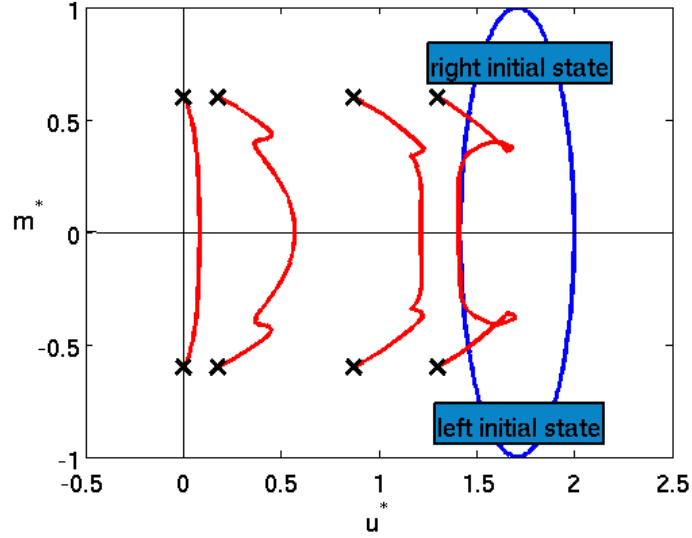


Figure 7.8: Riemann problem at $t=0.2$ evaluated for different τ ($\infty, 0.5, 0.1, 0.005$)

to the hyperbolic region, symmetric around $u^* = 0$. Then waves corresponding to the slow pair of eigenvalues together with the relaxation on the velocity differences give rise to a phase diffusion. This corresponds to the theoretical result derived in the section on the mathematical properties. Although theoretically states exist with a high velocity difference between the components, for our kind of flows, it is reasonable to assume that all physically relevant states are within the hyperbolic domain.

7.5 Frictional source terms

Finally, gravitational and frictional source terms $\mathbf{G}(\mathbf{V})$ are included into the scheme. They are discretized as an explicit contribution to the Heun-relaxation scheme. The overall update is then given by

$$\begin{aligned}\mathbf{V}_i^{(*)} &= \mathbf{r}\left(\mathbf{V}_i^{(n)}\right) + \frac{\Delta t}{\Delta x} \Delta \mathbf{F}_i^{(\text{HLL})}\left(\mathbf{V}^{(n)}\right) + \Delta t \mathbf{G}\left(\mathbf{V}_i^{(n)}\right) \\ \mathbf{V}_i^{(n+1)} &= \frac{1}{2} \left(\mathbf{V}_i^{(n)} + \mathbf{r}\left(\mathbf{V}_i^{(*)}\right) + \frac{\Delta t}{\Delta x} \Delta \mathbf{F}_i^{(\text{HLL})}\left(\mathbf{V}^{(*)}\right) + \Delta t \mathbf{G}\left(\mathbf{V}_i^{(*)}\right) \right)\end{aligned}$$

In the following, we will demonstrate two cross-couplings between different physical effects, by looking at a basic setting on an inclined plane.

7.5.1 Component dependent friction

Let us consider an initially uniformly mixed box, that starts its motion due to gravitational acceleration. Both components exhibit different friction coefficients. We will see,

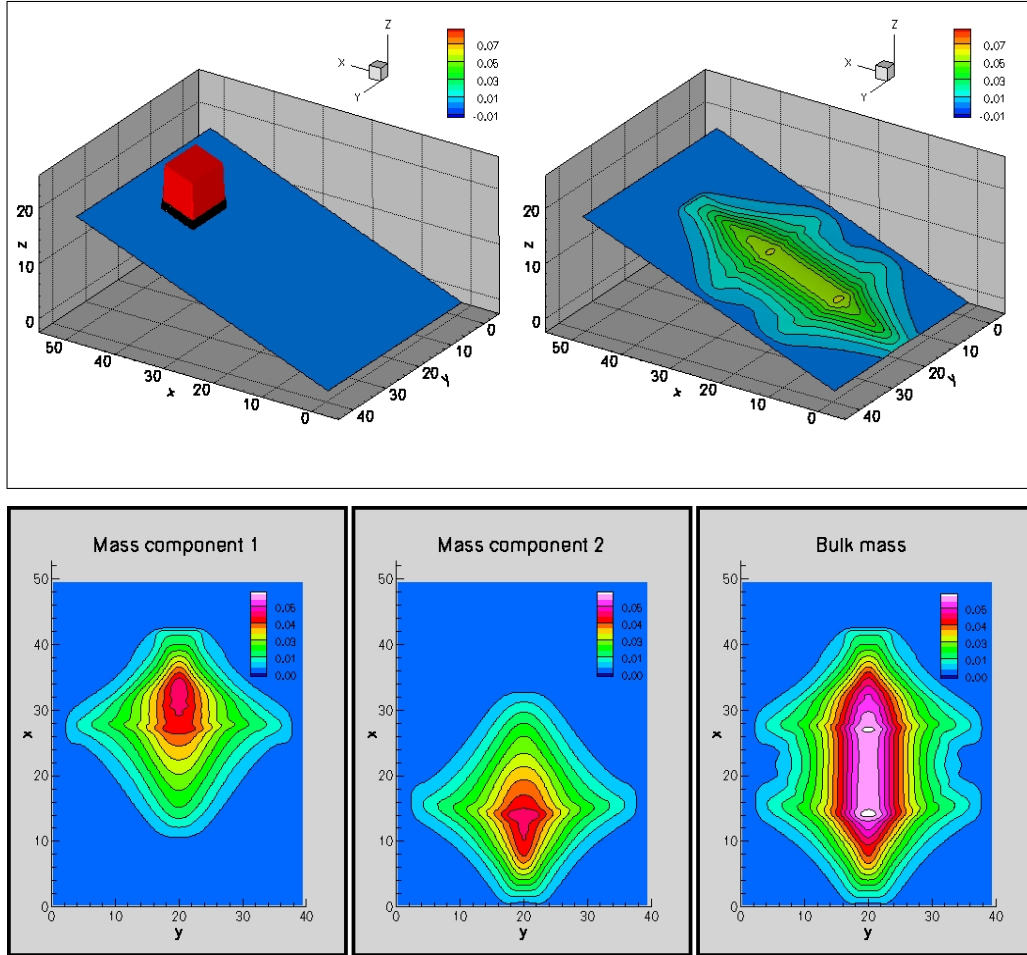


Figure 7.9: Results of Case(A): Component dependent friction with negligible momentum exchange; Upper left: Initial data on an inclined plane; Upper right: Surface plot of the bulk mass at $t_{\text{final}} = 15$; Lower: Contour plots of the masses of species one (left), species two (middle), and the bulk (right) evaluated at $t_{\text{final}} = 15$. The different components tend to separate.

that for small momentum exchange the components start to separate, whereas for strong momentum exchange, they move as one bulk.

General setting

The computational domain $\mathcal{C} := [0, 50] \times [0, 40]$ is inclined along the x -axis by an angle $\zeta = 20^\circ$. The plane is flat, such that $\partial_x b \equiv \partial_y b \equiv 0$. For both spatial dimensions, the grid resolution is the same ($\Delta x = \Delta y = 0.25$). We consider initial data of the following form

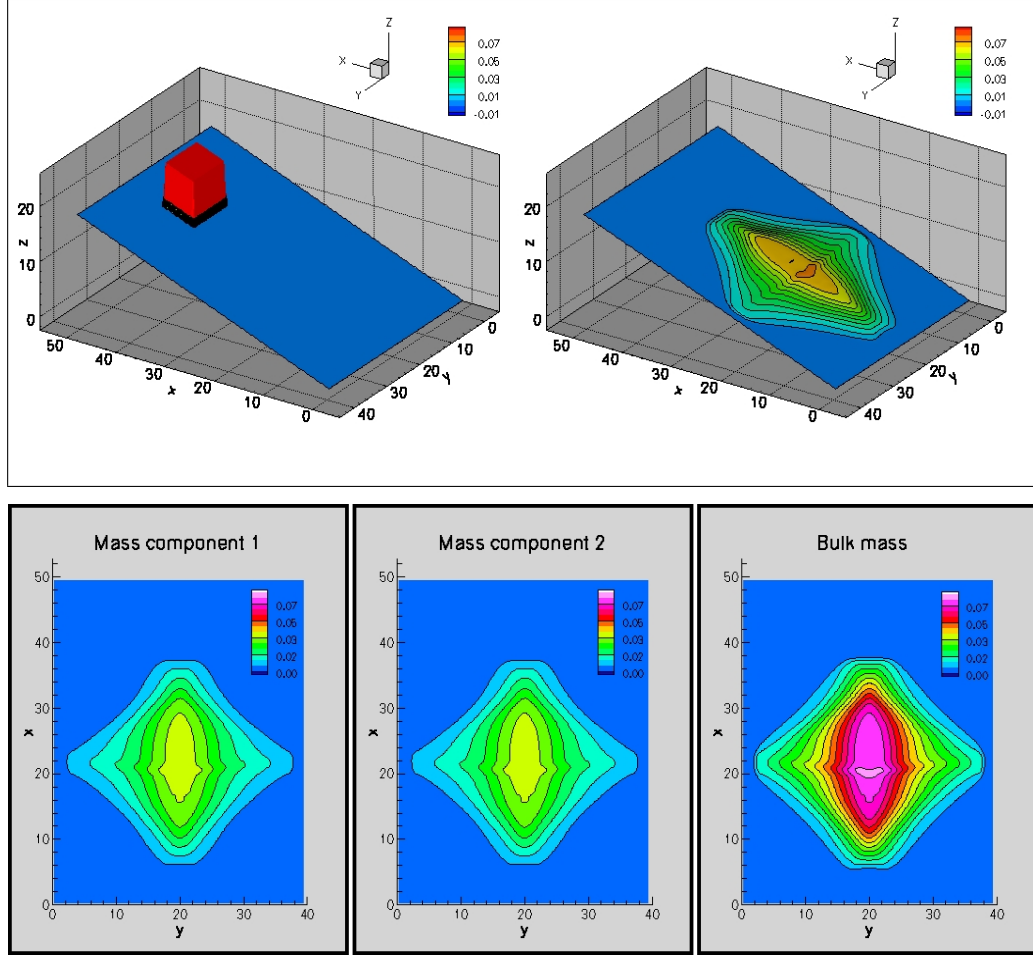


Figure 7.10: Results of Case(B): Component dependent friction with strong momentum exchange; Upper left: Initial data on an inclined plane; Upper right: Surface plot of the bulk mass at $t_{\text{final}} = 15$; Lower: Contour plots of the masses of species one (left), species two (middle), and the bulk (right) evaluated at $t_{\text{final}} = 15$. The mixture moves as one bulk, due to strong viscous-drag type coupling.

$$m_1(x, y, 0) = \begin{cases} 0.2 & \text{if } 37.5 \leq x \leq 42.5 \quad \text{and} \quad 15 \leq y \leq 25 \\ 0.0 & \text{else} \end{cases}$$

$$m_2(x, y, 0) = \begin{cases} 0.2 & \text{if } 37.5 \leq x \leq 42.5 \quad \text{and} \quad 15 \leq y \leq 25 \\ 0.0 & \text{else} \end{cases}$$

$$U_1(x, y, 0) = 0.0 \quad U_2(x, y, 0) = 0.0$$

Entrainment and deposition rates are neglected and the friction coefficients for the species are $\mu_1 = 0.28$ and $\mu_2 = 0.1$. Then, according to (4.35), the net acceleration force on the components in x -direction is given by

$$S_1 = m_1 \left(\sin \zeta - \frac{U_1}{\|U_1\|} \mu_1 \cos \zeta \right)$$

$$S_2 = m_2 \left(\sin \zeta - \frac{U_2}{\|U_2\|} \mu_2 \cos \zeta \right)$$

The choice of inclination angle ζ and friction coefficients μ_1, μ_2 implies $A_1 = 0.5 \cdot A_2$, when A_k are given by $A_k := \sin \zeta - \mu_k \cos \zeta, k \in \{1, 2\}$. For a sketch of the general setting, we refer to the upper, left picture in Figure 7.9.

The calculation up to the final time $t_{\text{final}} = 15$ is done by applying the second order Heun-relaxation scheme, introduced within this chapter. The time step is dynamically chosen and satisfies a CFL number of 0.9.

Let us consider two cases:

- Case (A): Negligible momentum relaxation, $\tau = 100$
- Case (B): High momentum relaxation, $\tau = 0.001$

Figure 7.9 contains the results for Case (A). The upper left picture shows a surface plot of the initial mass, and the upper right picture a surface plot of the bulk mass evaluated at t_{final} . One can clearly make out two local maxima. In the second row, the inclined plane is projected into the x - y -domain, and contours display the masses of component one (left), component two (middle), and the bulk mass (right), respectively. Due to the lower net acceleration of the first component, it moves slower than the second one. Due to the weak momentum exchange, $\tau = 100$, there is no strong coupling mechanism present in the system. Consequently the two species will eventually be separated from each other, and develop independent dynamics. The plot of the bulk mass accounts for both components, which explain the development for the two maxima.

In Figure 7.10, the results of Case (B) are displayed. This time, the momentum exchange is strong, $\tau = 0.001$. Again, the upper two surface plots show the initial bulk mass on the left and the bulk mass at the final time on the right. The surface plot of the final mass differs from Case (A), as it exhibits only one local maximum. The contour plots in the second row, once again provide more details, as they split up the bulk mass in the contributing components. We see, that both maxima are located in the same position. Hence, although the species exhibit net accelerating forces, that differ by 100%, the mixture moves as one bulk material. This is due to the strong momentum exchange. Any appearing velocity differences are relaxed towards the barycentric bulk velocity.

7.5.2 Lateral mixing

A concluding example in this chapter is devoted to the lateral mixing of components. Let us once again consider an inclined plane, this time with the initial configuration

$$m_1(x, y, 0) = \begin{cases} 0.5 & \text{if } 37.5 \leq x \leq 42.5 \quad \text{and} \quad 10 \leq y \leq 20 \\ 0.3 & \text{if } 37.5 \leq x \leq 42.5 \quad \text{and} \quad 20 \leq y \leq 30 \\ 0.0 & \text{else} \end{cases}$$

$$m_2(x, y, 0) = \begin{cases} 0.3 & \text{if } 37.5 \leq x \leq 42.5 \quad \text{and} \quad 10 \leq y \leq 20 \\ 0.5 & \text{if } 37.5 \leq x \leq 42.5 \quad \text{and} \quad 20 \leq y \leq 30 \\ 0.0 & \text{else} \end{cases}$$

$$U_1(x, y, 0) = 0.0 \quad U_2(x, y, 0) = 0.0$$

In contrast to the previous example, the initial volume consists of a left state, with a high concentration of the first component, and a right state, with a low concentration of the first component. Both states are connected by a jump in the concentration. However, that initial masses are chosen, such that the bulk mass is constant over this jump in the concentration. For a plot of the initial configuration, we refer to the upper row of Figure 7.11. Here, the left hand side shows a surface plot, and the right hand side a lateral cut through the surface at $x = 40$.

For positive times the bulk accelerates in x -direction. In addition to that, the components start to mix at the internal concentration-jump. The second and third line in Figure 7.11 show once again a surface plot of the bulk mass, as well as lateral cuts located at $x = 36.6$ (second row) and $x = 16$ (third row). We clearly see, that a mixing of components is taking place at the internal boundary of the bulk. Eventually both concentration of both species will be evenly distributed throughout the flowing body.

The same example is repeated with $\tau = 100$, which corresponds to a negligible momentum exchange. The plot of the results, shown in Figure 7.12, is organized similar to the first example. The surface plots in row one to three show the bulk mass at the initial time $t = 0$ and for two later times. This time, the character of the lateral mixing corresponds to surge, traveling through the flowing body. Especially in the second row, we can make out the two waves, that originate at the internal concentration discontinuity and are moving towards the side edges of the bulk. These waves correspond to the slow discontinuities, that have been discussed in the Chapter 5.

Both examples, the separation of components and the lateral mixing on an inclined plane, demonstrate the capability of the model to describe mixing and separation of two components in a shallow flow contexts. However, the scheme still has to be generalized to solve the whole combined shallow flow model, proposed in Chapter 4.

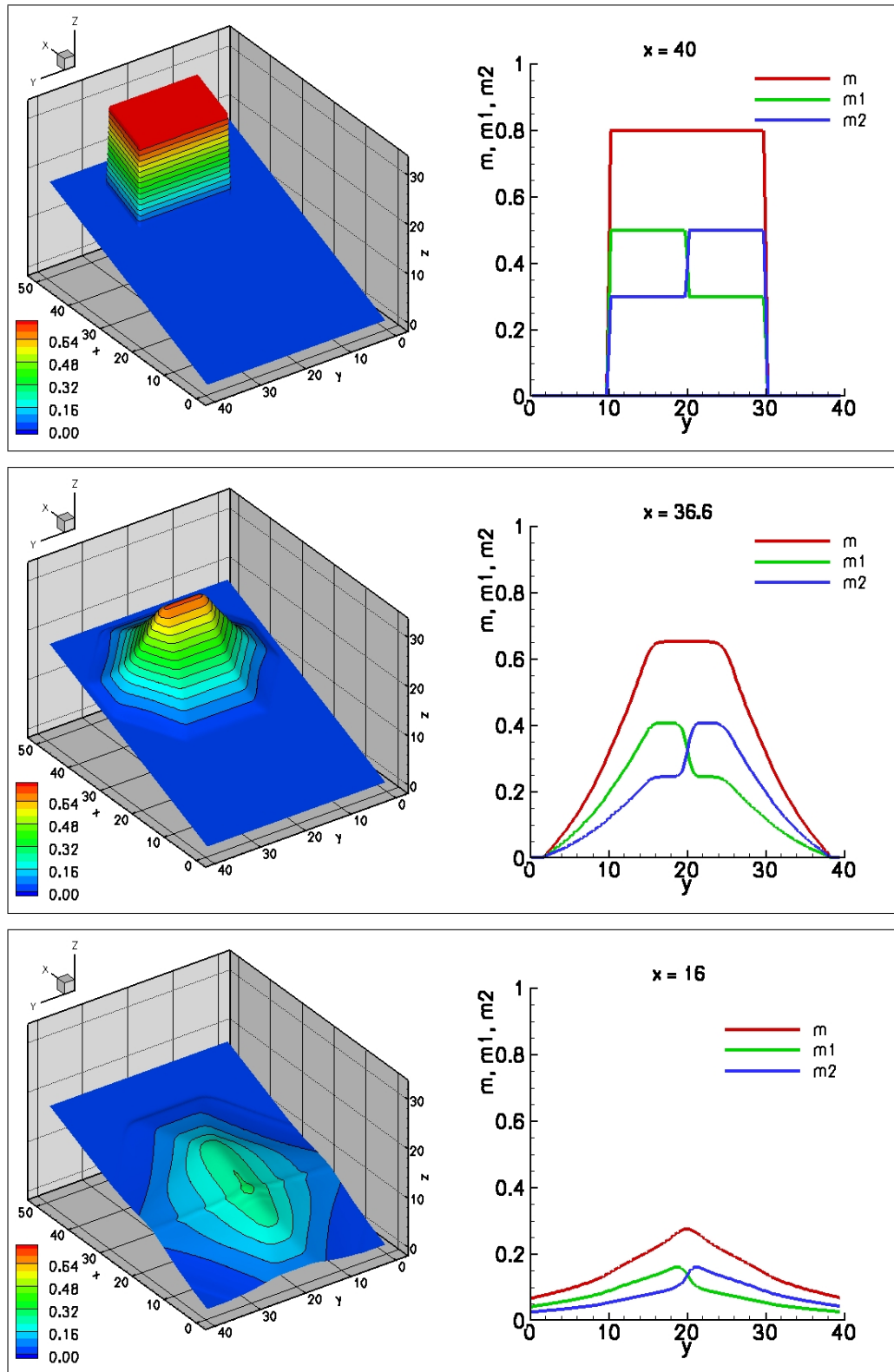
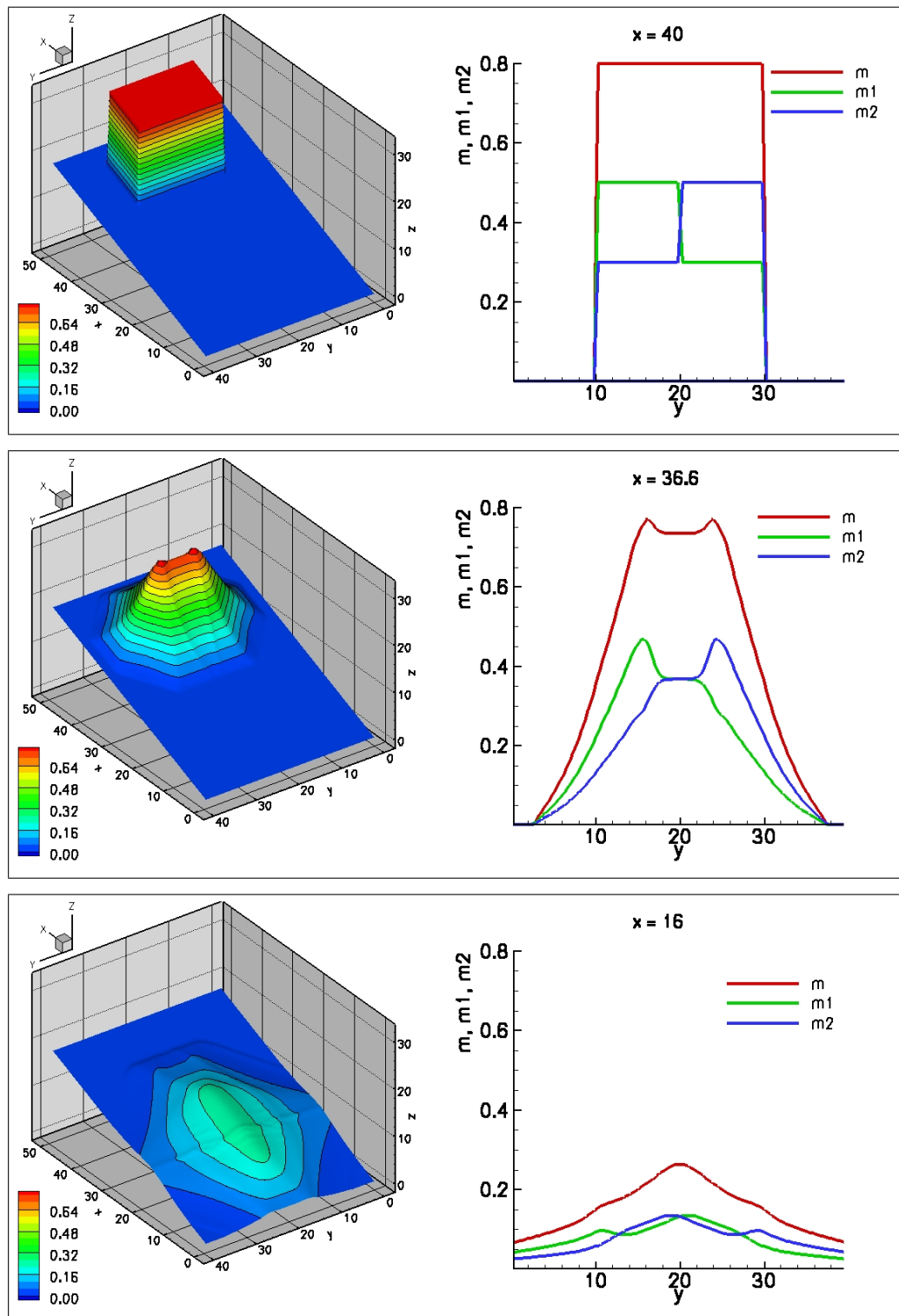


Figure 7.11: Lateral mixing on an incline ($\tau=0.001$):

Figure 7.12: Lateral mixing on an incline with negligible momentum exchange, $\tau=100$

Chapter 8

Outlook: Realistic test cases

Recent advances in simulating natural geophysical flows are based on stable and robust solution schemes of the shallow water system [6, 19, 34, 69, 66]. A rigorous discussion of such 1D and 2D schemes can be found in LeVeque [58]. Other fundamental contributions to the field are due to Toro [88, 89]. With minor modification these approaches can be applied to natural avalanche or debris flow models [76, 34]. However, most of the sophisticated solvers have been evaluated in a fairly simple framework. When modeling in real terrain the complex basal topography comes into play. Thus, in the last couple of years an effort has been invested in finding a correct numerical representation of topographically induced source terms (compare for instance [13]). In this concluding chapter, we will provide an outlook into numerical simulations in complex topography. In particular, we will discuss simulations conducted in the framework of the two data sets introduced in Chapter 2. Hence, the first example will be a chute flow on the USGS debris flow flume, and the second example at the Swiss Illgraben test site.

8.1 Chute flow

The U.S. Geological Survey Debris Flow Flume is described in Section 2.3.2. Simulations of a flume experiments using solver developed in Chapter 7 are shown. Prior to a discussion of the main results, the general setting is described.

8.1.1 General setting

The computational domain is determined by the geometry of the flume, shown in the upper left panel of Figure 8.1. It is discretized by a structured, quadrilateral mesh with constant grid width in both spatial dimensions $\Delta x = \Delta y = 0.05\text{m}$. The upper right panel in the same Figure shows the topography of the flume along longitudinal cut in the x -axis. In the initialization process, both geometry and topography are combined into a surface mesh, shown in the lower part of Figure 8.1. The surface mesh also includes the initial data, chosen as a dam-break problem with an initial volume of 9.4 m^3 . This

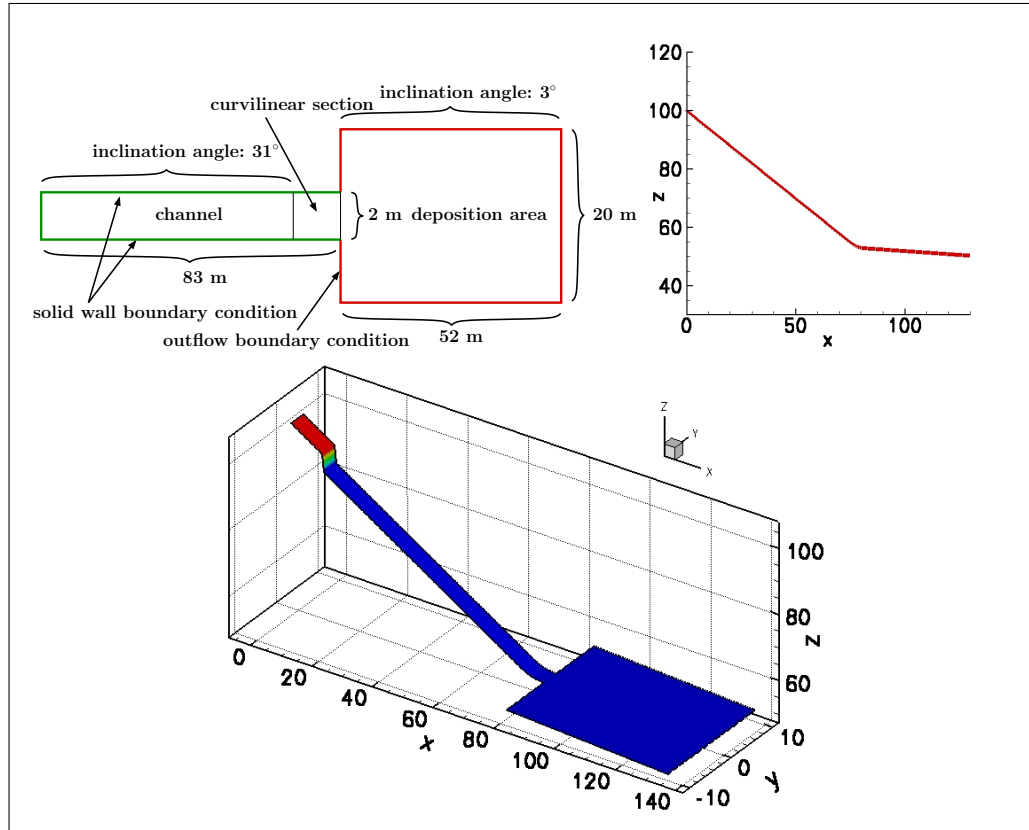


Figure 8.1: Upper left: Geometry of the USGS Debris Flow Flume; Upper right: Profile of the flume; Lower: Implemented computational domain with initial data (cmp. Section 2.1.2)

corresponds to an experiment conducted at the flume in September 2001. As a simplifying approximation, we choose solid and fluid components to contribute in equal part to the initial volume. The chute is axis-symmetric in y , such that it is sufficient to formulate the initial condition as a 1D-Riemann problem in x :

$$m_1(x, y, 0) = \begin{cases} 0.47 & \text{if } x \leq 10 \\ 0.0 & \text{else} \end{cases} \quad m_2(x, y, 0) = \begin{cases} 0.47 & \text{if } x \leq 10 \\ 0.0 & \text{else} \end{cases}$$

$$U_1(x, y, 0) = 0.0 \quad U_2(x, y, 0) = 0.0.$$

We solve for a mixture in uniform suspension and apply the HLL-Relaxation scheme introduced in Chapter 7. The model includes gravitational acceleration as well as both, basal friction and momentum exchange, the latter giving rise eventually to phase diffusion. The scheme is second order convergent in both space and time. The calculations have been performed with a CFL-number of 0.9. In order to determine the linear reconstructions of the cell values, two lines of ghost cells surround the actual computational domain.

Boundary conditions complete the basic setting of the simulation. In the channelized

Value	Measured Data	Simulation
Peak flow depth 66m	0.22m	0.38m
Peak flow depth 90m	0.38m	0.95m
Velocity 66m	10 m/s	8.8 m/s
Velocity 90m	5.1 m/s	5.4 m/s
Run-out distance	98.4 m	99.0 m

Table 8.1: Comparison between measured and calculated values at the USGS Flume.

part of the flume (green in the geometry-schematic Figure 8.1) solid wall conditions are assumed. Hence, the normal component of the velocity is reflected. We did not incorporate additional side wall friction. The bulk moves approximately as a plug in the channel width. Out-flow boundary conditions are applied in the deposition area (red part of the geometric boundary in Figure 8.1). Note that ghost cells at the *non-convex* boundaries close to the channel mouth need special treatment. One cell exhibits two boundaries of the flow domain, hence, when initializing values after each time step, two different values of the state variables must be saved.

8.1.2 Choice of the friction parameter

We assume basal friction to be given by a Coulomb relation, with friction coefficients μ_1 for the solid phase and μ_2 for the fluid phase. However, in a first example μ is chosen to be constant for both components ($\mu := \mu_1 = \mu_2$). The one parameter is chosen to be $\mu = 0.49$, such that the maximal run-out distance of the simulation agrees with the measured run-out distance of the experiment. We found it to be reasonably high in comparison to other dry friction values for debris flows, suggested in the literature [74, 63, 39]. However, in our simulation we neglected side wall friction and any contribution of a velocity dependent Chezy friction, such that a high calibration value for μ is the natural consequence. Coulomb friction in every component is a simple assumption that allows us to focus on the physical effects associated with momentum exchange.

Besides the maximal run-out distance, we have two height and velocity measurements, located in the channel (66 m) and in the deposition area (90 m). Choosing the friction coefficient to match the run-out distance also provided acceptable results for the measurements at 66m. The calculated velocities were in good agreement with the data, the peak flow depth showed reasonable agreement (compare Figure 8.2). Details on measurements versus simulation are summarized in Table 8.1. A possible reason for the systematic overestimation of the height will be given later.

Figure 8.2 shows two plots of the bulk height in the calibration run. Shown are contour plots of the points in time when the front of the flow passes the check points. At 66 m the

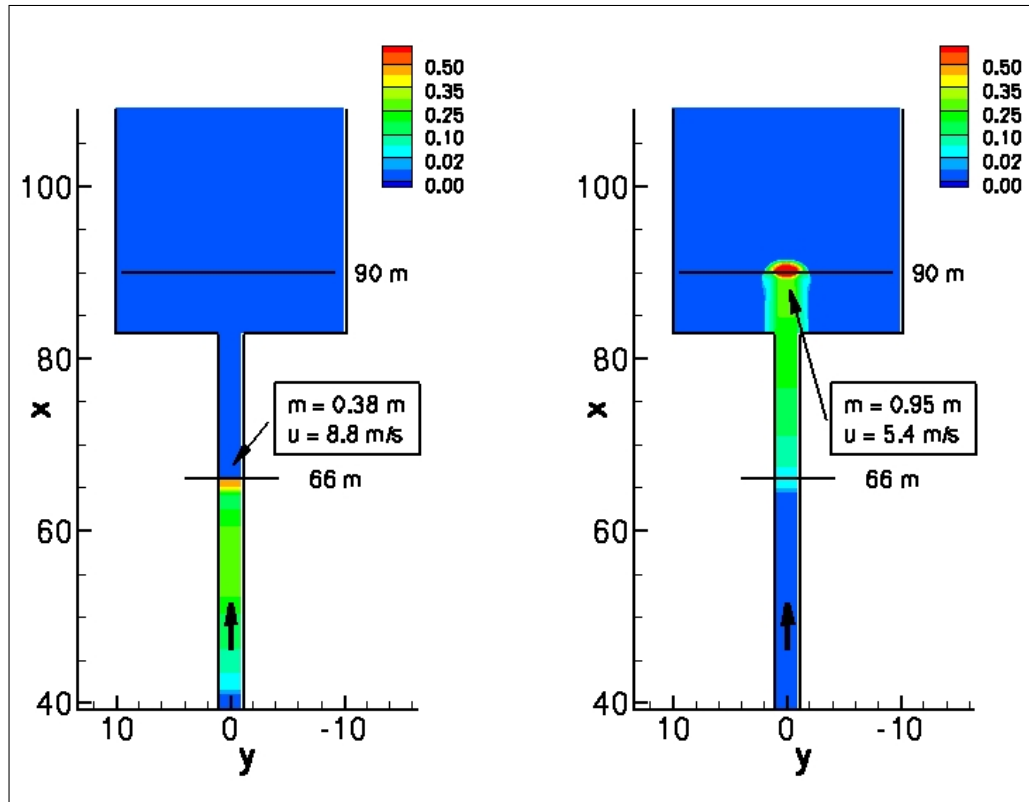


Figure 8.2: A contour plot of the calibration run. Left: The flow front is located at the first check location at 66m. Right: The flow front just passed the channel mouth and enters the deposition area - the peak flow height is at the second measuring location at 90 m.

flow is still channelized. Also at the second location, the bulk of the flow is still confined and does not show large lateral spreading. This agrees with realistic flow situations found in the flume.

8.1.3 Separation of components

In the next example, the friction coefficient of the second component differs slightly from the first component $\mu_1 \neq \mu_2$. The μ -values are chosen to be $\mu_1 = 0.52$ and $\mu_2 = 0.49$. Hence, the net acceleration, being gravitational acceleration minus basal friction is different in both components, and this will eventually give rise to separation of the species. However, the momentum exchange counteracts the phase separation and keeps the bulk together. In Figure 8.3, the bulk height is plotted just after the flow leaves the channel mouth and enters the deposition area. The left picture corresponds to a computation with a high momentum relaxation (associated with the small time scale $\tau = 0.001$), and shows a single height maximum. The picture on the right hand side is the result of a simulation with a small momentum exchange ($\tau = 3$), showing the bulk mass developed two local bulk height maxima. The slower moving maximum corresponds to the solid phase with the higher friction coefficient, the faster maximum to the fluid phase, with

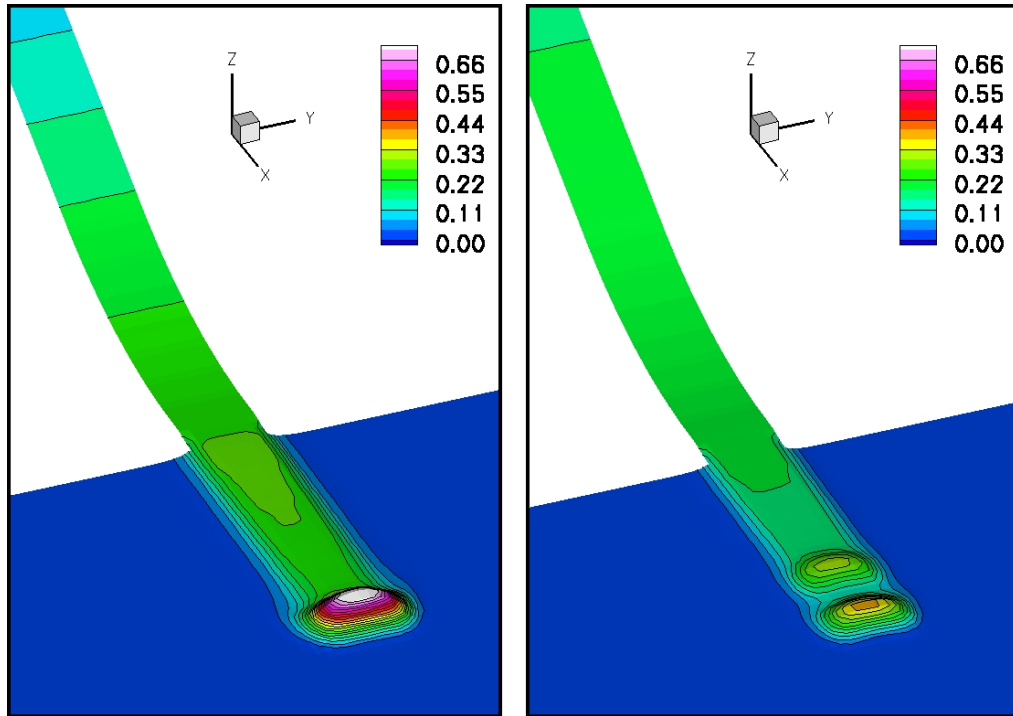


Figure 8.3: Separation of components on the chute

the smaller friction coefficient. In a realistic solid-fluid two-component flow, separation of components will take place, when the particles settle in the deposition area, and their basal and inner friction increases (dewatering). Moreover, a realistic debris flow front exhibits a precursory fluid surge (compare Figure 1.3). The latter could be an explanation for the systematic overestimation of bulk masses and heights by the model. Models that do not allow for phase separation assume that the complete mixture is present in the flow front. However in a realistic flow situation, the initial volume might have been reduced due to Pre-flow of the fluid component.

8.2 Simulation in realistic terrain

This final section is devoted to the simulation of debris flows in natural terrain. Besides the implementation of a robust numerical scheme, input data pre-processing and post-processing of the numerical results is an additional difficulty. Figure 8.4 summarizes the main steps of this process. At first topographical data from a digital elevation model (DEM) is converted into a surface mesh. Additional information, such as the value of friction parameters, is either set directly, or extracted from the DEM corresponding to a georeferenced map containing vegetation and surface roughness information. For large computational domains or inhomogeneous regions, automated routines are used to determine the necessary flow parameters. Finally, initial conditions are set. They depend on measurements on the amount of available material and hydrographs, but also on subjective assessment by experts with field experience.

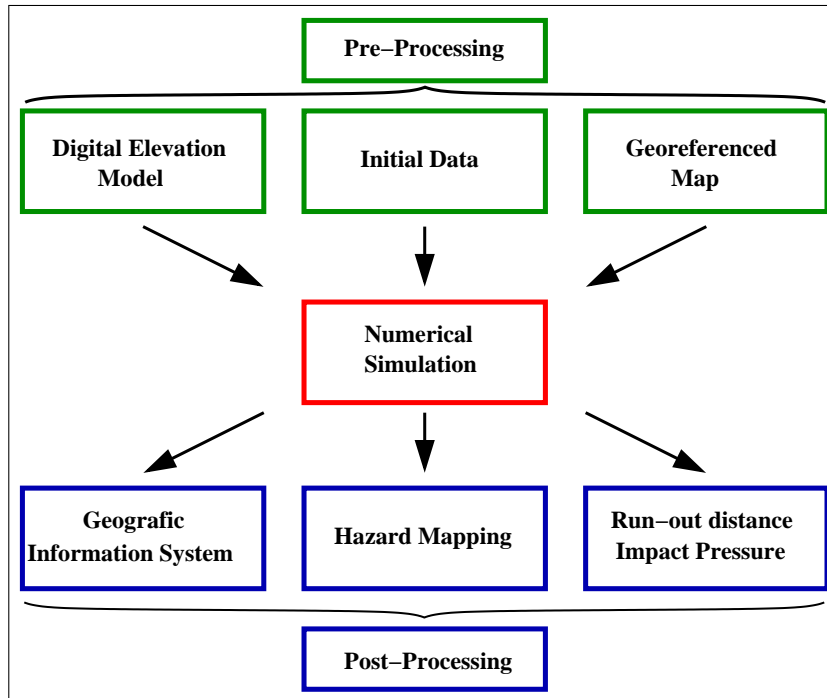


Figure 8.4: Flow chart of the different steps, involved in a numerical simulation of geophysical mass flows in real terrain

In a next step the actual numerical solver computes the solution. The results are interpreted by once again making use of Geographic Information Systems (GIS). A common criteria to evaluate the performance of the simulation is a comparison between simulated run-out distance and the run-out distance of the actual flow event [19]. Once calibrated, the numerical software can serve as a tool in the process of creating hazard maps [34]. Hazard maps relate risk from geophysical mass movements to event return period and are essential for land-use planning [60]. However, any simulation of this kind still contains a large amount of uncertainty and knowledge of experts is still required to define and interpret the simulated results.

8.2.1 RAMMS - Rapid Mass Movements

The development of the software package RAMMS (Rapid Mass Movements) started at the Swiss Federal Institute for Snow and Avalanche Research [20, 19]. RAMMS integrates the previously discussed demands of the practitioners into one software tool. It combines three-dimensional process modules for snow avalanches, debris flows and rockfalls with protection and visualization modules. Because the system is linked to a GIS environment, RAMMS is a powerful tool for hazard mitigation studies in mountainous regions, that are affected by gravity driven, rapid mass movements [16].

To prepare a simulation for any location in the Swiss Alps, the region of interest is extracted from an underlying database, which contains a DEM of Switzerland and a cor-

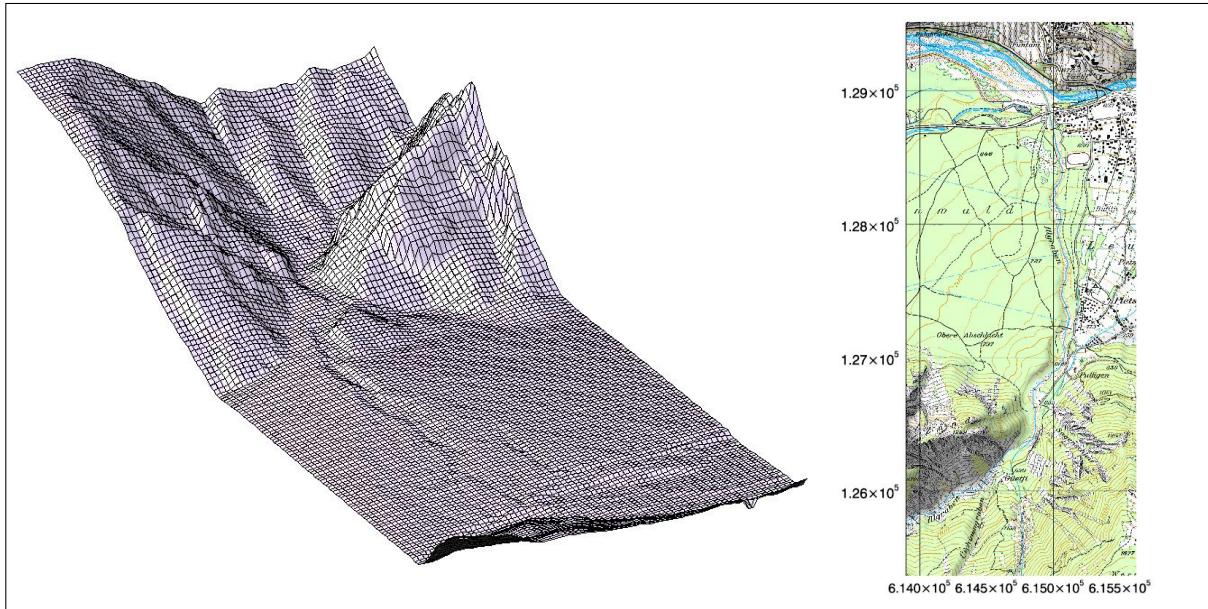


Figure 8.5: Left panel: Digital elevation model (DEM) of the Illgraben area - DTM-AV ©2008 swisstopo (DV033492); Right panel: Corresponding georeferenced map PK25 ©2008 swisstopo (DV033492)

responding georeferenced map [83]. The topographical data of the Illgraben torrent is shown on the left side and the georeferenced map on the right side of Figure 8.5. The package uses direct cartesian projections of the common global coordinate system given by latitude, longitude and height. Hence, simulations are not restricted to the European Alps, but can also be performed for other mountain ranges, such as the Himalayans and the Andes [16].

The open source geographic information system GRASS provides routines to do the necessary analysis of the given terrain. The resulting data is visualized within RAMMS, however it is also possible to export it into standard GIS-formats for the use in other GIS-software products. RAMMS does not serve as a software "black-box" for the simulation of a geophysical mass flow. It rather provides an integrated platform for hazard assessment and mitigation studies.

RAMMS incorporates both a first and a second order Finite Volume solver based on a HLL approximate Riemann solver. In the second order version, a linear reconstruction of the cell values with Minmod slope limitation, and a Heun time integration is applied. The mesh width of the computational domain can be chosen arbitrarily, but it should be geared to the grid resolution of the underlying DEM.

At the moment, the model is formulated as a one-phase system with a Voellmy-Salm basal friction formulation [6]. It is successfully applied to dense flow avalanche problems and covers also basic aspects of debris flows. A generalization to the two-component system

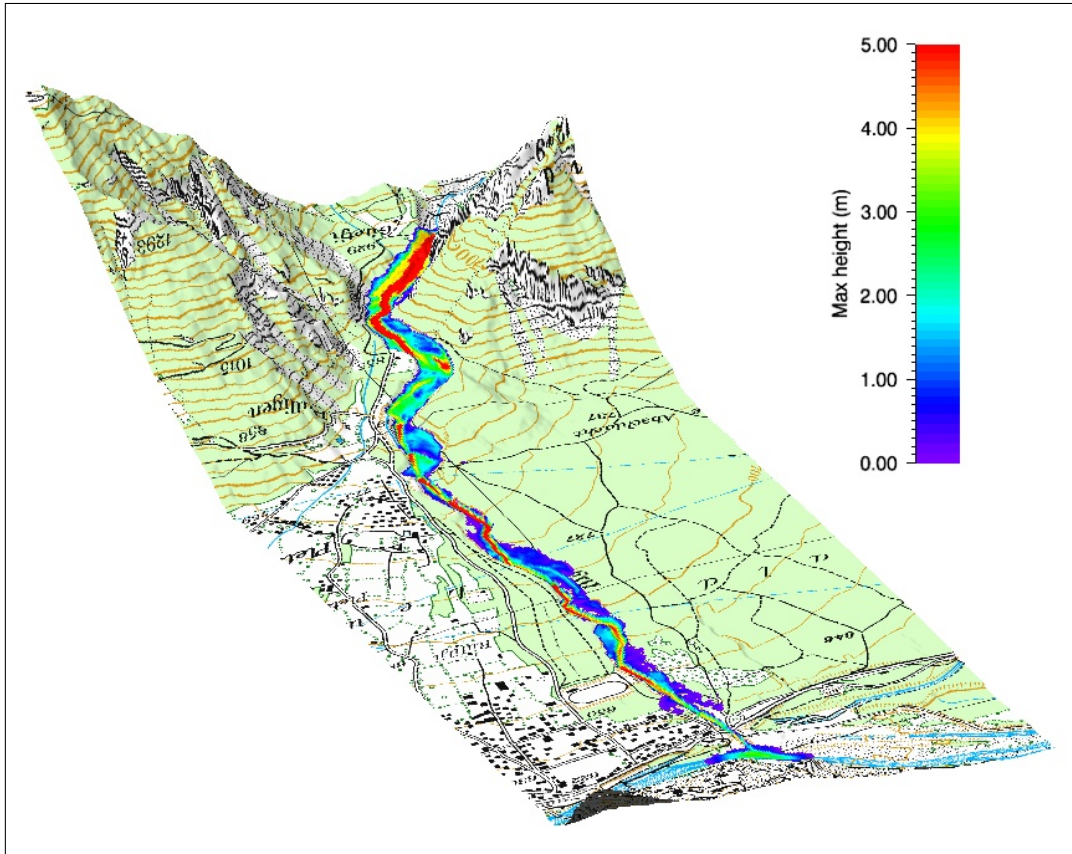


Figure 8.6: Maximal height of an Illgraben simulation, corresponding to the event on 28th May, 2005; 3d view; Illgraben overview.

is planned as future work.

8.2.2 A debris flow at Illgraben

Figure 8.6 depicts the maximal flow heights of a first order simulation of a debris flow event at Illgraben, that took place on the 28th May 2005. From measurements at the Illgraben observation site, the bulk volume has been estimated to be around $140'000 \text{ m}^3$ (2.1.1). For other details on this event, we refer to Table 2.1. The underlying digital elevation model has a grid resolution of 2.5 m, and the mesh width of the computational domain is set to 5 m. The friction coefficients are set to $\mu = 0.1$ and $\xi = 0.003 \frac{\text{s}^2}{\text{m}}$. All calculations are done with a CFL-number of 0.9.

In Figure 8.7 the same simulation results are plotted, this time zoomed into the area, where the measuring facilities are installed (beneath the bridge). With a maximal height of $H \approx 2.1 \text{ m}$, the simulation results are in good agreement to the measurements. The computed velocity results ($U \approx 3\text{-}4 \frac{\text{m}}{\text{s}}$) are slightly slower than the average front velocity determined by correlating the geophone signals. In the height plot 8.7 the position of two check dams in the channel can be seen. The first is located underneath the bridge, the

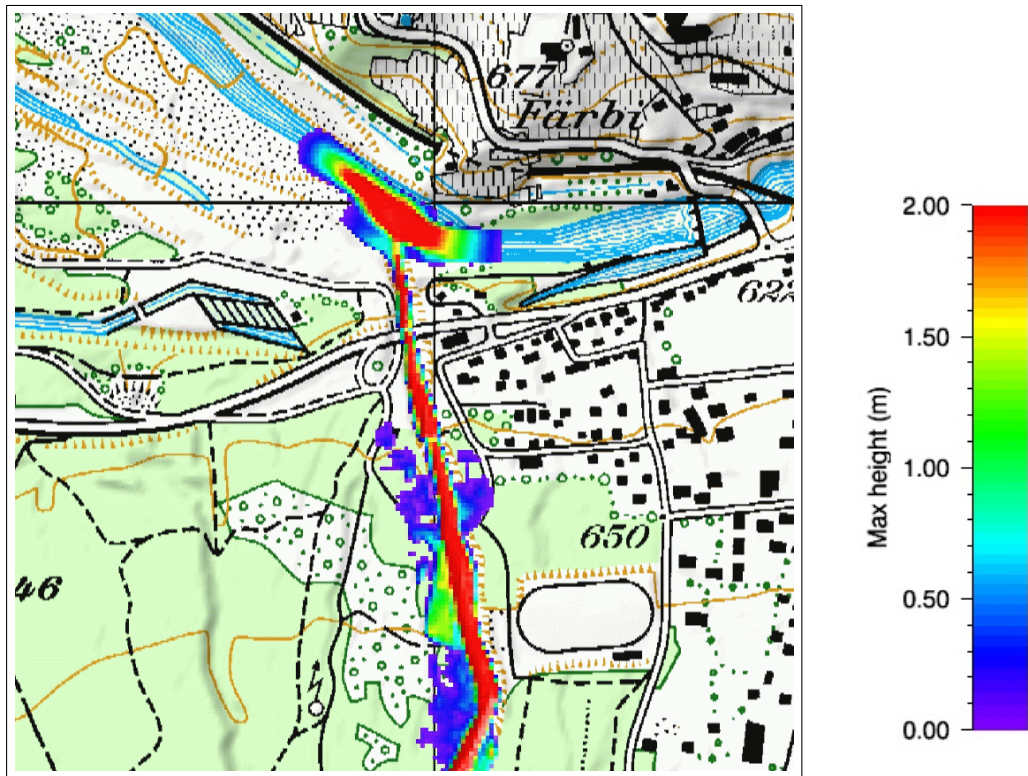


Figure 8.7: Maximal height of an Illgraben simulation, corresponding to the event on 28th May, 2005; 2d view; Zoom into the region where the measuring devices are installed.

second some 470m upstream. These stabilizing dams cause vertical drops of 2-3 m and hence, locally, the flow accelerates and the corresponding height decreases.

The right choice of the friction coefficients is not yet clear for the wide spectrum of debris flow events observed at the Illgraben test site. Effort has to be made to calibrate them in future. Nevertheless, we can still profit from the modeling results. The amount of available material in the catchment area of the Illgraben is reasonably high [], such that a potential initial volume could be up to $500'000 \text{ m}^3$. Performing a calculation with such an initial volume provides a hint of possibly endangered areas. The maximum heights of this extreme simulation can be seen in Figure 8.8. Note, that by applying the calibrated μ and ξ of the previous simulation, we implicitly assume, that the friction coefficients have no strong dependence on the flow volume.

8.2.3 Outlook

Although the achieved results are promising, there are still many open questions in the numerical simulation of geophysical mass flows in natural terrain. With respect to the development and implementation of a software package such as RAMMS, the following two topics require intense research in the near future:

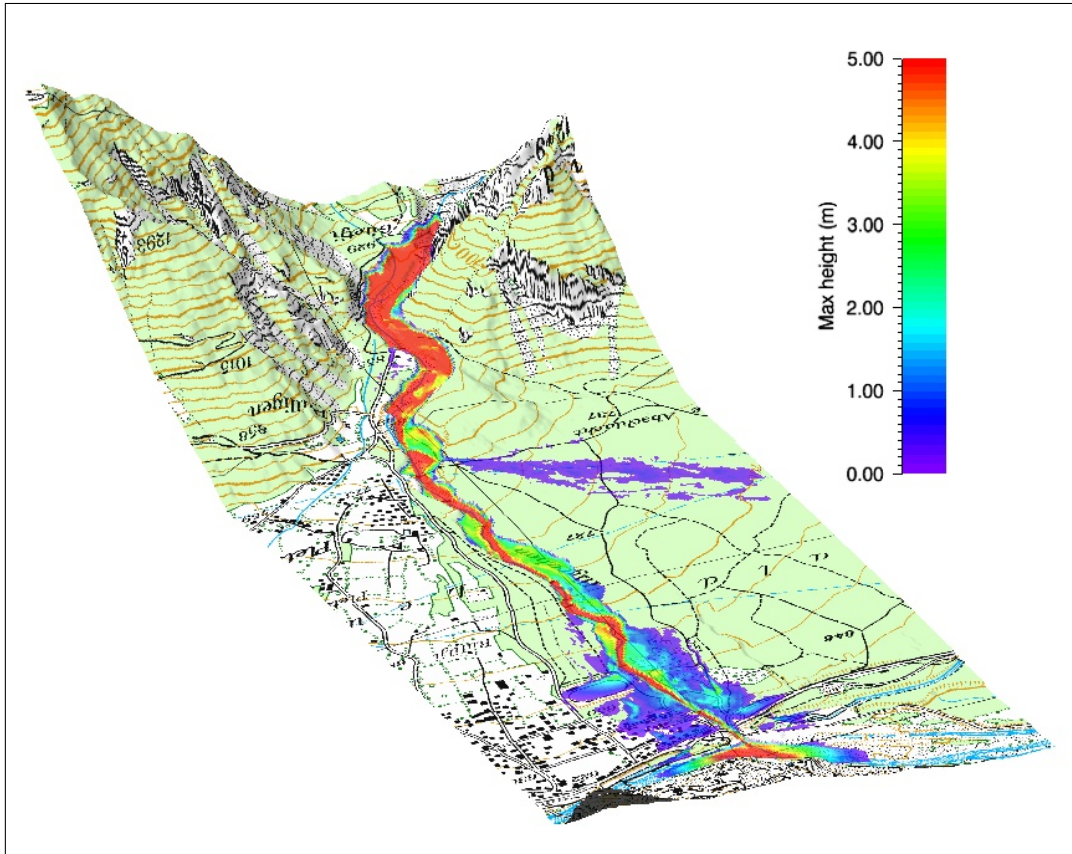


Figure 8.8: Illgraben simulation with a big initial volume of 500000 m^3

- Strong variations in the topography cause local instabilities in the velocities. In some cases these do not influence the global result significantly, as they are damped quickly and remain local. In others cases they lead to a global breakdown of the calculation. Sample topographies involving sudden drops in the topography and channelized geometries will be used to systematically investigate this problem.
- The debris flow module of the software tool will be extended to the debris flow mixture model. Then a detailed comparison between one-phase models and innovative two-phase models can be preformed using well documented test cases.

Bibliography

- [1] R. Abgrall and S. Karni. *Hyperbolic Problems: Theory, Numerics, Applications*, chapter Two-layer shallow water systems: a relaxation approach, pages 135–144. Springer-Verlag, Berlin-Heidelberg-New York, 2008.
- [2] C. Ancey and P. Evesque. Frictional-collisional regime for granular suspension flows down an inclined channel. *Physical Review E*, 62(6):8349–8360, 2000.
- [3] L. Armi. *The internal hydraulics of two flowing layers of different densities*. PhD thesis, University of Berkley, 1975.
- [4] L. Armi. The hydraulics of two flowing layers with different densities. *Journal of Fluid Mechanics*, 163:27–58, 1986.
- [5] R.J. Atkins and R.E. Craine. Continuum theory of mixtures: Basic theory and historical development. *Q.J. Mech. Appl. Math., Part 2*, 29:209–244, 1976.
- [6] P. Bartelt, B. Salm, and U. Gruber. Calculating dense-snow avalanche runout using a voellmy-fluid model with active/passive longitudinal straining. *Journal of Glaciology*, 45(150):242–254, 1999.
- [7] G.K. Batchelor. *An Introduction to Fluid Dynamics*. Cambridge Mathematical Libraries. Cambridge University Press, 2000.
- [8] S. Berres. *Modeling, analysis and numerical simulation of polydisperse suspensions*. PhD thesis, Fachbereich Mathematik der Universität Stuttgart, 2006.
- [9] S. Berres, R. Bürger, and E.M. Tory. On mathematical models and numerical simulation of the fluidization of polydisperse suspensions. *Applied Mathematical Modelling*, 29:159–193, 2005.
- [10] S. Berres, R. Bürger, and W.L. Wendland. Mathematical models for the sedimentation of suspensions. Internal report, Universität Stuttgart.
- [11] A.W. Bishop and A.E. Skinner. The influence of high pore-water pressure on the strength of cohesionless soils. *Philosophical Transactions of the Royal society of London, Series A, Mathematical and Physical Sciences*, 284(1318), 1977.

- [12] F. Bouchut and T. Morales. An entropy satisfying scheme for two-layer shallow water equations with uncoupled treatment. Technical report, Departement de Mathematiques et Applications Ecole Normale Superieure & CNRS, 2007.
- [13] F. Bouchut and M. Westdickenberg. Gravity driven shallow water models for arbitrary topography. *Comm. Math. Sci.*, 2(3):359 ff., 2004.
- [14] A.N. Bozhinskiy and A.N. Nazarov. Two-phase model of debris-flow. In Ko-Fei Liu, editor, *Debris-Flow Hazards Mitigation: Mechanics, Prediction and Assessment*, pages 263–269, 2000.
- [15] E. Buckingham. On physically similar systems; illustrations of the use of dimensional equations. *Physical Review*, 4(4):345–376, Oct 1914.
- [16] A. Casteller, M. Christen, R. Villalba, H. Martinez, V. Stöckli, J.C. Leiva, and P. Bartelt. Validating numerical simulations of snow avalanches using dendrochronology: the cerro ventana event in northern patagonia, argentina (accepted). *Nat. Hazards Earth Syst. Sci.*, 8:1–11, 2008.
- [17] M.J. Castro, J.A. Garcia-Rodriguez, J.M. Gonzales-Vida, J. Macias, C. Pares, and M.E. Vazquez-Cendon. Numerical simulation of two-layer shallow water flows through channels with irregular geometry. *Journal of Computational Physics*, 195:202–235, 2004.
- [18] C. Chen, editor. *Debris-flow Hazards Mitigation: Mechanics, Prediction, Assessment - Proceedings of the First International Conference held in San Francisco, California, August 7-9, 1997*. American Society of Civil Engineers, 1997.
- [19] M. Christen, P. Bartelt, and U. Gruber. Numerical calculation of snow avalanche runout distances. In *Proc. of the 2005 International Conference, July 12-15, 2005. Cancun, Mexico*, page 11 p., 2005.
- [20] M. Christen, P. Bartelt, and U. Gruber. Ramms - a modeling system for snow avalanches, debris flows and rockfalls based on idl. *Photogrammetrie - Fernerkundung - Geoinformation*, 4:289–292, 2007.
- [21] J.E. Costa. *Developements and applications of geomorphology*, chapter Physical geomorphology of debris flows, pages 268–317. Springer-Verlag, Berlin-Heidelberg-New York, 1984.
- [22] P. Coussot. *Mudflow Rheology and Dynamcis. IAHR Monograph*. Balkema Pub., Rotterdam, Netherlands, 1997.
- [23] P. Coussot and C. Ancey. Rheophysical classification of concentrated suspensions and granular pastes. *Physical Review E*, 59:4445–4457, 1999.
- [24] D.M. Cruden. A simple definition of a landslide. *Bulletin of the International Association of Engineering Geology*, 43:27–29, 1991.

- [25] D.M. Cruden and D.J. Varnes. Landslide types and processes. *Landslides: Investigation and Mitigation, Special Report*, 247:36–75, 1996.
- [26] T.R. Davies. Dynamically similar small-scale debris flow models. In *International Workshop on floods and inundations related to large earth movements*. Fluvial Hydraulic Section, 1994.
- [27] R.P. Denlinger and R.M. Iverson. Flow of variably fluidized granular masses across three-dimensional terrain 2. numerical predictions and experimental tests. *Journal of Geophysical Research*, 106(B1):553–566, 2001.
- [28] P.G. Drazin. *Introduction to Hydrodynamic Stability*. Cambridge University Press, 2002.
- [29] D.A. Drew and S.L. Passman. *Theory of Multicomponent Fluids*. Springer-Verlag, Berlin-Heidelberg-New York, 1998.
- [30] B. Einfeldt. On godunov-type methods for gas dynamics. *Journal of Computational Physics*, 25:294–318, 1988.
- [31] A.C. Fowler. *Mathematical Models in the Applied Sciences*. Cambridge University Press, 1997.
- [32] J. M. N. T. Gray. Rapid granular avalanches. *Dynamic Response of granular and porous material under large and catastrophic deformations, Lecture Notes in Applied and Computational Mechanics*, 11:3–42, 2002.
- [33] J.M.N.T. Gray, M. Wieland, and K. Hutter. Gravity-driven free surface flow of granular avalanches over complex basal topography. *Proceedings: Mathematical, Physical and Engineering Sciences*, 455(1985):1841–1874, 1999.
- [34] U. Gruber and P. Bartelt. Snow avalanche hazard modelling of large areas using shallow water numerical methods and gis. *Environmental Modelling & Software*, 22:1472–1481, 2007.
- [35] A. Harten. On a class of high resolutional total variation stable finite difference schemes. *SIAM, Journal of Num. Anal.*, 21:1–23, 1984.
- [36] A. Harten, P.D. Lax, and B. van Leer. On upstream differencing and godunov-type schemes for hyperbolic conservation laws. *SIAM, Rev.*, 25:35–61, 1983.
- [37] R.D. Holtz and W.D. Kovacs. *An Introduction to Geotechnical Engineering*. Prentice-Hall, Inc., 1981.
- [38] O. Hungr, S.G. Evans, M.J. Bovis, and J.N. Hutchinson. A review of the classification of landslides of the flow type. *Environmental & Engineering Geoscience*, 7(3):221–238, 2001.
- [39] M. Hürlimann, D. Rickenmann, and C. Graf. Field and monitoring data of debris-flow events in the swiss alps. *Can. Geotech. Journal*, 40:161–175, 2003.

- [40] K. Hutter. Report on debris flow modeling. Report, Federal Institute fo Snow and Avalanche Research, 1995.
- [41] K. Hutter. *Fluid- und Thermodynamik*. Springer-Verlag, Berlin-Heidelberg-New York, 2003.
- [42] K. Hutter, Y. Wang, and S.P. Pudasaini. The savage-hutter avalanche model. how far can it be pushed? *Philosophical Transactions A: Mathematical, Physical and Engineering Sciences, the Royal Society*, 363(1832):1507–1528, 2005.
- [43] M. Ishii and T. Hibiki. *Thermo-fluid Dynamics of Two-phase Flow*. Springer-Verlag, Berlin-Heidelberg-New York, 2006.
- [44] R.M. Iverson. The physics of debris flows. *Reviews of Geophysics*, 35(3):245–296, 1997.
- [45] R.M. Iverson, J.E. Costa, and R.G. LaHusen. Debris-flow flume at h.j. andrews experimental forest, oregon. USGS Open-File Report 92-483, U.S. Geological Survey, 1992.
- [46] R.M. Iverson and R.P. Denlinger. The physics of debris flows - a conceptual assessment. *Proc. Symp. on Erosion and Sedimentation in the Pacific Rim, Corvallis*, 165, 1987.
- [47] R.M. Iverson and R.P. Denlinger. Flow of variably fluidized granular masses across three-dimensional terrain 1. coulomb mixture theory. *Journal of Geophysical Research*, 106(B1):537–552, 2001.
- [48] R.M. Iverson and R.P. Denlinger. Mechanics of debris flows and debris-laden flash floods. In *Seventh Federal Interagency Sedimentation Conference*, pages IV–1–IV–8, 2001.
- [49] R.M. Iverson and J.J. Major. Debris-flow deposition: Effects of pore-fluid pressure and friction concentrated at flow margins. *Geological Society Of America Bulletin*, 111(10):1424–1434, 1999.
- [50] R.M. Iverson and J.W. Vallance. New views of granular mass flows. *Geology*, 29(2):115–118, 2001.
- [51] M. Jakob. A size classification for debris flows. *Engineering Geology*, 79:151–161, 2005.
- [52] C.D. Jan and H.W. Shen. A review of debris flow analysis. *Proc. XXV IAHR Congress, Technical Session B*, 3, 1993.
- [53] D.D. Joseph and T.S. Lundgren. Ensemble averaged and mixture theory equations for incompressible fluid-particle suspensions. *International Journal of Multiphase Flow*, 16(1):35–42, 1990.

- [54] M.A. Kern, F. Tiefenbacher, and J.N. McElwaine. The rheology of snow in large chute flows. *Cold Regions Science and Technology*, 39:181–192, 2004.
- [55] K.R.Rajagopal and L. Tao. *Mechanics of Mixtures*. World Scientific Publishing Co Pte Ltd - New Jersey - London - Hong Kong, 1995.
- [56] G. J. Kynch. A theory of sedimentation. *Trans. Faraday Soc.*, 48, 1952.
- [57] B. Van Leer. Towards the ultimate conservative difference scheme ii. monotonicity and conservation combined in a second order scheme. *J. Comp. Phys.*, 14:361–370, 1974.
- [58] R.J. LeVeque. *Finite Volume Methods for Hyperbolic Problems*. Cambridge Texts in Applied Mathematics. Cambridge University Press, 2002.
- [59] M. Logan and R.M. Iverson. Video documentation of experiments at the usgs debris-flow flume 1992-2006. USGS Open-File Report 2007-1315, U.S. Geological Survey, 2007.
- [60] S. Margreth and U. Gruber. Use of avalanche models for hazard mapping. Technical report, Swiss Federal Institute for Snow and Avalanche Research, 1996.
- [61] G.P. Matson and A.J. Hogg. Two-dimensional dam break flows of herschel-bulkley fluids: The approach to the arrested state. *Journal of Non-Newtonian Fluid Mechanics*, 142:79–94, 2006.
- [62] B. McArdell, P. Bartelt, and J. Kowalski. Field observations of basal forces and fluid pore pressure in a debris flow. *Geophysical Research letters*, 34(L07406), 2007.
- [63] B. W. McArdell, B. Zanuttigh, A. Lamberti, and D. Rickenmann. Systematic comparison of debris flows at the illgraben torrent, switzerland. In *Debris-Flow Hazards Mitigation: Mechanics, Prediction and Assessment*, pages 647–657. 2003 Millpress, Rotterdam, 2003.
- [64] M.Jakob and O.Hungr. *Debris-flow Hazards and Related Phenomena*. Springer-Verlag, Berlin-Heidelberg-New York, 2005.
- [65] R.M. Nedderman. *Statics and Kinematics of Granular Material*. Cambridge University Press, 1992.
- [66] A.K. Patra, C.C. Nichita, A.C. Bauer, E.B. Pitman, M. Bursik, and M. Sheridan. Parallel adaptive discontinuous galerkin approximation for thin layer avalanche modeling. *Computers & Geosciences*, 32:912–926, 2006.
- [67] M. Pelanti, F. Bouchut, A. Mangeney, and J. Vilotte. Numerical modeling of two-phase gravitational granular flows with bottom topography. *Report about Post-doc project*, 2007.
- [68] E.B. Pitman and L. Le. A two-fluid model for avalanche and debris flow. *Philosophical Transactions of the Royal society*, 363:1573–1601, 2005.

- [69] E.B. Pitman, C.C. Nichita, A. Patra, A.C. Bauer, M. Sheridan, and M. Bursik. Computing granular avalanches and landslides. *Physics of fluids*, 15(12):3638–3646, 2003.
- [70] S.P. Pudasaini and K. Hutter. *Avalanche Dynamics - Dynamics of rapid flows of dense granular avalanches*. Springer-Verlag, Berlin-Heidelberg-New York, 2007.
- [71] J.F. Raffle. Pressure variation within concentrated suspensions. *Journal of Physics D: Applied Physics*, 9:1239–1252, 1976.
- [72] D. Rickenmann and C. Chen, editors. *Proceedings of the third international conference on Debris-Flow Hazards Mitigation: Mechanics, Prediction, and Assessment*, volume 1. Millpress, Rotterdam, 2003.
- [73] D. Rickenmann and C. Chen, editors. *Proceedings of the third international conference on Debris-Flow Hazards Mitigation: Mechanics, Prediction, and Assessment*, Volume 1, volume 2. Millpress, Rotterdam, 2003.
- [74] D. Rickenmann, D. Laigle, B.W. McArdeell, and J. Hübl. Comparison of 2d debris-flow simulation models with field events. *Computational Geoscience*, 10:241–264, 2006.
- [75] P.L. Roe. Characteristic-based schemes for the euler equations. *Ann. Rev. Fluid Mech.*, 18:337, 1986.
- [76] G. Sartoris and P. Bartelt. Upwinded finite difference schemes for dense snow avalanche modeling. *Int. Journal for Num. Meth. in Fluids*, 32:799–821, 2000.
- [77] S.B. Savage and K. Hutter. The motion of a finite mass of a granular material down a rough incline. *Journal of Fluid Mechanics*, 199:177–215, 1989.
- [78] S.B. Savage and K. Hutter. The dynamics of avalanches of granular materials from initiation to runout. part 1: Analysis. *Acta Mechanica*, 86:201–223, 1991.
- [79] J. H. Song. A remedy for the ill-posedness of the one-dimensional two-fluid model. *Nuclear Engineering and Design*, 222:40–53, 2003.
- [80] J. H. Song and M. Ishii. The well-posedness of incompressible one-dimensional two-fluid model. *International Journal of Heat and Mass Transfer*, 43:2221–2231, 2000.
- [81] J. H. Song and M. Ishii. The one-dimensional two-fluid model with momentum flux parameters. *Nuclear Engineering and Design*, 205:145–158, 2001.
- [82] J. Stiny. *Die Muren*. Verlag der Wagnerschen Universitätsbuchhandlung, Innsbruck, 1910.
- [83] Swisstopo. <http://www.swisstopo.ch>. Product information, Swiss Federal Office of Topography, 2001.
- [84] T. Takahashi. Debris flow. *Ann. Rev. of Fluid Mechanics*, 13:57–77, 1981.

- [85] T. Takahashi. *Debris Flow. IAHR Monograph Series*. Balkema Publishers, The Netherlands, 1991.
- [86] K. Terzaghi. The shearing resistance of saturated soils and the angles between planes of shear,. *Proc. Int. Conf. Soil Mech.*, 1st:54–56, 1936.
- [87] E. F. Toro. Riemann problems and the waf method for solving the two-dimensional shallow water equations. *Philos. Trans. R. Soc. London, Ser. A*, 338:43–68, 1992.
- [88] E. F. Toro. *Riemann solvers and numerical methods for fluid dynamics: a practical introduction*. pub-SV, pub-SV:adr, 1997.
- [89] E.F. Toro. *Shock-Capturing Methods for Free-surface Shallow Flows*. John Wiley and Sons, Ltd, Manchester, UK, 2001.
- [90] M. Torrilhon. Two-dimensional bulk micro-flow simulations based on regularized grad’s 13-moment-equations. *SIAM Multiscale Model. Sim.*, 5(3):695–728, 2006.
- [91] D.J. Varnes. Slope movement types and processes. *Landslide Analysis and Control, Special Report*, 176:11–33, 1978.
- [92] G.F. Wieczorek and N.D. Naeser, editors. *Debris-flow Hazards Mitigation: Mechanics, Prediction, and Assessment*. Balkema, Rotterdam, 2000.
- [93] M. Wieland, J.M.N.T. Gray, and K. Hutter. Channelized free-surface flow of cohesionless granular avalanches in a chute with shallow lateral curvature. *Journal of Fluid Mechanics*, 392:73–100, 1999.

Curriculum Vitae

Julia Kowalski,

born 22. April 1979 in Bergisch-Gladbach, Germany

1985	Elementary School in Bergisch-Gladbach
1986-1989	Elementary School in Hamm
1989-1998	Gymnasium Schwabmünchen
1998	Abitur
1998-2004	University of Augsburg, subjects: Mathematics, Physical Education, and Computer Science
2001	Master of Education
2001-2004	Teaching Assistant Dept. Mathematics at University of Augsburg
2003	Internship at the Swiss Federal Institute for Snow and Avalanche Research, Davos, Switzerland
2004	Diploma in Mathematics of University of Augsburg Thesis: <i>Dynamics of Granular Material Avalanches and Numerical Approximations of Savage-Hutter Models</i>
2005	PhD Student at University of Texas at Houston (discontinued)
since 2005	PhD Student at the Swiss Federal Institute for Snow and Avalanche Research, Davos, Switzerland

